UNIVERSIDADE FEDERAL DE ALFENAS

LUIS RICARDO PEREIRA MUCCIARONI

OPTICAL SETUP FOR LASER MICROFABRICATION: DEVELOPMENT OF PHOTONIC DEVICES

Poços de Caldas/MG
2020

LUIS RICARDO PEREIRA MUCCIARONI

OPTICAL SETUP FOR LASER MICROFABRICATION:
DEVELOPMENT OF PHOTONIC DEVICES

Thesis presented as part of the requirements to obtain a Master’s Degree in Physics at the Federal University of Alfenas.
Concentration Area: Condensed Matter Physics

Advisor: Prof. Dr. Marcelo Gonçalves Vivas

Poços de Caldas/MG
2020

Dados Internacionais de Catalogação-na-Publicação (CIP)
Sistema de Bibliotecas da Universidade Federal de Alfenas
Biblioteca campus Poços de Caldas

Mucciaroni, Luis Ricardo Pereira.
M942o Optical setup for laser microfabrication: development of photonic devices / Luis Ricardo Pereira Mucciaroni. – Poços de Caldas/MG, 2020.
108 f. –

Orientador(a): Marcelo Gonçalves Vivas.
Dissertação (Mestrado em Física) – Universidade Federal de Alfenas, campus Poços de Caldas, 2020.
Bibliografia.

1. Óptica não linear. 2. Microfabricação a laser. 3. Filmes finos – propriedades ópticas. 4. Pontos quânticos. 5. Sistemas de varredura. I. Vivas, Marcelo Gonçalves. II. Título.
CDD – 530

Ficha Catalográfica elaborada por Thaís Aparecida de Lima
Bibliotecária-Documentalista CRB6/3032

LUIS RICARDO PEREIRA MUCCIARONI

OPTICAL SETUP FOR LASER MICROFABRICATION: DEVELOPMENT OF PHOTONIC DEVICES

The undersigned Examining Board approves this thesis submitted as part of the requirements for obtaining a Master's Degree in Physics from the Federal University of Alfenas..

Área de concentração: Fisica da Matéria Condensada

Aprovada em: 28 de agosto de 2020.

Prof. Dr. Marcelo Gonçalves Vivas
Instituição: Universidade Federal de Alfenas

Prof. Dr. Paulo Henrique Dias Ferreira
Instituição: Universidade Federal de São Carlos

Profa. Dra. Fábia Castro Cassanjes
Instituição: Universidade Federal de Alfenas

Documento assinado eletronicamente por **Marcelo Gonçalves Vivas**, **Professor do Magistério Superior**, em 02/09/2020, às 09:45, conforme horário oficial de Brasília, com fundamento no art. 6º, § 1º, do Decreto nº 8.539, de 8 de outubro de 2015

Documento assinado eletronicamente por **Fábia Castro Cassanjes**, **Professor do Magistério Superior**, em 02/09/2020, às 12:09, conforme horário oficial de Brasília, com fundamento no art. 6º, § 1º, do Decreto nº 8.539, de 8 de outubro de 2015.

Documento assinado eletronicamente por **Paulo Henrique Dias Ferreira**, **Usuário Externo**, em 04/09/2020, às 16:20, conforme horário oficial de Brasília, com fundamento no art. 6º, § 1º, do Decreto nº 8.539, de 8 de outubro de 2015.

ACKNOWLEDGMENTS

Firstly, I am glad to have my parents, my wife and daughter by my side pushing me all the time and encouraging myself to achieve such goals even among difficulties and pebbles in the way. In their absence, I am not sure if I would get the strength to be where I am today.

Next, I thank to the Lord because every single thing He has provided to my life. In special, my beautiful and beloved daughter early-born. She is the inspiration and the reason I get up every morning trying to be a better father, better husband and a better person.

To my advisor, Dr. Marcelo Gonçalves Vivas, who pushed me and taught me how to work properly in a lab of physics. Besides, he gave me all the instructions and conclusions to achieve such work at the end.

To my post-graduate professors, Fernando Gardim and Rodrigo Rocha Cuzzinato. Taking major subjects under their guidance certainly have increased and enhanced my skills as a physics teacher whereas a physics early-researcher.

To my classmates Carlos, Silas, Lidiana, Andrea, Michelle, Bruna and Arildo. The hard days became easier with you. I will never forget all the coffees we had at the breaks and intervals.

Finally, I thank the team of educational technicians from the University – Hérick, Fábio, Alexandre, Rosana, Kênia and Fernanda – besides friendship, they also supported me on many issues to sort out difficulties in the research or documental situations to do not miss any important process or deadline.

This study was financed in part by the Coordenação de Aperfeiçoamento de Pessoal de Nível Superior – Brasil (CAPES) – Finance Code 001.

ABSTRACT

Laser micromachining is a very useful technique that has been widely employed in a vast range of applications based on linear and nonlinear optics phenomena. In this context, the goal of this dissertation is to develop an optical micromachining system to make photonic devices on a reduced scale. For that, a Q-switch Nd:YAG pulsed laser with a temporal duration of 1.2 ns (nanosecond) operating at a low repetition rate (ranging from 10 to 2000 Hz) tuned at 532 nm (second-harmonic generation) was employed in this system. These features were assembled with a microscope mounted on a 3-D motor-driven stage, in which its movement is controlled by a homemade software that controls the stepper-motors over the XY-axis. Also, the z-axis of controls the focus over the sample where the experiment will occur. Initially, gold and chitosan thin films were used to characterize the optical setup, which mistakes, dismisses, mismatches, and misalignments were mapped and solved. After some improvement in the optical setup along with the automation/controlling software, we performed a systematic study of micromachining of polymer films doped with azo-chromophores and perovskite quantum dots thin films. To better understand the laser setup, we have investigated the influence of laser energy, the translation speed, and the numerical aperture of microscope objective on the average width of the microstructure, which indeed, provided important data to support the good usage of such optical setup. Our results have shown that our micromachining setup is able to microstructure materials in two different regimes, that is, ablation and surface modification, for both polymer films containing azo-compounds and quantum dot films compound. These two regimes of micromachining were possible by controlling the incident energy from the laser path, the speed in which the specimen moves, and also by changing the microscope objectives. The objectives, however, have a lot of influence on the outcomes because its numerical aperture causes the light to be gathered wider or narrower. Such changes allow the same laser energy to cause different structures on the surfaces only by altering the objectives. To sum up these three features, we have achieved linewidths as narrow as 0.8 µm. Moreover, it is possible to microfabricate any shape of microstructure in our experimental setup due to the dedicated program development for this present work.

Keywords: Nonlinear optics. Laser micromachining. Polymer thin films. Quantum dots.

RESUMO

A microfabricação a laser é uma técnica muito útil que tem sido amplamente empregada em uma vasta gama de aplicações baseadas em fenômenos ópticos lineares e não lineares. Neste contexto, o objetivo desta dissertação é desenvolver um sistema de micromaquinação óptica para fazer dispositivos fotônicos em uma escala reduzida. Para isso, foi empregado neste sistema um laser pulsado Q-switch Nd:YAG com duração temporal de 1,2 ns (nanossegundo) operando a uma baixa taxa de repetição (variando de 10 a 2000 Hz) sintonizado a 532 nm (segunda geração harmônica). Estas características foram montadas com um microscópio montado em um estágio motorizado 3-D, no qual seu movimento é controlado por um software caseiro que controla os motores passo-a-passo sobre o eixo XY. Além disso, o eixo z controla o foco sobre a amostra onde o experimento irá ocorrer. Inicialmente, filmes finos de ouro e quitosano foram usados para caracterizar a configuração ótica, que erros, demissões, desajustes e desalinhamentos foram mapeados e resolvidos. Após algumas melhorias na configuração ótica juntamente com o software de automação/controle, realizamos um estudo sistemático de micromaquinação de filmes de polímeros dopados com azo-chromophores e perovskite quantum dots thin films. Para entender melhor a configuração do laser, investigamos a influência da energia laser, a velocidade de translação e a abertura numérica da objetiva do microscópio na largura média da microestrutura, que de fato, forneceu dados importantes para suportar o bom uso de tal configuração óptica. Nossos resultados mostraram que nossa configuração de micromaquinação é capaz de microestruturar materiais em dois regimes diferentes, ou seja, ablação e modificação da superfície, tanto para filmes de polímeros contendo compostos de azo-componentes como para filmes de ponto quântico. Estes dois regimes de micromaquinação foram possíveis através do controle da energia incidente do percurso do laser, da velocidade em que a amostra se move, e também através da mudança das objetivas do microscópio. Os objetivos, entretanto, têm muita influência nos resultados porque sua abertura numérica faz com que a luz seja coletada mais larga ou mais estreita. Tais mudanças permitem que a mesma energia laser cause estruturas diferentes nas superfícies somente alterando as objetivas. Para resumir estas três características, atingimos larguras de linha tão estreitas quanto 0,8 µm. Além disso, é possível microfabricar qualquer forma de microestrutura em nossa configuração experimental devido ao desenvolvimento do programa dedicado a este trabalho atual.

Palavras-chave: Óptica não-linear. Microfabricação a laser. Filmes finos de plímero. *Quantum dots.*

LIST OF FIGURES

LIST OF GRAPHS

LIST OF TABLES

LIST OF ABREVIATIONS AND ACRONYMS

SHG – second harmonic generation

2PA – two photon absorption

mW – unidade de energia por tempo – 1 mW = 10^{-3}W

µJ – unidade de energia – 1 µJ = 10^{-6}J

nJ – unidade de energia – 1 µJ = 10^{-9}J

nm – unidade de dimensão espacial – 1 nm = 10^{-9}m

µm/s – unidade de velocidade – 1 µm/s = 10^{-6} m/s

QDs – Quantum Dots

PMMA – poly methyl methachrylate

LEOF – Laboratório de Espectroscopia Óptica & Fotônica

XRD – X-ray diffraction

CONTENTS

1 INTRODUCTION

Laser microfabrication is an optical technique that allows developing photonic devices with reduced dimensions such as waveguides, laser, ring resonators, polymer electro-optical modulator, efficient optical sensors, to cite a few [1]. Such a technique can be used in absorptive and transparent samples, and, at the same time, we can use it to remove materials (ablation) or only to cause localized changes in the material's properties like refractive index, for instance.

It is essential to mention that nonlinear optics provide the basis of many key technologies used today for delivering radiation sources in various wavelength ranges. Nonlinear optics also studies some phenomena that occur because of changes in the optical properties of a material system due to the presence of light. These phenomena are "nonlinear" in the meaning that they occur when a medium responds to an applied optical field in a nonlinear way related to the strength of such optical field.

Furthermore, laser microfabrication can occur in the linear and nonlinear optical regimes depending on the resolution that you want. To achieve higher resolution is necessary to induce nonlinear process in the material, which occurs when the photon flux is so high that it is possible to promote an electronic transition with the half photon energy required. Also, this nonlinear process is related to many applications for our daily life, such as shown in Figure 1.

Figure 1 - Mind map presenting an overview of nonlinear optics aplications in daily life

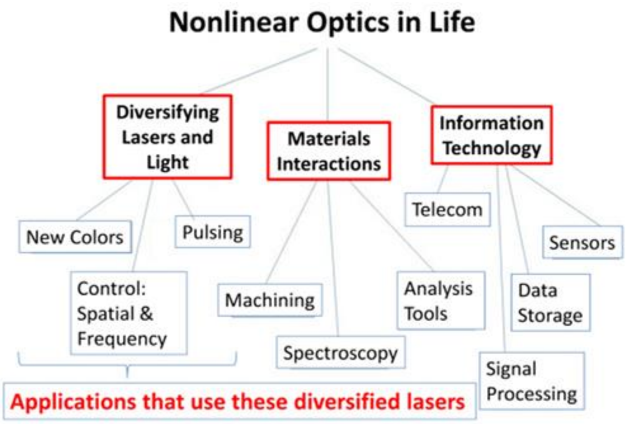

Source: [2].

Therefore, pulsed lasers from nanosecond ($10^{-9}s$) to femtosecond ($10^{-12}s$) with peak irradiance about $10^7 - 10^9 W/cm^2$ have been widely used for this purpose. Still, when the nonlinear effects are reached in the experiment, a larger scenario of the development of photonic devices is open.

Laser micromachining is a technique employed basically when an electronic or structural change is desired. This technique, however, can be applied using different time-scale pulse duration. Femtosecond lasers are used to cause electronic changes such as refractive index because the short pulse duration decreases the interaction with the sample. The nanosecond lasers, on the other hand, are often used to promote structural and deeper changes on the surface of the sample or even inside the bulk volume – this modification is called ablation.

Micromachining technique is the meaning for fabrication of 2D or 3D structures on the micrometer scale. Until few decades ago, watch parts and other small components were considered to be the micro-sized ones produced for the purpose of making watches and related tech. However, upcoming demands for micro parts in new technologies have required a variety of smaller components used in different fields, from entertainment electronics to biomedical implants [3][4]. Micromachining became increasingly important to produce micro parts. Also, the convenience and value of a range of products can be raised by reducing the size and weight of its components. Thus, micromachining techniques have become the new trend of miniaturization of cutting-edge technologies [4].

Furthermore, micro parts usually have size of a couple of millimeters, but if we consider micro range from 1 µm to 500 µm so there are many features that can be filled in that. Features size of 100 µm is common in micromachining – this means small as hair size, which presents such small diameter. Considering medicine and surgical procedures, new studies of the micromachining process shows that micro-cutting processes are not challenging just by reducing size of the conventional cutting technology, but it requires adjustments and control of all processes in the micromachining setup. These technologies are perceived as key technologies for future and some of them are already bringing about completely different ways to interact with the physical world. Industrially speaking, the interest in microscopic scale manufacturing is rapidly increasing due to the fast growth of the named Micro Electro Mechanical Systems (MEMS) research [3]–[7].

All types of lasers can be used for electronic or structural changes, although it has consequences. To illustrate this situation, Figure 2 shows a comparison between nanosecond and femtosecond laser ablating the surface of the material.

Figure 2 - Comparison between nanosecond and femtosecond laser ablation processes

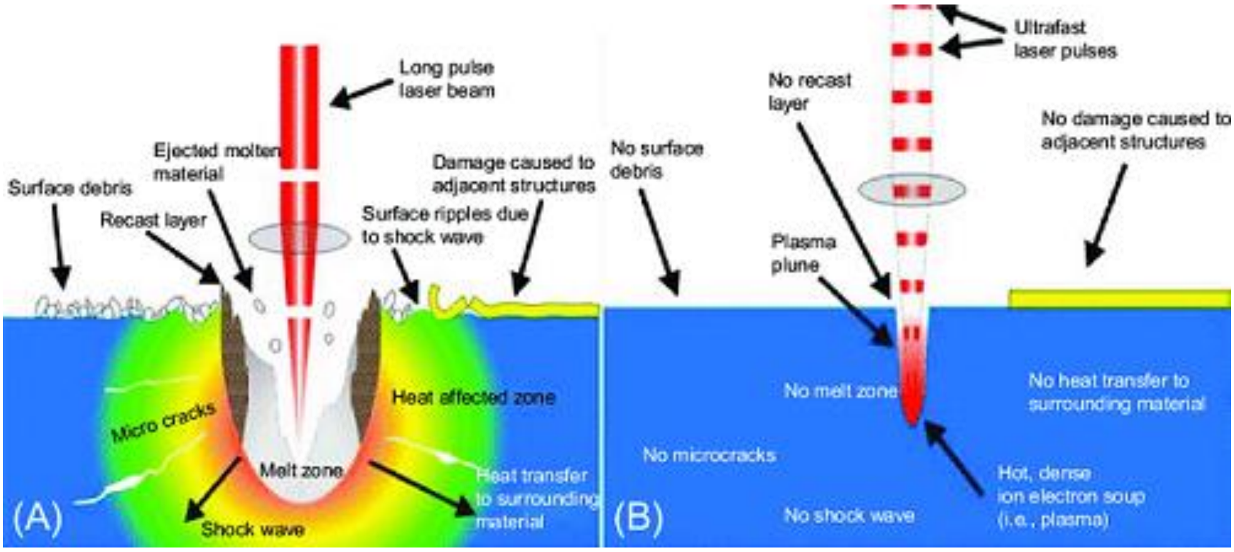

Source: [8].

Caption: (A) Nanosecond pulse laser ablation causes more damage in the round spot area such as shock waves, micro cracks and lots of heat.

(B) Femtosecond pulse laser ablations offers higher resolution because there are no damage in the round spot area.

In Figure 2, the laser beam is both represented by the incident red lines, which are sliced to illustrate the pulse duration. Besides, the yellow line represents a very tiny surface. Looking at picture (A), we can see that the drill hole is much larger than the one shown in part (B). This drilling hole in (A) causes secondary changes such as the melt zone and the ripples on the surface. Because of the pulse duration, the nanosecond interaction produces largely shock waves that propagate across the material generate heat, which leads to micro-cracks over the sample. We also see a large heat-affected zone around the focal volume.

On the other hand, the femtosecond interactions cause no melt or heat zone, which leads to a more condensed and high-resolution change that occurs strictly where the focused beam reaches the sample. In part (A) though, the surface is wholly destroyed, whereas in (B) the yellow line remains intact. All these differences presented until now are widely investigated by researchers to determine which kind of pulse duration works better for a specific and desired change.

In this context, the aim of this dissertation is to explain the design of an optical setup to microfabricate optoelectronic devices. Thus, the first optical setup developed in our lab was the laser micromachining technique. At the Laboratory of Optical Spectroscopy and Photonics (LEO&F) we have used a Q-switch Nd:YAG laser – an English acronym for **N**eodymium **d**oped **Y**ttrium **A**luminium **G**arnet – with a temporal duration of 1.2 ns (provided by the manufacturer) operating at low repetition rate (ranging from 10 to 2000Hz) tuned at 1064 nm and converted into a 532 nm after a second-harmonic generation crystal. In our experimental system, the fundamental laser goes through a second harmonic generator crystal where the conversion of frequency from 1064 nm to 532 nm occurs. After that, three dielectric mirrors are used to put the laser on the right way to reach inverted microscopy containing a 3D translation stage and, at the same time, to remove the 1064 nm residual laser. Also, two lenses are added as a telescope to enlarge in about 2-3 times the laser spot size, which is needed to cover the entire microscope objective entrance. We have employed 10x, 20x, and 40x microscope objectives. Consequently, the fully covered entrance makes possible the maximum intensity and smallest beam waist, providing higher resolution.

Furthermore, the sample moves over a 3D translational stage, which is controlled by dedicated software developed in our research group. In other words, the x and y-axis are responsible for moving the material horizontally as well as the z-axis controls the focus of the laser beam, in which the focal volume precisely reaches the point we intend to microstructure.

This micromachining setup was also equipped with some homemade features that helps to achieve better results. To say so, I point out the electronic system to control the motor-driven stage with stepper-motors and the shutter, which controls the passage of light throughout the system. The shutter, also linked on the electronic setup, closes its aperture when the sample is not being machined. Thus, the setup was set by considering a range of possible applications in a short future. However, to attest to the well-functioning fo the system, we had to try on some different materials and compare such results on the literature. Initially, we have worked on microfabrication tests over films produced with PMMA (polymethyl methacrylate), dopped with azo chromophores, and quantum dot films. Firstly, we aimed to obtain the threshold energy necessary to start modifying the specimens. Secondly, lines were structured on the surface’s sample to get more information about how laser energy may change the material’s properties or even cause ablation.

This thesis, therefore, was organized as follows: First, an overview of the theoretical background is presented, followed by short descriptions of its applications. Secondly, we show how the setup was designed and tested, at the first moment, for gold and chitosan substrates as calibration tests. On the sequel, besides gold and chitosan results, the setup was enhanced to obtain a better resolution in micromachining, where to do so, we used polymer-based films dopped with azo compound films with a flat surface to machine and test once more the capabilities of our optical setup. Finally, perovskite quantum dot thin films were also machined. The results showed very promising ways to reach other trails.

2 HISTORY AND APPLICATIONS OF LASER

The history of all significant developments that have brought successful laser technology until now is too long to be described in this short chapter. Still, the laser discovery celebrated its 60th anniversary, in the year of 2020, since Theodore Maiman showed the first laser functioning to the world [9]. Since that event, many important facts and researchers contributed to achieving new and shorter scales of laser pulses duration that are available nowadays. Maiman's laser was already a nanosecond pulse duration. Besides the laser came up in 1960, years later, pulses shorter than 100 fs (femtoseconds) were first achieved by Fork, Greene, and Shank, in the Bell Telephone Laboratories located in New Jersey (USA) [10]–[15].

Figure 3 - Theodore Maiman's first laser

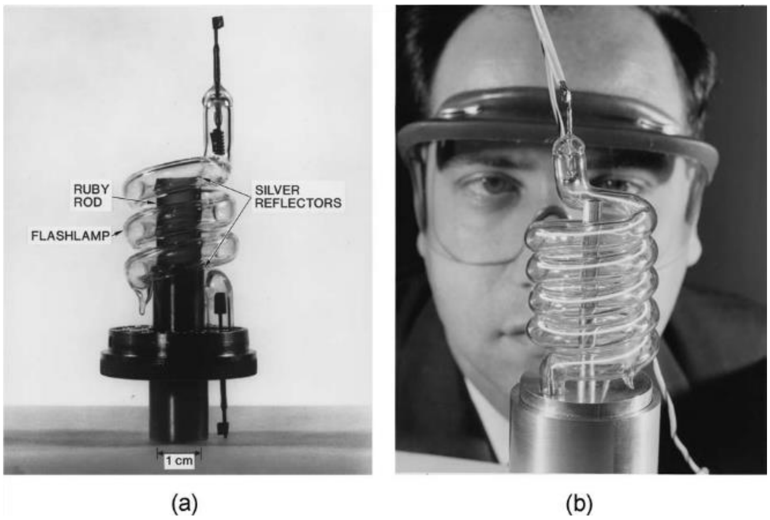

Source: [9].

Caption: (a) First laser invented by Theodore Maiman which was a nanosecond pulse ruby laser.

(b) Theodore Maimam behind his laser invention.

In 1960, on December 12nd, Ali Javan, William Bennett, and Donald Herriott got their accomplishment on the first helium-neon laser [9]. They had to build and align a kind of high-reflective cavity about a meter longer than Maiman's to get low-gain to finally succeed in their first gas laser experiment.

Few decades ahead, in 1997, pulses as short as five femtoseconds were reached by a solid-state Ti:Sapphire laser [16]. The current record for ultra-short pulse duration was only achieved by Chang’s group in 2012 with pulses shorter than 67 attoseconds (as) [17]. Further, a resumed timeline is shown in Figure 5.

As time has gone by, many other researchers started looking carefully for the range of possible applications of laser technology in general. One of Maiman’s assistant named Irnee D’Haenens once joked that the laser was “a solution looking for a problem” [9]. The laser was not a factual invention. The fact is that it was more discovery that an invention.

Figure 4 - (from left to right) Donald Herriott, Ali Javan, and William Bennett pose with the first helium-neon laser at Bell Labs. The beaker in Herriott’s hand contains a celebratory liquid

Source: [9].

Figure 5 - Timeline of ultra-short pulse laser micro/nanostructuring and other related works

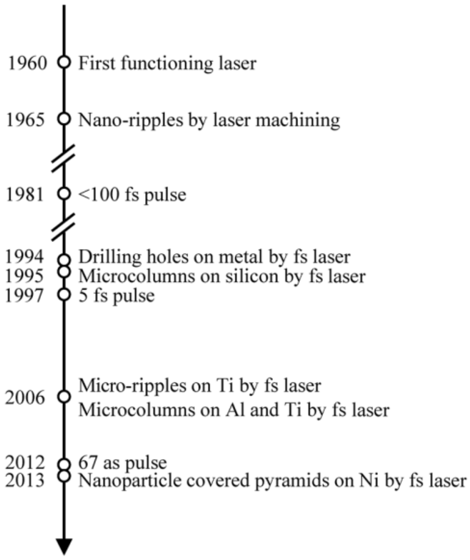

Source: [16].

Nowadays, many technological applications have laser as part of it. Thus, to cite a few of these applications, we can highlight waveguides, active devices, filters and resonators, and polymerization, slicing, surgeries and CD reading (no longer used). There is a short description of each of these applications as follows.

2.1 WAVEGUIDES

Waveguides were first demonstrated in the 1990s, where some structured lines presented features and worked as optical fibers. In photonic applications and it was one of the first demonstrations of potentialities of femtosecond laser micromachining[18]. Femtosecond laser-micromachined waveguides can be used as interconnections and conductors in a variety of glasses, and have opened up new possibilities.

Over the past twenty years, the transmission losses, refractive-index contrast, and bending radii of micromachined interconnects have been characterized to cite few features studied in this field [1]. Additionally, minimum bending radii such as order of tens of millimeters decreases have been achieved. Today photonic-circuit is being designed to be constructed using such waveguides as interconnections across the sample, which may go through many kinds of materials.

The waveguides are constructed by focusing the laser spot inside the material. Commonly, the used material is a transparent glass that may be doped with other substrates or not, depending on the results desired. In this case, the waveguides are produced by nonlinear optical effects. The laser beam goes through a microscope objective that moves over a 3D motion stage where the z-axis is usually used to control the focus. The other stages, however, are used to translate the glass sample according to the design intended. It is important to emphasize that a change in the refractive index has to be caused to promote the guidance of light and information along the modified line [18]. Also, the experiment shall be set to correlate the speed of translation to the expected modifications. If the energy is kept still, and the speed of translation is increased, smaller will be the interaction between the laser and the sample [19]**.**

Figure 6 shows a schematic way to fabricate waveguides. The inset shows the microscope image of the cross section of the cladding waveguide.

Figure 6 - Schematic representation of a waveguide fabrication with a microscope picture of the cross section shown in the upper-left side

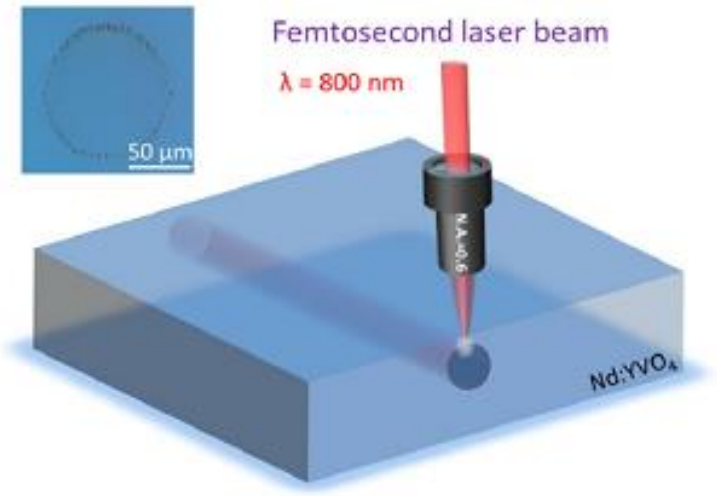

Source: [19].

2.2 ACTIVE DEVICES

The active devices are an optical gain category. For instance, femtosecond micromachined amplifiers are active devices such as the waveguides itself, since it is used to obtain a specific rate of gain. To achieve such a device, not only glasses have been used to be micromachined.

Waveguides machined inside electro-optical crystals are more often used as active devices than those fabricated in glasses. For instance, Brazilian researchers have reported the fabrication of waveguides in Gorilla Glasses and organic crystal of L-Theorine that has presented spectral broadening as well as white-light generation. According to these works, the new frequencies generated by the crystal happened because of the self-phase modulation and stimulated Raman scattering, where those effects are related to third-order nonlinear effects from this kind of glass [20].

Another interesting application showed recently in waveguides is the nonlinear conversion frequency in lithium niobite, which presents an efficiency of 49 % in SHG made over a crystal with about 9 mm length [1].

2.3 POLYMERIZATION

Polymerization is also an interesting application. Until now, I have just discussed how the laser can modify a sample or cause changes in the refractive index. However, polymerization is somehow the opposite of that. Instead of using a laser beam focused on modifications, the pulsed laser can cause polymerization induced by two-photon absorption process in a resin. In this way, the resin will be solidified over the laser path [21].

Also known as “two-photon polymerization”, this technique allows fabricating high complexity structures. As the laser goes through the resin located in a recipient, the photo-polymerization happens to create the desired structure. Many applications of this technique are exceeding the photonics field, and a lot of working has been reported [22][23]**.** Figure 7 shows a schematic representation of the polymerization process. First, the laser pulses are focused by an objective microscope lens.

Figure 7 - Schematic of the fabrication process by photopolymerization

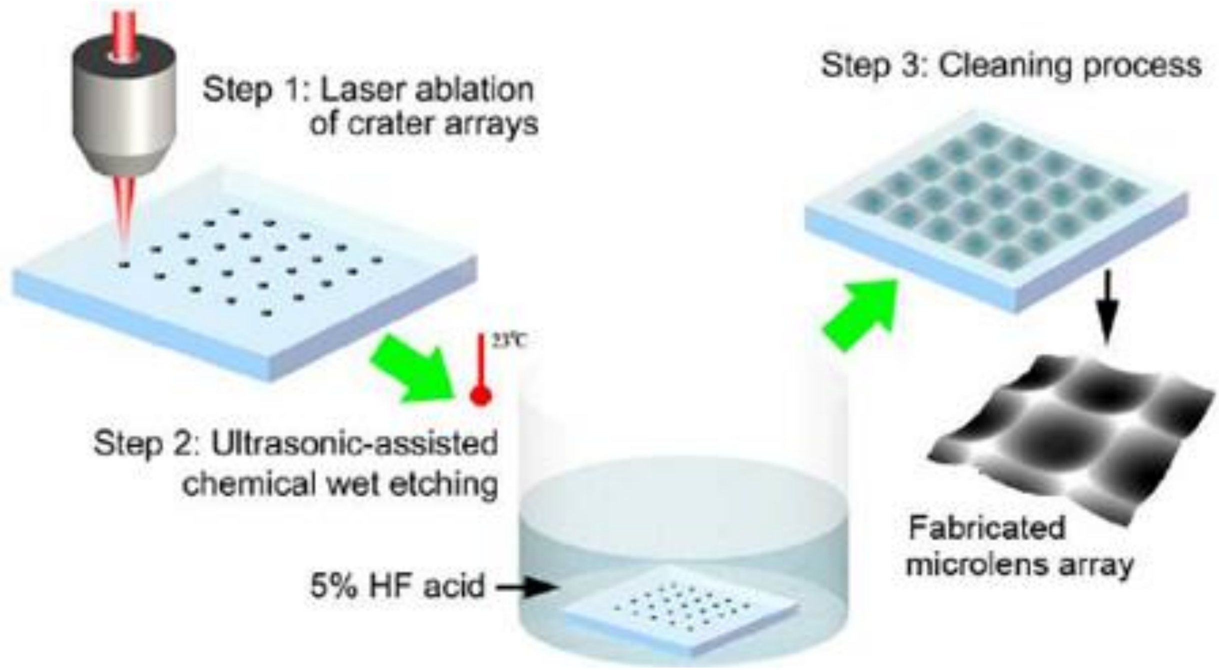

Source: [24].

The specimen is treated by a chemical etching process. At the end, the sample is cleaned by a bath in acetone, alcohol, and deionized water, respectively. For example, in Figure 8 shows 3D quadratic and hexagonal microstructure forms produced by this technique.

Figure 8 - Example of applications from the photopolymerization technique

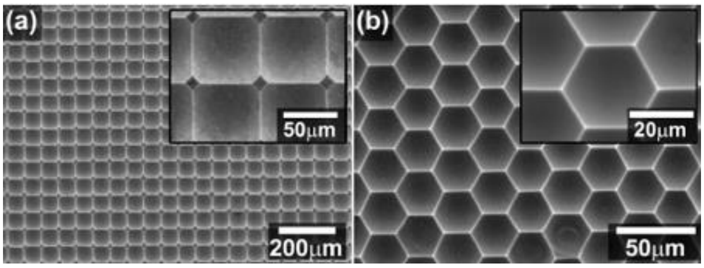

Source: [24].

Caption: (a) quadratic patterns produced by photopolymerization.

(b) Hexagonal patterns produced by photopolymerization.

3 NONLINEAR OPTICS

Nonlinear optics is the basis of modern photonics. The nonlinear phenomena allow us to reach an unusual regime of physical, optical, and electronic effects that would be unreachable if using only “natural or low-intensity sources” of energy [25]. Such a regime is possible by intensifying the electric field to the second, third, or even fourth, as shown next. However, to reach such amplitudes, a powerful source of energy is required. Thus the pulsed laser plays a major role in this because their light intensities make it possible to achieve, both due to its high field energy and the number of photons they turn available as a source of energy. It leads, among other things, to make possible the usage of pulsed lasers from nano to femtosecond time durations regimes.

The nonlinear optical regime differs from the linear regime by the amplitude of the electromagnetic field that interacts with the media. In the linear regime, this amplitude is presented many orders of magnitude smaller if compared to the interatomic electric field created in the atom. For instance, a continuous-wave laser usually produces electric fields on the order of 10^4 while the interatomic field is about 10^8, which give difference of about ten thousand times stronger. Moreover, the linear and nonlinear optics responds to different kinds of induced polarization with respect to the electric field. In other words, the dependency on this induced polarization can be linear or nonlinear.

Comparing these two types of polarization, the linear polarization $\vec{P}$ is related to the electric field, $\vec{E},$ by the following expression,

$$\vec{P}= \varepsilon_0 \chi \vec{E} \tag{3.1}$$

where ε_0 is the vacuum permittivity, and χ is the electric susceptibility of the medium. On the other hand, a Taylor expansion form in which the electric field appears followed by consecutive orders of electric susceptibility such as relates the nonlinear polarization to the electric field as,

$$\vec{P}= \varepsilon_0 \chi^{(1)} \vec{E} + \varepsilon_0 \chi^{(2)} \vec{E}\vec{E} + \varepsilon_0 \chi^{(3)} \vec{E}\vec{E}\vec{E} + \cdots \tag{3.2}$$

To put it another way, the first term of the Eq. with $\chi^{(1)}$ expresses the linear relation between $\vec{E}$ and $\vec{P}$ only [26][27] Besides, the other terms until the j-th term express the nonlinear dependency between $\vec{E}$ and $\vec{P}$. The second term and third terms, for instance, relate the second and third-order effects, respectively. Second-order effects are related to the electric field square, as well as third-order ones, are dependents on the cubic of an electric field. Therefore, Eq. (3.2) for polarization may be written as

$$\vec{P}=\overrightarrow{P_L}+\overrightarrow{P_{NL}} \tag{3.3}$$

Specifying the linear and nonlinear polarization, respectively, and making the linear optics as a particular case within the more general nonlinear optics.

In spite of explaining the polarization, it is also needed to approach the general explanation for the wave Eq. in a nonlinear material. Thus, it is possible to derive an appropriate wave equation from Maxwell's equations, whereas it depends only on the electric field. Thus, considering Maxwell's equations given by:

$$\nabla.\vec{D}=\rho \tag{3.4}$$

$$\nabla.\vec{B}=0 \tag{3.5}$$

$$\nabla\times\vec{E}=-\frac{\partial\vec{B}}{\partial t} \tag{3.6}$$

$$\nabla\times\vec{B}=\mu_0\left(\vec{J}+\frac{\partial\vec{D}}{\partial t}\right) \tag{3.7}$$

In which $\vec{D}$ is the electric displacement that describes the response of the medium due to the external electric field. Also, the electric displacement $\vec{D}$ can be expressed by

$$\vec{D}=\varepsilon_0\vec{E}+\vec{P} \tag{3.8}$$

Given such mathematical formulas, a very general wave equation for a medium can be obtained by simply taking the curl on the Eq. (3.6). For a better understanding, when the vector identity $\nabla \times \left(\nabla \times \vec{E}\right) = \nabla(\nabla \vec{E}) - \nabla^2 \vec{E}$ is applied to Eq. (3.6) and using both Eqs. (3.7) and (3.8), it is now possible to write equation (3.9) as:

$$\nabla^2 \vec{E} - \frac{1}{c^2}\frac{\partial^2 \vec{E}}{\partial t^2} = \frac{1}{\varepsilon_0 c^2}\frac{\partial^2 \vec{P}}{\partial t^2} \tag{3.9}$$

It is worth mentioning that in this situation, there are no free charges in the medium [26][27]. Moreover, c is the speed of light and may also be shown as $c = 1/\sqrt{\mu_0 \varepsilon_0}$ in which μ_0 is the magnetic permeability and ε_0 is the electric permittivity of the vacuum.

The energy of an optical beam, such as lasers, can be expressed in terms of the Poynting Vector given by

$$\vec{S} = \frac{1}{\mu_0}(\vec{E} \times \vec{B}) \tag{3.10}$$

It is a vector pointing on the direction of energy flow, as well as its magnitude, provides the power transported through a surface with unit area perpendicular to the direction of energy flow. Thus, the units of the Poynting Vector are $[S] = \left[{}^{W}\!/_{m^2}\right]$ – this quantity will appear later when the description of our system comes up.

Another key thing to remember is the refractive index called n. For the medium studied above, we can show the refractive index following the basic geometrical optics in which $n = {}^{c}\!/_{v}$, taking c is the speed of light in the space, and v is the speed of light in the media. However, it was already shown that $c = 1/\sqrt{\mu_0 \varepsilon_0}$. Thus, this relation leads to

$$c = \frac{1}{\sqrt{\mu_0 \varepsilon_0}} \tag{3.11}$$

$$n = \frac{c}{v} = \sqrt{\frac{\mu\varepsilon}{\mu_0 \varepsilon_0}} \tag{3.12}$$

$$n = \sqrt{1 + \chi} \tag{3.13}$$

in which χ is the electric susceptibility.

Right now, considering a nonlinear medium and taking the facts that a nonlinear material responds in a nonlinear way to any applied electric field, we may rewrite the equation (3.9) as

$$\nabla^2\vec{E} - \frac{n^2}{c^2}\frac{\partial^2\vec{E}}{\partial t^2} = \frac{1}{\varepsilon_0 c^2}\frac{\partial^2\vec{P}_{NL}}{\partial t^2}, \tag{3.14}$$

in which we also included the relation of the refractive index given by (2.13) [23][24]. According to this equation, the right-hand term – the nonlinear polarization – acts like a source generating such a new electric field. In the same way, when talking about nonlinear optics inside a medium, two or more waves are often considered in the interaction, in which such waves might have the same or different frequencies [20].

3.1 THE NONLINEAR RESPONSE OF A MEDIUM

Nonlinear responses occur when $\chi^{(2)}$, $\chi^{(3)}$ and its higher orders are detected and accessed in an experiment. So, taking these two examples – which are the most common to be studied, this relation can be better viewed in a graph, in which is represented by Figure 9 and it shows how the polarization interacts with electric fields.

Figure 9 - The curves show a graphic form of the interaction between P and E. Linear relation produces a straight line. Nonlinear regime produces a distorced line

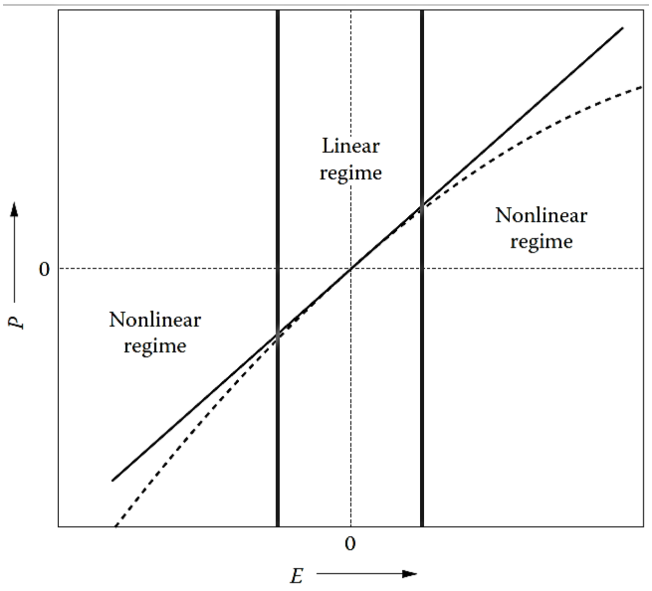

Source: [28].

In the same way, imaging how the electric field oscillates in time, a very typical scenario is given by Figure 10. In the sequel, following the idea of imaging the oscillation of $\vec{E}$, it also represented the oscillation of $\vec{P}$ as a function of time.

Figure 10 - Schematic representation of a time-oscillating electric field and different response for different mediums

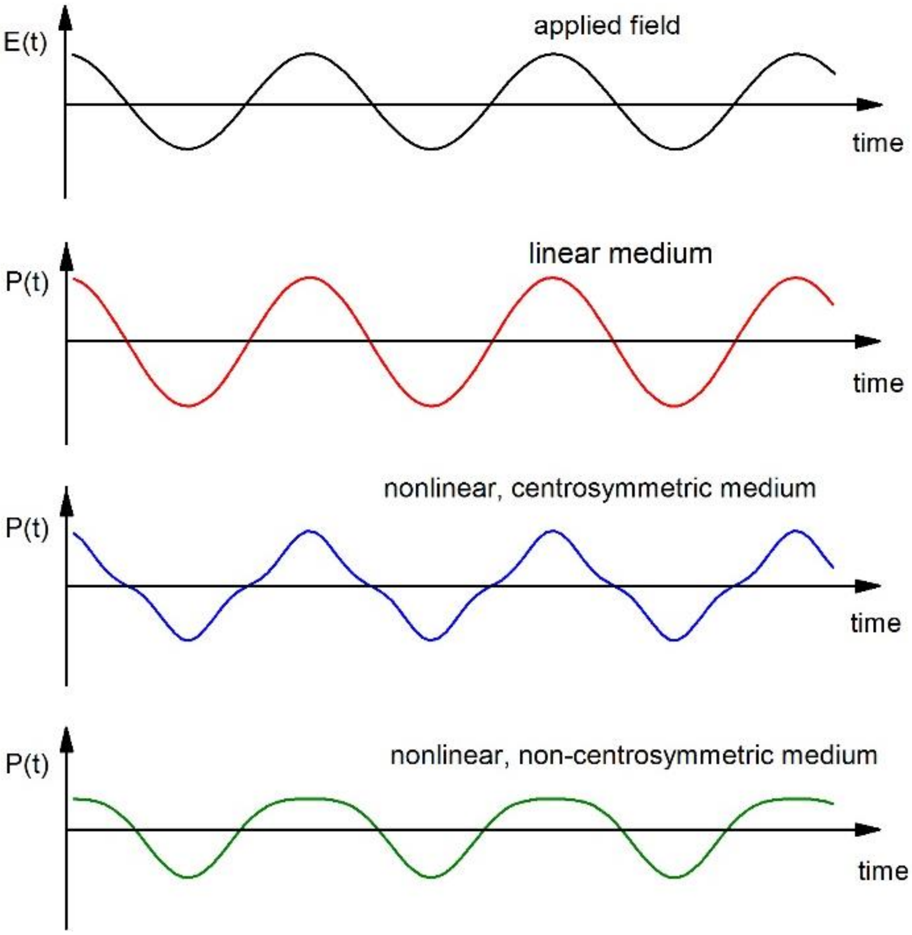

Source: [26].

Thus, the red line explores a bit more the relation between $\vec{E}$ and $\vec{P}$, as expected, presents the same pictorial curves due to its linear correlation. Furthermore, the cubic relationship in blue shows polarization P as a function of time for a nonlinear and centrosymmetric medium, whereas the polarization oscillates in a cubic form curve. Finally, the second-order in green is presented in a curve illustrated for a nonlinear but non-centrosymmetric medium.

3.2 SECOND HARMONIC GENERATION

In the field of nonlinear optics, always a nonlinear susceptibility is associated with a nonlinear phenomenon. In this way, we shall briefly present one aspect that is essential to the studies of nonlinear effects. This event is named Second Harmonic Generation (SHG), and it is crucial to explain the experimental setup in the later chapters.

To start so, let us consider a laser beam incident upon a crystal, which has a nonzero second-order susceptibility $\chi^{(2)}$. In this situation, the electric field strength may be written as

$$\tilde{E}(t) = Ee^{-i\omega t} + c.c. \tag{3.15}$$

the nonlinear polarization, therefore, is created in the crystal and it is given explicitly as

$$\tilde{P}^{(2)}(t) = 2\varepsilon_0\chi^{(2)}EE^* + (\varepsilon_0\chi^{(2)}E^2e^{-i2\omega t} + c.c.), \tag{3.16}$$

in which the second-order polarization is composed of a term (first) that does not depend on the frequency, while a 2ω frequency comes up in the second term, indicating the generation of a new frequency that occurs inside the crystal. It can also be said as “generation of radiation at the second-harmonic frequency” [29].

Figure 11 shows a schematic SHG. In part (a), a photon with frequency ω interacts with a SHG crystal and, as a result, the photon of frequency 2ω is created with half-wavelength that leads to the double of energy. It is important to highlight that the ω-output frequency occurs due to the not full conversion efficiency of the SHG crystal.

It is required to have good phase-matching to achieve high conversion of frequence. Under proper experimental conditions of phase-matching, the process of second-harmonic generation can be so efficient, whereas almost all of the power coming from the incident beam at ω-frequency is converted to radiation at the second-harmonic 2ω-frequency [29].

Figure 11 - Schematic geometry of second-harmonic generation and an energy-level diagram describing second-harmonic generation

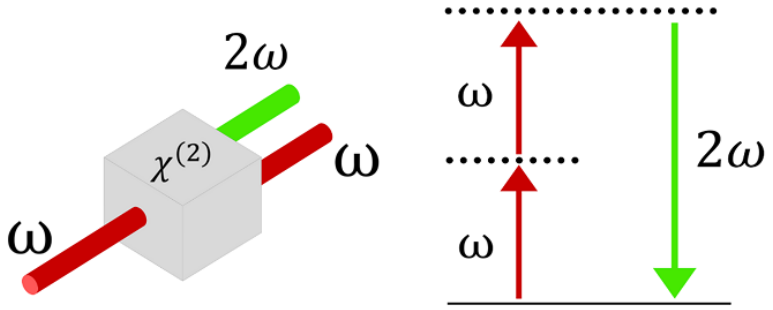

Source: Author.

The second-harmonic generation can also be visualized by considering the interaction in the exchange of photons on the various frequency components of the field. According to this, as illustrated in part (b) of Figure 11, two photons of frequency ω are destroyed, and a photon of frequency 2ω is created in the process. The bold black line represents the atomic ground state, as well as the dashed line, which describes what is known as virtual levels.

3.3 TWO-PHOTON ABSORPTION

Two-Photon Absorption (2PA) is a nonlinear optical phenomenon in which two-photon – not necessarily with the same frequency – are absorbed simultaneously by an atomic system or molecule in a quantum event. Besides, it is a non-resonant phenomenon, herewith, the energy of the incident photon $\hbar\omega_f$ is always smaller than an electronic transition energy ($\hbar\omega_{\text{transition}}$).

Figure 12 shows a schematic representation of this situation. As can be noted, two different photon energies, when summed, reach the same energy level named $|1\rangle$. Thus, it does not matter the energy of the photon itself. What does matter indeed is the sum of the energies has to be equal to the transition energy, in which the first photon reaches what is called a virtual state.

It is essential to point out that, to occur 2PA process, we need a laser with such short temporal duration to make sure that in a very short interval, two or more photons will target the atom before it “relaxes” and dispose of the energy.

To illustrate this process, let us take two photons with a wavelength of 600 nm presents the same energy a single photon wavelength of 300 nm. Besides, two 1064 nm photons have the same energy of one 532 nm wavelength photon.

Figura 12 - Schematic representation of the Two-Photon Absorption (2PA) process

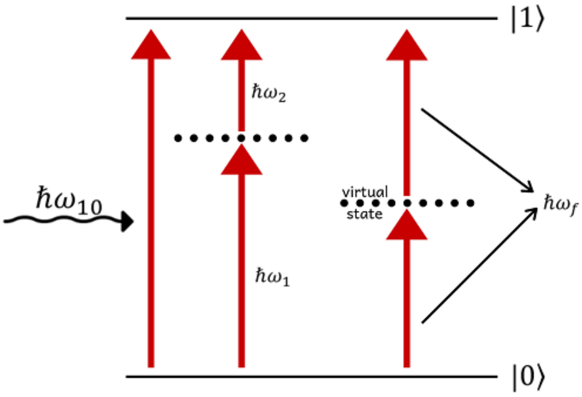

Source: Author.

As said before, the flux of photons has to be the one whereas both photons are absorbed in the same quantum event – Heisenberg's Uncertain Principle rules such event. In this case, the virtual state shown in Figure 13, has a lifetime given by:

$$\Delta \mathrm{E} \Delta \mathrm{t} \geq \frac{\hbar}{2} \tag{3.17}$$

$$\Delta \mathrm{t} \geq \frac{\hbar}{2\Delta \mathrm{E}}, \tag{3.18}$$

in which $\Delta \mathrm{E}$ is the energy of transition.

To give an example of this principle applied in the virtual state, let us consider an energy transition of 2eV. Figure 13 shows a schematic for that.

Figure 13: Schematic representation of a 2 eV energy trasition.

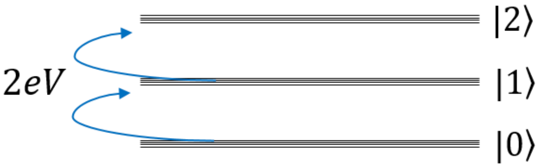

Source: Author.

Thus, equation (3.18) by putting the right values, gives us:

$$\Delta t \geq \frac{6{,}62 \times 10^{-34} J.s}{4\pi(1{,}6 \times 10^{-19} J)} \tag{3.19}$$

$$\Delta t \approx 10^{-15} s \tag{3.20}$$

Thus, it is impossible to observe this phenomenon with a continuous-wave laser, only with a pulsed laser [30].

Using the nonlinear Law of Beer given by

$$\frac{dI}{dz} = -\alpha I, \qquad \text{in which } \alpha = \alpha_0 + \beta I \tag{3.21}$$

here, α_0 is the linear coefficient of absorption, and β is the two-photon coefficient of absorption. In this way, we may rewrite Eq. (3.21) to have

$$\frac{dI}{dz} = -(\alpha_0 + \beta I)I \tag{3.22}$$

However, β is not an intrinsic parameter of any material. This Eq., when solved by integration in time and space, leads to a scattering section given by

$$\sigma_{2PA} = \frac{\hbar\omega\beta}{N} = [GM] \tag{3.23}$$

Finally, to end this section, it is essential to say that materials that present a 2PA cross-section higher than 1000 GM are more considered to be studied.

3.4 THE KERR EFFECT (NONLINEAR REFRACTIVE INDEX)

As we already know, high intensities light causes nonlinear effects when it propagates through a medium. One of these effects is named Kerr Effect, which describes a change in the refractive index that, in turn, is related to the optical intensity [26].

To explain this change in the refractive index, let us consider an isotropic, centrosymmetric medium ($\chi^{(2)} = 0$) with a monochromatic electric field E. Hence, we can overlook the second-order susceptibility. Thus, recalling the equation (3.1), it can be written as

$$\vec{P}= \varepsilon_0 \left[\chi^{(1)} + 3\chi^{(3)} \left|\vec{E}(\omega)\right|^2\right] \vec{E}(\omega) \tag{3.24}$$

However, $\chi^{(3)}$ has a real and an imaginary part. The real part is the refractive index, while the imaginary one is the coefficient of absorption. As a result, $\chi^{(3)}$ can be expressed as

$$\vec{P} = \varepsilon_0 \chi_{\mathrm{eff}} E(\omega) \tag{3.25}$$

in which we have introduced the effective susceptibility given by

$$\chi_{\mathrm{eff}} = \chi^{(1)} + 3\chi^{(3)} \left|\vec{E}(\omega)\right|^2 \tag{3.26}$$

Although the refractive index depends on the intensity of light for many materials, the refractive index, for this reason, can be written as

$$n = n_0 + \bar{n}_2 \langle \tilde{E}^2 \rangle \tag{3.27}$$

in which n_0 represents the usual refractive index for linear responses or for low intensities. On the other hand, $\bar{n}_2$ is the nonlinear refractive index derived from the Kerr Effect. As we can see, $\bar{n}_2$ gives the rate at which the refractive index grow according to the intensity of the electric field. Also, it important to say that the bar over the second term in equation (3.27) is that just to emphasize another kind of index – the nonlinear, in this case.

Relating the nonlinear susceptibility $\chi^{(3)}$ with the nonlinear refractive index $\bar{n}_2$, we may express such relation as

$$n^2 = 1 + \chi_{\mathrm{eff}}, \tag{3.28}$$

in which is very similar to the equation (3.13) presented before. As a result, the nonlinear refractive index is given by

$$n_2 = \frac{3}{4n_0^2\varepsilon_0 c}\mathrm{Re}\{\chi^{(3)}\} \qquad (3.29)$$

Here again, only the real part of the third-order susceptibility represents the refractive index.

4 MICROMACHINING THEORY

Here, we present some of the most important concepts and variables present in the micromachining experiments. Some of these items are further explained and calculated in the chapter of results.

4.1 GROOVES, SPEED OF TRANSLATION AND BEAM WAIST

When we run trials in micromachining experiments, we set a couple of parameters that lead to a certain groove machined over the sample. These grooves can be measured, and some of the parameters in the experiment cause different wider or narrower lines. This section, therefore, discusses two of these parameters.

Firstly, on the path of the concepts presented in the last section, the beam waist is directly related to the numerical aperture of the microscope objectives. As a definition, the beam waist of a laser beam is the point along the propagation axis, in which the beam radius has its smallest value [31].

The laser beam presents some special characteristics. To define, Gaussian beams are those in which the electric field profile is perpendicular to the beam axis and is described by a Gaussian function. They are considered to have small divergences so that the named paraxial approximation can be applied [32]. This evaluation allows us to omit the term of second-order derivative in the wave's propagation equation (derived from Maxwell's equations), so, we end up with only a first-order differential equation results. For a monochromatic beam, propagating in the z-direction, the Gaussian beam equation is written as follows:

$$\Psi = E_0 \frac{w_0}{w(z)} \exp\left\{\frac{-r^2}{w^2(z)}\right\} \exp\left\{-i\left[kz - \eta(z) + \frac{kr^2}{2R(z)}\right]\right\} \tag{3.30}$$

Here, r is the radial distance from the center axis of the beam, z is the axial distance from the beam's focus (or "waist"), i is the imaginary unit, $k = 2\pi n/\lambda$ is the wavenumber (in radians per meter) for a free-space wavelength λ, and n is the index of refraction of the medium in which the beam propagates, E_0 is the electric field amplitude (or phase) at the origin at time zero, $w(z)$ is the radius at which the field amplitude fall to 1/e of their axial values, w_0 is the waist radius (beam waist) –

measured in µm , $R(z)$ is the radius of curvature of the beam's wavefronts at z, and finally, $\eta(z) = tg^{-1}(z/z_0)$ is named Gouy phase.

Figure 14 shows a representation of the beam waist along the propagation axis. From the figure, we can see that at the zero point, we have the smallest beam radius, or also called the beam waist.

Figure 14 - Representation of a Gaussian beam waist along the propagation axis

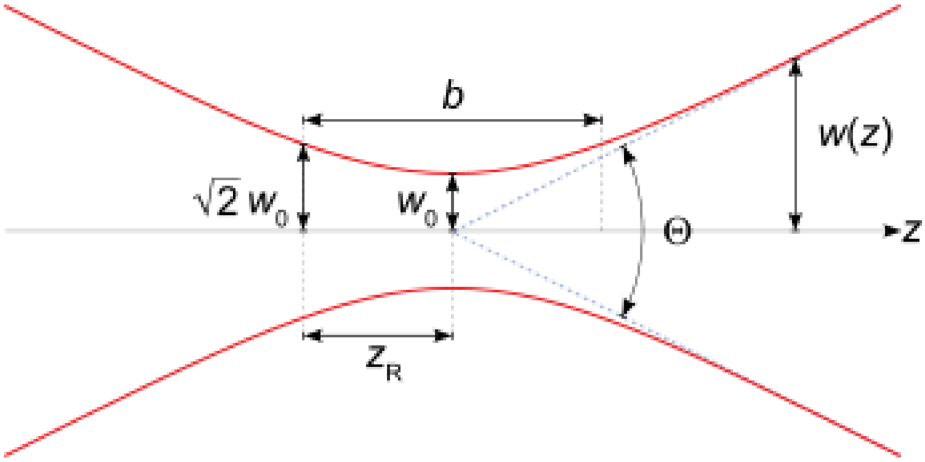

Source: [30].

One of the key factor here is the NA number of a microscope objective lens (see section 3.4.2.) works directly on the shape of the light cone by changing the focal plane of the light throughout the lens. Thus, higher NA values lead to a smaller beam waist, whereas the smaller NA values lead to a higher beam waist. In short, the smaller resolution values, in micrometers, indicates smaller beam waists. It means, in other words, that small resolution number provides narrower grooves machined in the experiment. Thus, the quality of the grooves, somehow, depends on the size of the beam waist targeted over the sample.

The beam waist can be evaluated from the following equation:

$$w_0 = \frac{n\lambda}{\pi NA}\sqrt{1 - NA^2}, \tag{3.31}$$

in which n is the sample's refractive index, λ is the wavelength and NA is the numerical aperture of the objective lens.

In micromachining experiments, the pulsed lasers are widely used. Theses laser presents a different number of pulses per second depending on the repetition rate set in the laser. The repetition rate is precisely the number of pulses per second – given in Hertz (Hz). In this way, we can set different repetition rates in the laser control, which, in turn, leads to a different number of pulses per second that target the sample. However, micromachining experiments also are widely controlled by an electronic setup coupled with the optomechanical components, in which one of its functions is to control the translation speed on the XYZ-stage.

Here, the translation speed gets a highlight function by changing the number of incident pulses over the specimen. When we set a certain speed in the electronic control, the XYZ-stage moves with this speed. A higher speed, therefore, implies fewer pulses reaching the specimen. Changing the translation speed rather than changing the repetition rate in laser control is that because it is safer and easier. In our lab, for instance, to change the repetition rate in the laser control, there is a protocol recommended by the manufacturer. First, the power and current have to be set down to zero. Next, you set the new repetition rate and set up the power and current again.

The important consequence of the speed feature on the experiment is the influence on the energy that reaches the sample and produces the groove. For example, by keeping the repetition rate constant in the laser control, by selecting different speeds on the electronic control, the number of pulses will also change. For instance, keeping the repetition rate in 2000 Hz, it means 2000 pulses per second. Hence, if we set up a translation speed as 25μm/s, we get many more pulses per second instead of setting up a speed of 100 μm/s or 200 μm/s.

The number of pulses can be calculated by the summation of intensities produced at a particular point. Hence,

$$N = \sum_{n=-\infty}^{\infty} e^{-\left(\frac{v_y}{f\,w_0}\right)^2 n^2} \tag{3.32}$$

Here, w_0 is the beam waist, v_y is the speed of translation, and f is the repetition rate of the laser[33]. The key to understand this equation is the argument of the exponential term because it refers to a corresponding value on the next figure. As can be seen in the figure 15 and evaluating $\frac{v_y}{f\,w_0}$ we are able to get the right number n that indicates the limits of such summation as written in equation 3.32.

Figure 15 - Convergence of the summation approximation in equation (3.32)

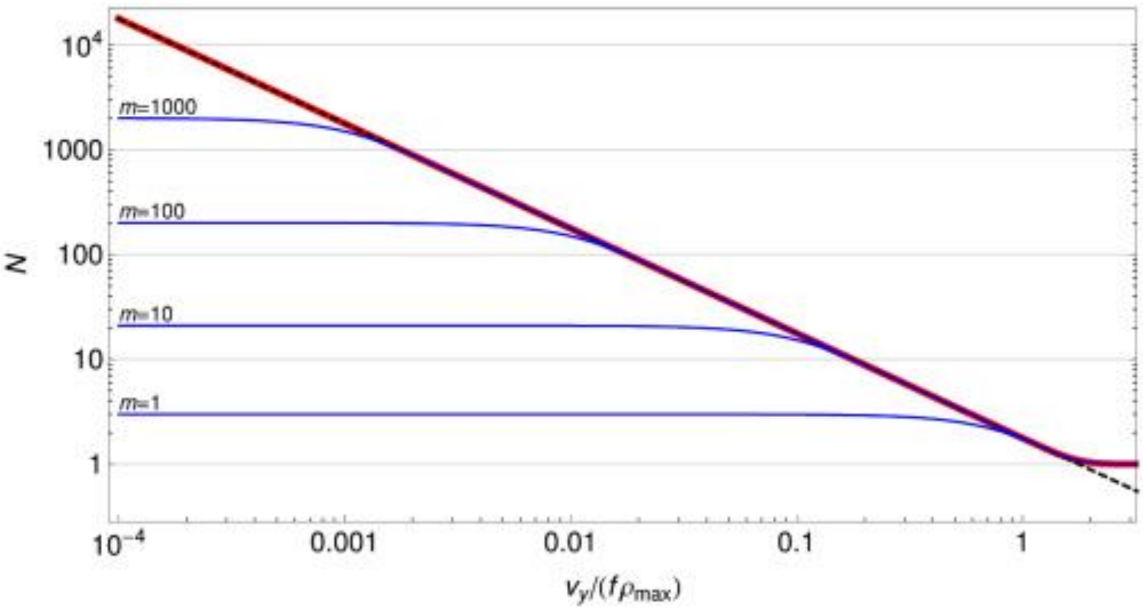

Source: [33].

Caption: The red line is the analytical function and the dashed lines is the arpproximation for small number derivated from equation 3.32.

Higher speeds cause narrower grooves if the laser power and repetition rate are kept constant. As said before, the small beam waists also produce narrower grooves. Thus, by combining the spot size in the waist with the translation speed, many different grooves, wider or narrower, can be machined. Results and clearer data are presented in chapter 5.

Last but not least, the number of pulses that reach the specimen is considered to be the number of pulses per spot. This number of pulses helps in understanding how the objectives, speed, and laser power set the ablated lines over the sample.

4.2 MICROSCOPE OBJECTIVES

Besides all the optomechanical components and features, the microscope objectives are essential for micromachining experiments. Its use is needed to focus the laser beam on the sample that is going to be modified. Thus, understanding its functioning is helpful to elicit data and comprehend micromachining features.

The objectives, for short, are original components of microscopes that are placed next to the sample. The objectives have an essential feature named Numerical Aperture (NA) - it is the key to working with it. The Numerical Aperture (NA) restricts the limits of how much narrow the laser spot will reach, and it also defines the resolution of the machined lines [34]. Besides the NA, different objectives present different focal distances, also known as working distance. Here, the working distance is the distance between the front surface of the lens to its front focal point where the laser beam is focused at a single point [35]. Figure 16 shows a schematic illustration of three different objective lenses with different NA and how their light cones are formed.

As can be seen from Figure 16, the NA determines the gathering of the light that goes throughout the objective. As can be noted further, a higher NA number leads to a higher angle that shapes the light cone. To put it another way, the angle formed between the black vertical line and the light cone is responsible for limiting the size of the laser spot that reaches the sample.

Furthermore, another critical feature that changes the NA, which next alters the light cone, is named *imaging medium*. It is the medium located between the front objective lens and the sample. For example, some microscope objective with a very high resolution uses oil.

Figure 16 - Illustration showing different NA and light cones for different microscope objectives

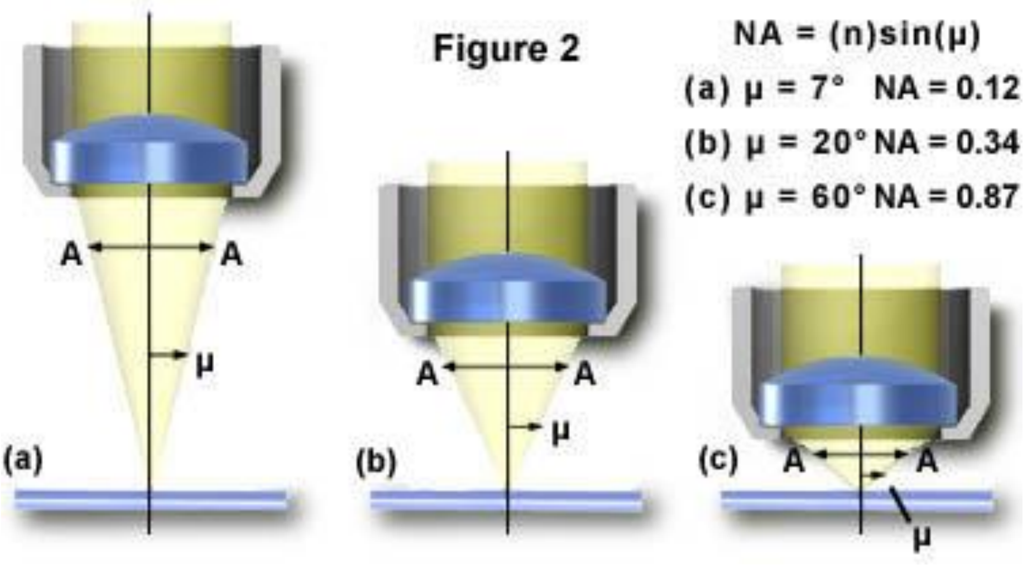

Source: [36].

The oil changes the refractive index of the imaging medium, which was air initially. Thus, by changing this refractive index, the NA will get higher values, and it leads to a wider angle forming a wider light cone and allowing such high resolution as presented by some 40x or above magnification numbers. In other words, the refractive index is the limiting factor in achieving high NA values. To give a better sight on this, equation 3.33 represents the NA calculation,

$$NA = nsin(\mu), \tag{3.33}$$

in which NA is the numerical aperture, n is the refractive index of the *imaging medium,* and μ is the angle formed between the vertical line and the light cone [36].

From equation 3.33 we see that when we work on the air – with a refractive index, **n** = 1.0, the numerical aperture depends only on the angle μ with maximum value is 90°. The term $\sin(\mu)$ has its maximum value of 1.0 for the angle of $90°$. This value is such the theoretical maximum numerical aperture of a lens placed in the air, which is also known as "dry" microscope objectives.

The NA of an objective is also dependent, somehow, upon the amount of correction for optical aberration – property from optical systems such as lenses that causes light to spread out some region of space instead of focus to a point. Most of the objectives are built with spherical surfaces and as it is strongly curved on its borders, which leads do spherical aberration when these lenses are used for imaging. Lenses with spherical aberrations can seriously degrade the quality of image [37]. When this kind of objective is used in lasers or other optical setups, it causes the laser beam to distortions. Thus, the higher is the correction in the objectives, the larger are the numerical apertures for the respective magnification, as illustrated in Table 1. As numerical aperture increases for a series of objectives with the same magnification, we may observe a greater ability to gather light, which corresponds to an increase in resolution.

Table 1 - Magnification of microscope objectives with different NA values

Magnification	Plan Achromat (NA)	Plan Fluorite (NA)	Plan Apochromat (NA)
0.5x	0.025	n/a	n/a
1x	0.04	n/a	n/a
2x	0.06	n/a	0.10
4x	0.10	0.13	0.20
10x	0.25	0.30	0.45
20x	0.40	0.50	0.75
40x	0.65	0.75	0.95
40x (oil)	n/a	1.30	1.00
60x	0.75	0.85	0.95
60x (oil)	n/a	n/a	1.40
100x (oil)	1.25	1.30	1.40
150x	n/a	n/a	0.90

Source: [36].

The most common objectives, widely employed on a majority of microscopes and optical experiments, are the achromatic objectives [38]. These objectives are corrected for axial chromatic aberration in two wavelengths, which are usually blue and red – about 486 and 656 nanometers, respectively. Furthermore, the same objectives are corrected for spherical aberration in the green region, about 546 nm. From Table 1, If we take typical 40x dry objectives as an example, we see that for flat-field corrected plan objectives, NA rises corresponding to correction for both chromatic and spherical aberration**:** plan achromat, NA = 0.65; plan fluorite, NA = 0.75; and plan apochromat, NA = 0.95. It illustrates that the aberration is also important to evaluate the gathering of light, which leads to smaller spot sizes. I point out, however, that all these numbers and features may differ from one manufacturer to another.

To give a better sight of these differences, it is necessary to look at the construction and lens composition of such objectives. Thus, Figure 17 shows how different lenses for the same 10x magnification are coupled together to fix chromatic and spherical aberrations depending on the incoming wavelength. From the figure, achromat lenses are less corrected than apochromat ones. The conjunction of such different curved lenses is able to compensate aberrations, which, in turn, leads to better resolutions. As said before, this increase in correction corresponds to an increase in

NA values for that objective. In addition, Table 2 presents the number of colors where such corrections are more effective in those objectives.

Figure 17 - Optical construction for different lenses correction considering the same magnification. Achromat lens is less corrected than Apochromat one

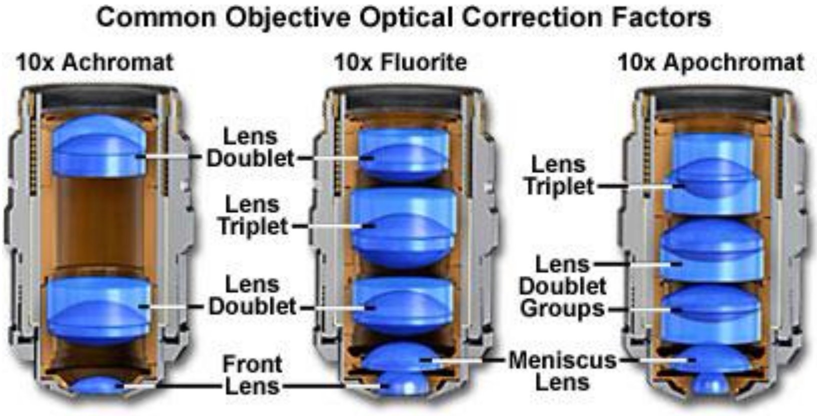

Source: [38].

Table 2 - Amount of colour (wavelengths) corrections for each type of microscope objective

Objective Type	Spherical Aberration	Chromatic Aberration	Field Curvature
Achromat	1 colour	2 colours	No
Plan Achromat	1 colour	2 colours	Yes
Fluorite	2 or 3 colours	2 or 3 colours	No
Plan Fluorite	3 or 4 colours	2 or 4 colours	Yes
Plan Apochromat	3 or 4 colours	4 or 5 colours	Yes

Source: [38].

As explained before, these features and corrections imply different image resolutions. Table 3 shows the resolution, in micrometers, for each NA correction for each of the most common magnification numbers.

From the table, we see important values that indicate how important is the corrections of those aberrations. Let us consider the 40x magnification, for instance. Plan-fluorite has a NA value of 0.75 and a resolution of 0.37 μm, whereas the Plan-Apochromatic presents a NA value of 0.95 and a resolution of 0.29 μm. It shows, for short, that, in spite of they are all 40x magnification objectives, the present different resolutions. Therefore, a small resolution number shows higher resolution for images, consequently, smaller grooves in micromachining experiments.

Table 3 - Image resolution, in micrometers, in relation to the NA correction

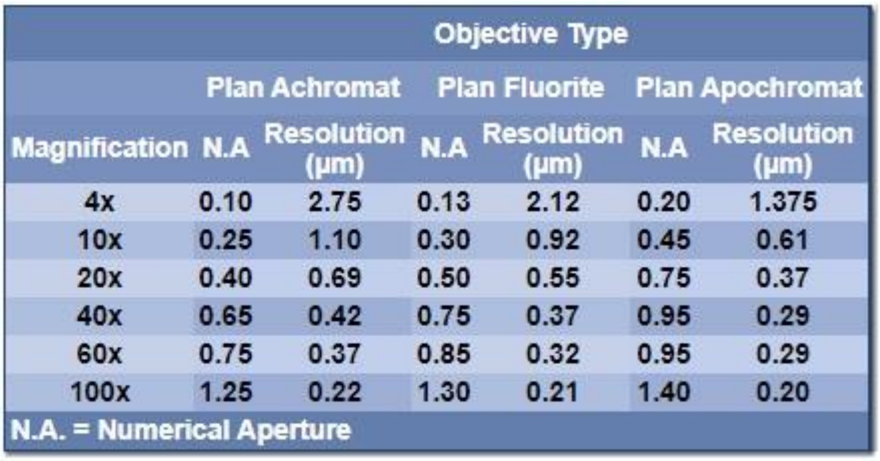

	Objective Type					
	Plan Achromat		Plan Fluorite		Plan Apochromat	
Magnification	N.A	Resolution (µm)	N.A	Resolution (µm)	N.A	Resolution (µm)
4x	0.10	2.75	0.13	2.12	0.20	1.375
10x	0.25	1.10	0.30	0.92	0.45	0.61
20x	0.40	0.69	0.50	0.55	0.75	0.37
40x	0.65	0.42	0.75	0.37	0.95	0.29
60x	0.75	0.37	0.85	0.32	0.95	0.29
100x	1.25	0.22	1.30	0.21	1.40	0.20
N.A. = Numerical Aperture						

Source: [34].

4.3 FLUENCE AND THRESHOLD FLUENCE

In physics, the fluence is defined as the flux of some radiation or particle stream that is time-integrated. Specifically, in the field of optics, the fluence – named **F** – from a laser pulse is the energy per unit area. Its most common units are written as J/cm^2 (joules per square centimeter). From the units, the fluence depends on the position value. For a Gaussian laser beam, for instance, at positions somewhat away from that axis the fluence is higher on the beam axis and lower. Fluence is meaningful only in combination with some irradiation time for continuous-wave beams [39]. Using the following equaions is possible to deduce the threshold fluence that indicates the smallest energy required to start modifying the specimen surface.

Following the unit information, the fluence is given by:

$$F = \frac{P}{f(\pi w_0^2)}, \tag{3.34}$$

in which P is the laser power set in the experiment. So, the ablation threshold fluence is related to the beam waist, the width of the grooves, as given by the equation below.

$$r^2 = \frac{w_0^2}{2} \ln\left(\frac{F}{F_{th}}\right) \tag{3.35}$$

in which r is the width of the groove, F is the fluence and F_{th} is the threshold fluence [40]. From the equation variables, we can measure the groove width experimentally with an open-source software named *ImageJ*. Thus, evaluating w_0 from equation (3.31) and using the values of F from equation (3.34), we can solve equation (3.35) for F_{th}.

4.4 HEATING AND THERMAL EFFECT

Different types of laser with different temporal pulse duration interact in many different ways with the materials. From the nanosecond to femtosecond range, we have some important characteristics that rule these interactions. A femtosecond pulsed laser can be used to produce high-quality and precise material processing due to the interaction between the pulse and the material that occurs over the timescale of the electron. On the other hand, longer pulse duration interacts with lattice because there is enough time to do so [41].

The short and quick interactions form the ultra-short pulses cause the material is ablated with a well-defined resolution area by minimizing both mechanical and thermal damages. In contrast, longer pulse duration, such as nanosecond ones, may heat up the material, producing shock-waves and causing mechanical and thermal damages on the target material. Here, the laser energy spreads throughout the lattice by heat conduction [8].

Today, it is possible to find existing research on laser-material interaction in which they show how different pulsed lasers can be used for material processing, especially in nanotechnology [42]–[44]. Moreover, little attention shall be given to the nanosecond laser interactions because it is the type of laser employed in this work.

Here, a revision and a reinterpretation from reference [8] and reference [45] are made. Laser ablation starts with photon absorption, followed by the heating of the target area by the laser beam. Aftermath, the heating will spread out the specimen leading to modifications and damages in different ways, as said before. Also, the amount of ablated material somehow depends on the absorption by the target sample.

The thermal energy can be transferred from the laser beam to the material according to the 1D or 2D diffusion models, in which it is considered to have a rapid thermalization in the electrons. Describing both lattice and electrons by their temperatures, we write

$$C_e \frac{\partial T_e}{\partial t} = -\frac{\partial Q(z)}{\partial z} - \gamma(T_e - T_i) + S, \tag{3.36}$$

$$C_i \frac{\partial T_i}{\partial t} = \gamma(T_e - T_i), \tag{3.37}$$

$$Q(z) = -k_e \left(\frac{\partial T_e}{\partial z}\right) + S, \tag{3.38}$$

$$S = I(t) A \alpha e^{-\alpha z}. \tag{3.39}$$

Here, we consider z to be the direction of propagation perpendicular to the specimen surface, taking $Q(z)$ as the heat flux, S is the laser heating source term, $I(t)$ is the laser intensity, $A = 1 - R$ with R being the reflectivity of the sample, α is the coefficient of absorption of the target sample, C_e and C_i are the electrons and lattice heat capacity per unit volume, respectively. Still, γ is the parameter characterizing the electron-lattice coupling, and k_e is the thermal conductivity of the electrons.

By coupling the equations (3.37), (3.38) and (3.39) we get a differential equation that describes both cooling dynamics for T_e and T_i, and also models the time evolution of the electron and lattice temperatures [37][38]. Thus, these equations can be now written as

$$C_e \frac{\partial T_e}{\partial t} = k_e \left(\frac{\partial^2 T_e}{\partial z^2}\right) - C_i \frac{\partial T_i}{\partial t} + I(t) A \alpha e^{-\alpha z} \tag{3.40}$$

As said before, the laser pulse duration has an effect over the material ablation threshold and on the penetration depths as well. By increasing the pulse duration, we increase the threshold fluence while it decreases the effective energy penetration. Here, we take the laser pulse duration much longer in comparison with the electron-phonon energy-transfer time, in which $(\tau_L \gg \tau_i)$, in which τ_L is the pulse duration. By this way, if we consider low laser intensities, the electron and the lattice have the same temperature $(T_e = T_i = T)$ [41]. In other words, when the pulse duration is long compared to the electron-phonon energy-transfer time, equation (3.40) reduces to

$$C_e \frac{\partial T_e}{\partial t} = k_0 \left(\frac{\partial^2 T}{\partial z^2} \right) + I(t) A \alpha e^{-\alpha z} \tag{3.41}$$

in which $k_0 = k_e(T)$ is the equilibrium thermal conductivity of the material.

In nanosecond laser interactions with the target specimen, the surface of the material is heated to the melting point or even reaching the vaporization temperature [8]. Meanwhile, energy is usually lost by heat conduction into the material lattice. Thus, the heat penetration l can be evaluated by $l \sim (D_t)^{1/2}$, in which D the heat diffusion coefficient and is given by $D = k_0/C_i$.

Furthermore, the energy transferred to the target material, written in terms of the mass can be expressed by $E_m \sim I_\alpha t/\rho l$, where ρ is density of the target By considering a specific time with $t = t_{th}$, this energy will be higher than the specific heat of evaporation Ω – when evaporation occurs, though. However, when $E_m \sim \Omega$ and after some driven calculations, we then have $t_{th} \sim D(\Omega \rho / I)^2$. Hence, the laser intensity can be written as

$$I > I_{th} \sim \frac{\rho \Omega D^{1/2}}{\tau_L^{1/2}}, \tag{3.42}$$

in which Ω is the specific heat of evaporation, D is the heat diffusion and τ_L is the pulse duration. Thus, the fluence can be expressed by

$$F > F_{th} \sim \rho \Omega D^{1/2} \times \tau_L^{1/2} \tag{3.43}$$

in which the fluence of threshold shall increase as $\tau_L^{1/2}$ increases as well.

As described, initially, the laser energy is described by the electrons and, hence, the electrons thermalize in an average time of 100 femtoseconds. Thus, the thermal equilibrium usually occurs after a multiple of the electron-phonon dispersion time. The electron-phonon dispersion time happens in the range of 0.5 to 50 picoseconds. Then, it leads to an important outcome: if the pulse duration is shorter than the electron-phonon dispersion time, then there is no heat transferred to the lattice. On the other hand, it is not observed in practice. When the lattice heats up, at a certain temperature, the evaporation begins and is able to be continued for many nanoseconds. Overall, even taking ultrashort pulses, such as the femtosecond ones, the thermal processes still remain active for a couple of nanoseconds, which leads to an almost independence of pulse duration for pulses shorter than 10 picoseconds [48].

In nanosecond pulsed laser regimes, because of the large durations of the pulses, there is enough time per pulse for thermal waves to propagate along the target material lattice and, in addition, create a quite large layer of melted material [32][33]. This melted layer is what makes micromachining experiments by nanosecond laser so imprecise due to all these undesired secondary effects.

5 MATERIALS AND METHODS

In this section, the experimental features and methods are presented.

5.1 OPTICAL SETUP

The optical setup was set to obtain the maximum quality of a nanosecond laser micromachining setup. Such optical setup consists of a Q-switch active Nd:YAG laser at 1064 nm with pulses of temporal duration of 1.2 ns and a repetition rate of 2 kHz ($M^2 < 1.1$, wedge HB-RPMC lasers). Figure 18 shows the full setup. In order to become the explanation clearer, the optical setup was divided into four sections.

Figure 18 - Schematic laser micromachining setup

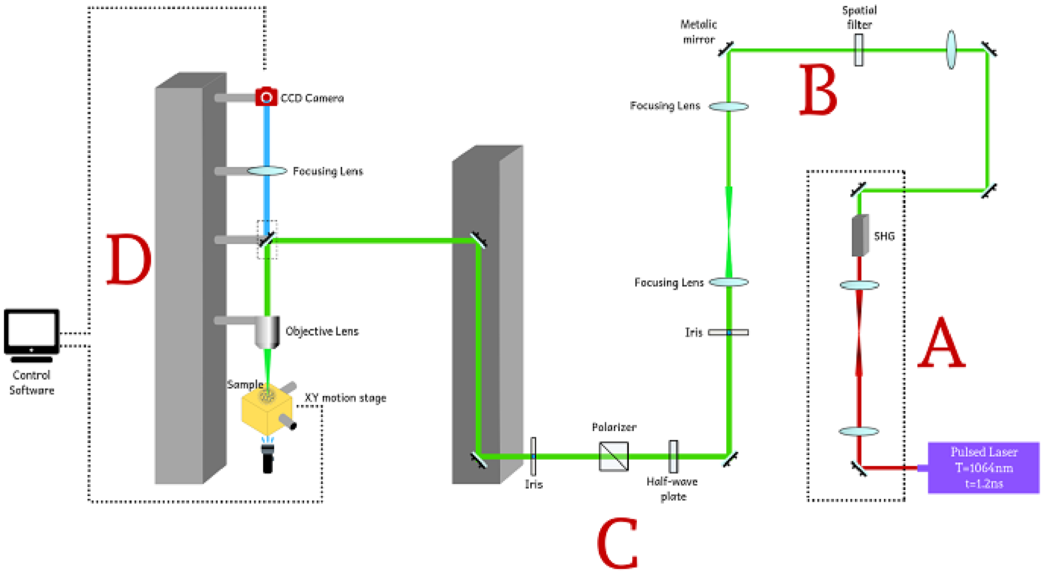

Source: Author.

For section A, the 1064 nm beam is directed through dielectric mirrors into a telescope to collimate the beam. After that, it is doubled using a LBO crystal cut for type-I second harmonic generation (4x4x20 mm). Then, the 532 nm beam passes through three dielectric mirrors (532 nm) to filter the fundamental laser beam. Then, it is focused on a spatial filter to obtain the TEM_{00} mode.

Figura 19 - Section A of the laser setup

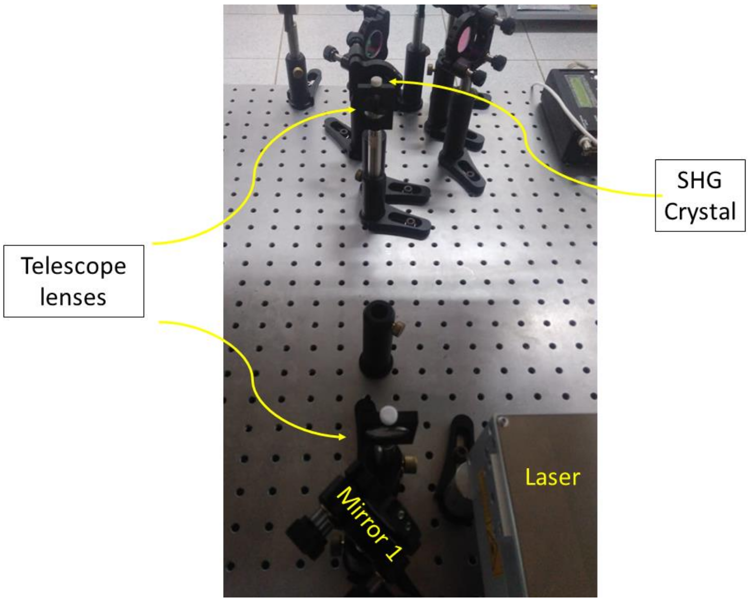

Source: Author.

For section B, a telescopic is used to collimate and enlarge the spot laser. Such procurement is important to cover the entire entrance of the microscope objective and, consequently, obtain the maximum peak intensity. Figure 20 shows the experimental setup for section B.

Figure 20 - Experimental setup for section B

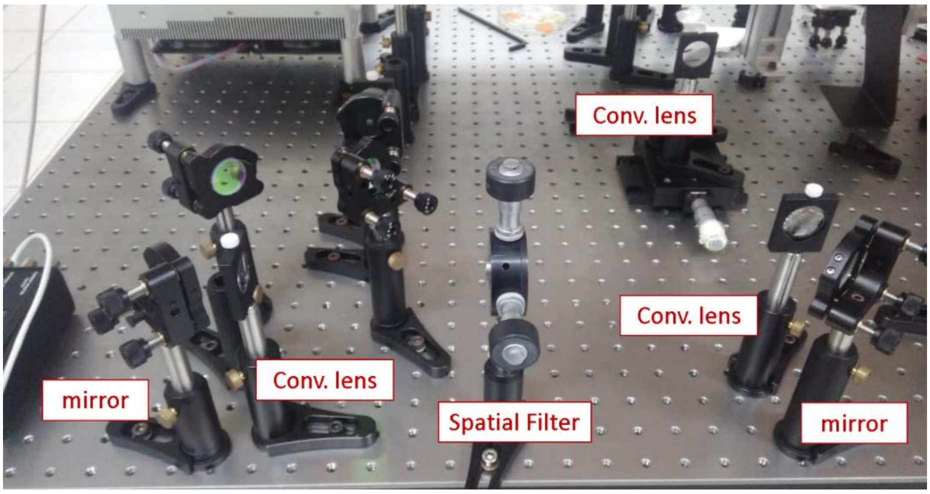

Source: Author.

Section C, in turn, starts with an iris located after in the back of the second lens of B-telescope. Its function, besides helping the alignment, also helps set the spot size to cover the microscope objective entrance as shown in Figure 21.

Figure 21 - Section C of the laser setup in detail

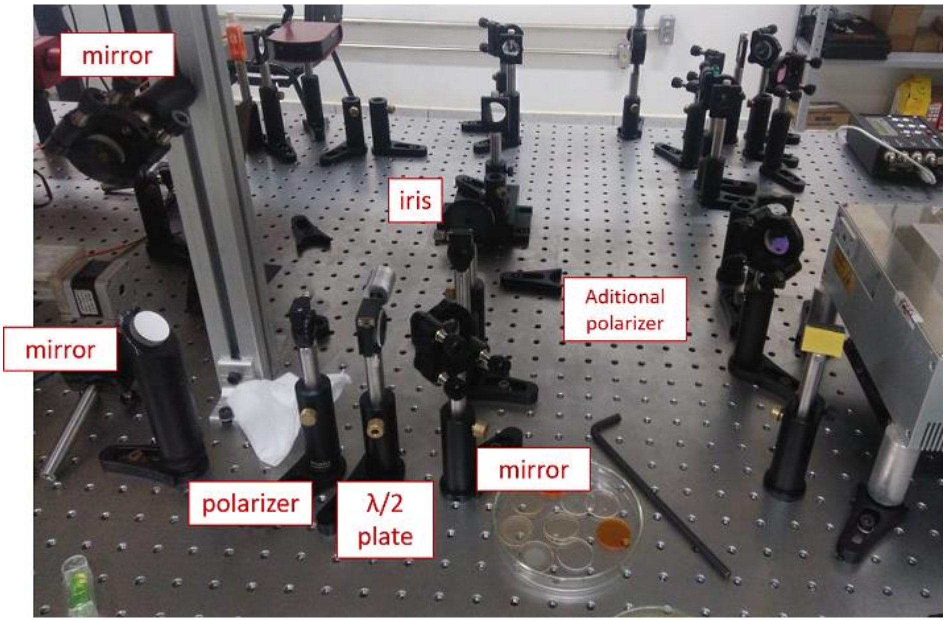

Source: Author.

In Section C, the 532 nm beam passes through an iris to filter the spatial noise, and it is directed to a half-wave plate and a calcite polarizer to control incident power in the sample without changing the polarization. At the end of section C, there is a mirror allocated over a 45º vertical angle support that sends the beam to a 45º angle aluminum mirror located at the first tower, which to send the beam to the next tower (section D).

Section D shows the laser beam reaching a dielectric mirror in which the beam goes straight down and finally targets the microscope objective. The dielectric mirror allows the passage of white light and, at the same time, it works to block the green color of the laser beam and. This feature is necessary because a white-light LED system illuminates the sample to project their image in the CCD camera located at the tower top.

Figure 22 shows the described tower of equipment. Further, the importance of blocking the green wavelength is needed because the system is illuminated from below to above until the CCD camera can capture high-quality images in real-time.

Figure 22 - Tower of section D

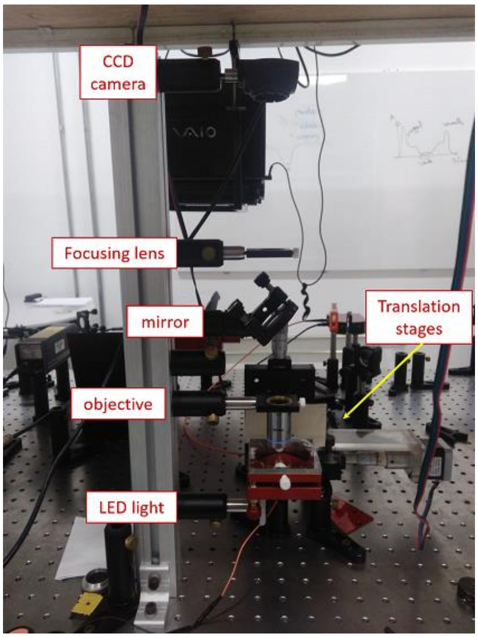

Source: Author.

Thus, if it is used as a metallic mirror, the light would be blocked we the system would be “blind”. Also, there is a last focusing lens, which function is coupling to both images. To illustrate that, think about the path, both lights – laser beam and white LED – across. The laser beam comes over the mirror and is reflected down until the sample.

On the other hand, the LED light crosses the sample, and the light enters the microscope objective and next across the dielectric mirror. Due to these different ways, light across two different paths that leads to a non-common focal point. The converging lens so comes up to couple these two paths, and so CCD camera now can capture the whole situation. To put it another way, on the CCD software, the screen shows the surface of the sample and the laser spot too.

Finally, to finish the experimental setup, a software created by our advisor Prof. Dr. Marcelo G. Vivas controls the translational stages in which we are able to control the speed of translation and the number of microstructures that are machined in the sample. The brightest point in Figure 23 is a sample being micromachined.

Figure 23 - Full experimental setup working in 80% power of the laser

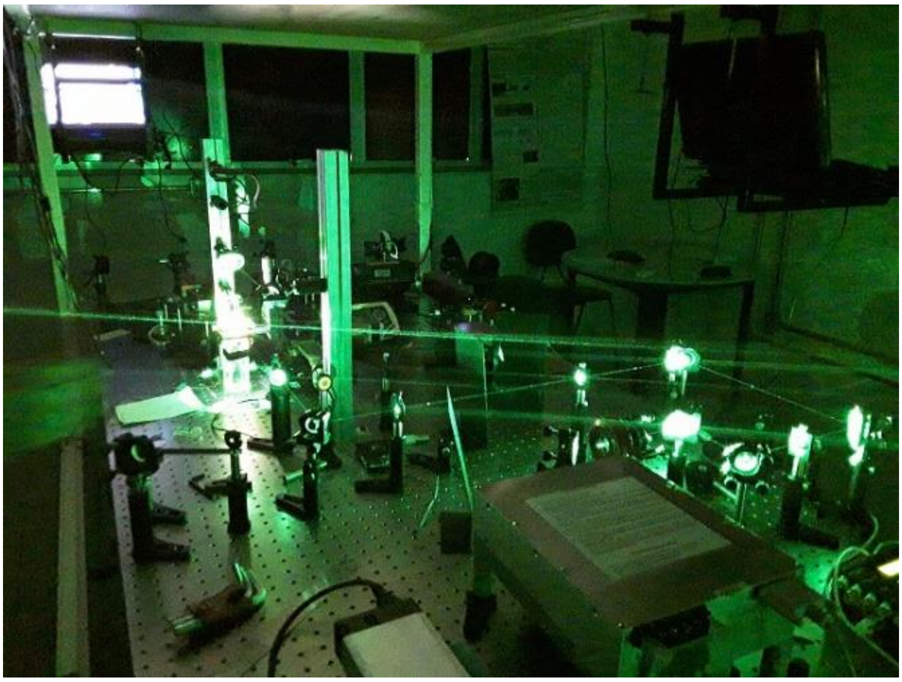

Source: Author.

Another detail to comment, if you look carefully at Figure 18, we might see some differences with the setup showed in Figure 23. This green photo shows the previous setup that worked but not as good as the one explained. In this picture, for example, there is just one telescope to enlarge the spot size. But running tests, we realized the need to add another telescope right before the SHG crystal. By doing that and changing the position of the polarizer, we got more control in the final power, as said before.

In micromachining experiments, it is common to use a moving translational base where the specimen is placed. This basis, when switched on and translating, allows the specimen to be micromachined forming different line patterns on its surface. Figure 24 presents a schematic representation of a XYZ-axis translation speed where the sample is located. Furthermore, the XY- axis moves the basis horizontally as well as the Z-axis controls the focus over the sample as it goes up and down, moving the beam focus up and down within the sample, and it was controlled manually. There are also two stepper-motors connected to XY-axis, and it was controlled by a homemade software designed at LEOF. From Figure 24, we can infer that when this basis is appropriately connected in an electronic circuit, the XYZ-basis may produce any image over the specimen.

Figure 24 - Schematic representation of an XYZ-axis translational base

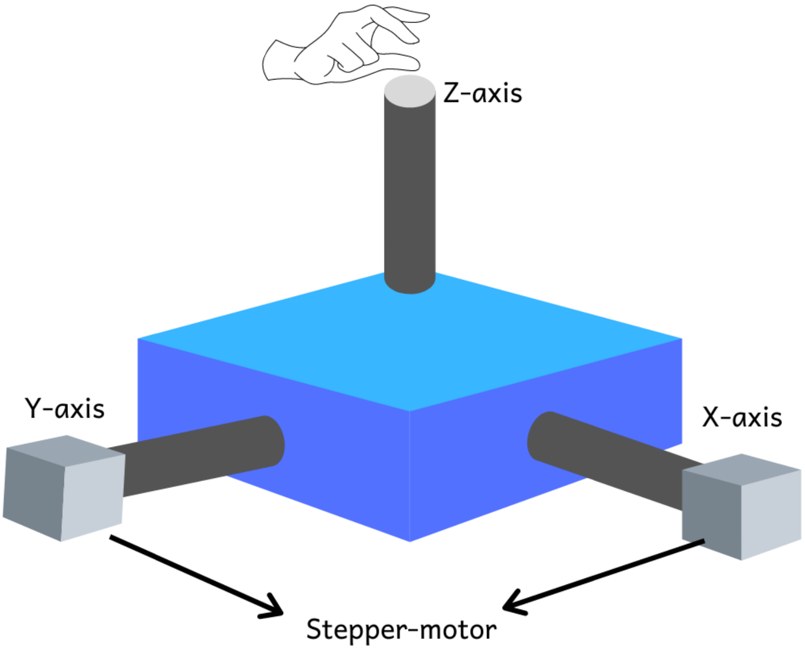

Source: Author.

I point out, for this section, however, that there was a huge improvement in the setup, including the controlling software, in which we got a higher resolution on its movement. Basically, we obtained an improvement in the spatial resolution of the stepper motor from the approximately 3.3 μm/step to 0.6 μm/step. However, such an increase of resolution generates a reduction in the translation speed from 470 μm/s to 200 μm/s. Moreover, new experimental modifications were performed in the optical setup. To summarise these changes, we take, at first, the telescope located right before the SHG crystal. The addition of this telescope enlarged the spot size by two times and provided better collimation of the laser beam. As a result, the larger beam covered a larger area of the crystal, promoting a greater SHG conversion. Another improvement was the inclusion of a translation stage in the second telescope – located in section C as appointed earlier – to avoid divergences on the beam at long distances. Thus, we reduced the loss of energy across the path. Finally, yet important, as mentioned, the new resolution of the system allowed a translation speed in a range between 10 μm/s and 200 μm/s.

5.2 ELECTRONIC SETUP

This section presents the electronic configurations employed in our experiment to provide better functioning and automatization over the optomechanic devices, especially the XY-stage, wherein the sample is micromachined.

5.2.1 Introduction

The rise of the electronic features employed in Physics has offered many important achievements, whereas using mechanical sets we could not get nor even do depending on the experimental purpose. Thus, in our experiment, we also made use of this tech to improve the functioning of the system. The current employment of electromechanical components and setups is essential to keep a modern and updated lab of modern physics out of high prices for such technologies [49]. Thus, it is possible to acquire important data using low-price setups.

In optics and photonics experiments, the usage of electromechanical components like stepper motors and the optical shutter is very important to provide better data acquisition and, nonetheless, better functioning of the system itself due to its more precise control over the system [50]. The stepper motors offer precise control of movement features such as angles, speeds, and changing directions. The optical shutters, on the other hand, help to close and allowing the laser incidence on the sample while being micromachined.

5.2.2 The Electronic Setup

Our electronic setup was built and configured with low-price materials and a computer program created using dedicated software. As said briefly before, stepper motors and optical shutters might be very interested in being used in physics experiments. Here, these two electromechanical components were put together with an Arduino Uno, two Easy Driver boards, and a relay.

Figure 25 shows the schematic of our electronic setup with its components and the schematic wires to link and connect the parts.

Figure 25 - Shows the schematic construction of the electronic setup for our experiment

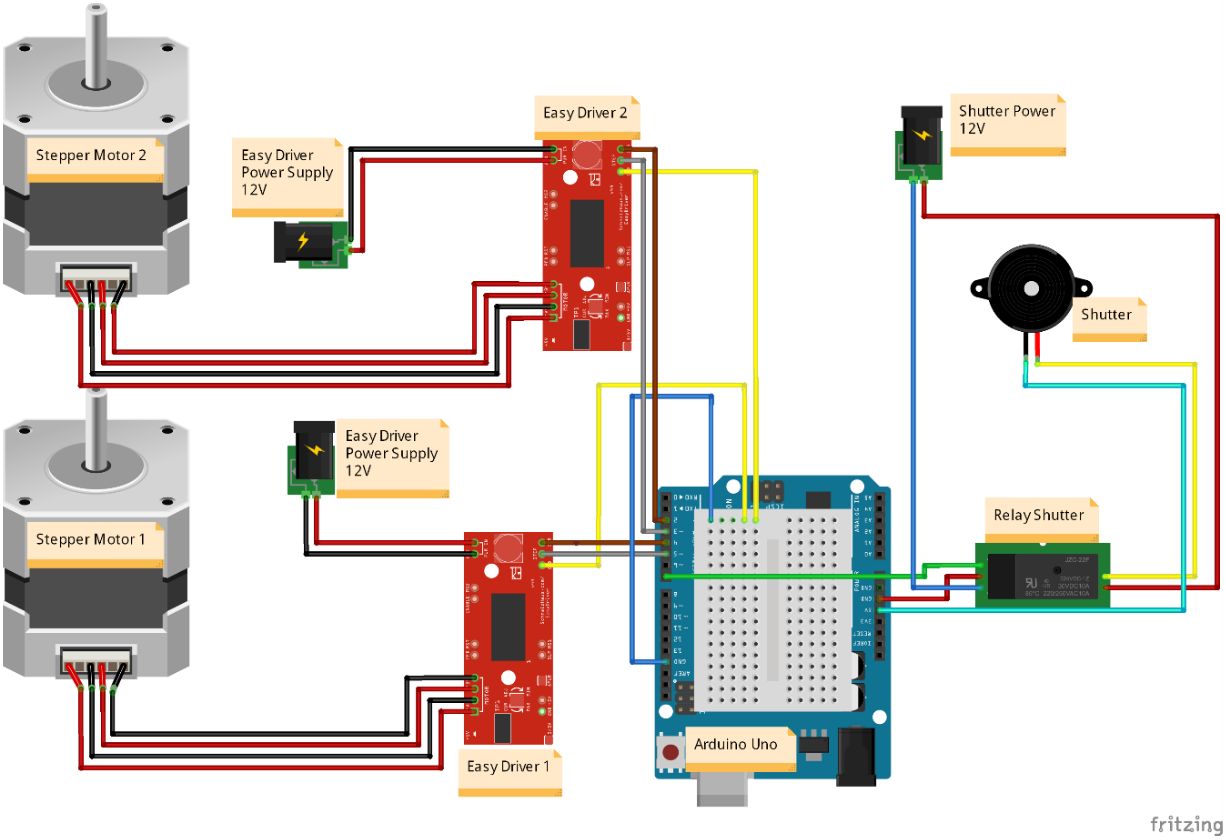

Source: Author.

As can be seen, all the connections and clearly understand the constructions of this setup. The Arduino Uno board has been widely used in physics experiments because it offers easy employment [51]. There are two Easy Driver components are connected in the pins of the Arduino. The Easy Driver boards, otherwise, control the two stepper motors. Here, the speed of the motors is controlled by the step of each motor. Thus, the Easy Drivers read the entrance information coming from the Arduino program and convert it into a number of steps that will be given by the motor. The number of steps in a time interval results in the speed of translation. In addition, there is three power supply in the setup – 12V for each one – in which two of them are for each Easy Driver component, and the other one supplies the relay and the optical shutter.

The optical shutter, in short words, works as switching on/off in terms of the laser incidence. It means, in other words, that the laser incidence over the sample can be allowed or blocked depending on the design desired for the experiment. For instance, if we work out some rectangular drawings in sequence, from one object to the next, the laser has to be blocked to do not damage or to cause no modifications while the sample is translating until the starting point of the new object. To illustrate such situation, a schematic is represented in Figure 26.

Figure 26 - Shutter

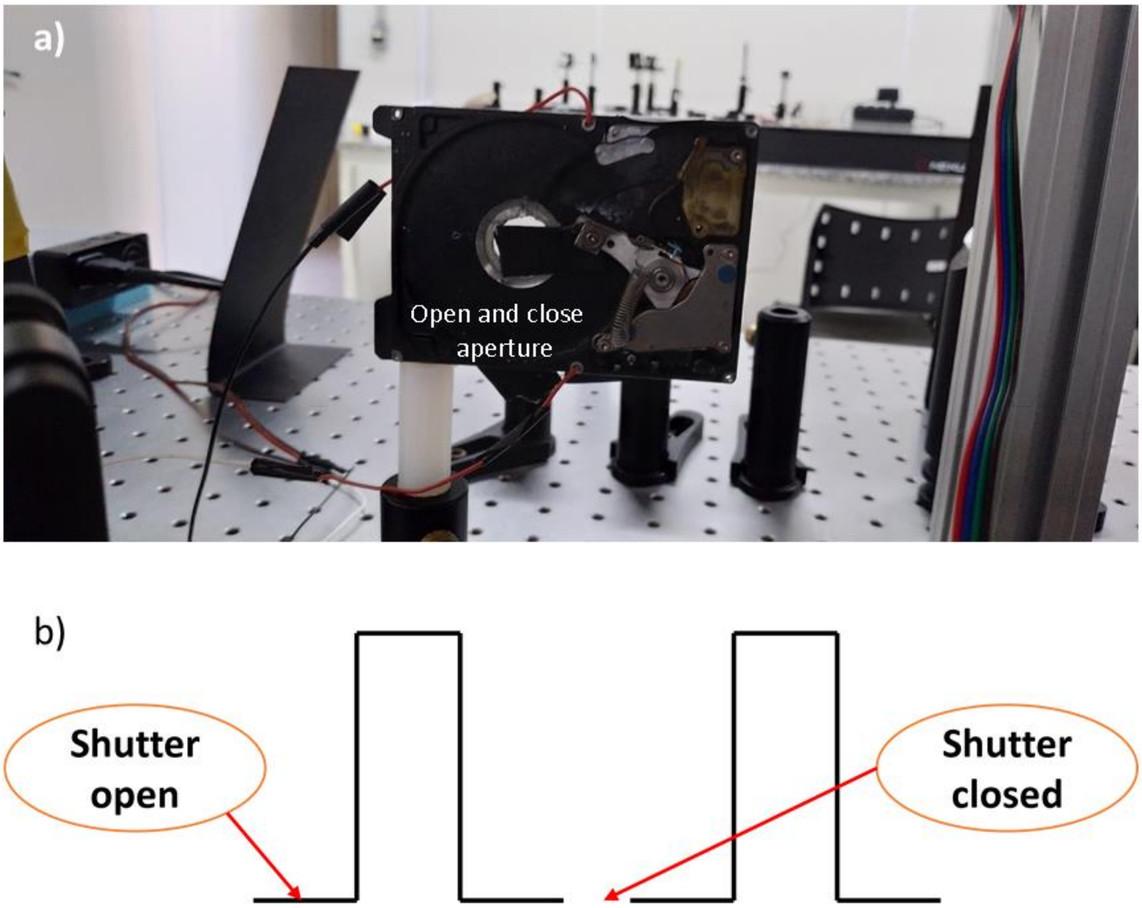

Source: Author.

Caption: a) picture from the shutter apparatus placed in the experiment. b) Representation of the shutter switching on/off effect in a rectangular micromachining experiment.

When the shutter is open, the laser beam flows throughout the setup and reach its final target – the sample. However, when the shutter is closed, the laser beam is blocked yet on the early sections in the setup.

The stepper motor is an electro-mechanical component that converts the pulsed digital signal into motion. These stepper motors allow us to control the speed, direction, and acceleration with high precision [52]. Currently, this tech can subdivide the steps of the engines into micro-steps, which helps to provide better acquisition and accuracy on the data.

Further, the Easy Driver is a component able to easily control a stepper motor, and it is compatible with any component with a digital pulse exit from 0 to 5V. It links the Arduino to the stepper motors, and its connections are explained next in Figure 27. Once the system is on, the easy driver works as the link from the commands that comes from the Arduino and the stepper motor itself. As illustrated in Figure 27, the top right connections link the Arduino to the Easy Driver. The top left connections to receive the energy of 12V from the power supply and the bottom left ones to connect the bipolar stepper motor within its coils.

Figure 27 - Easy Driver connections and pins

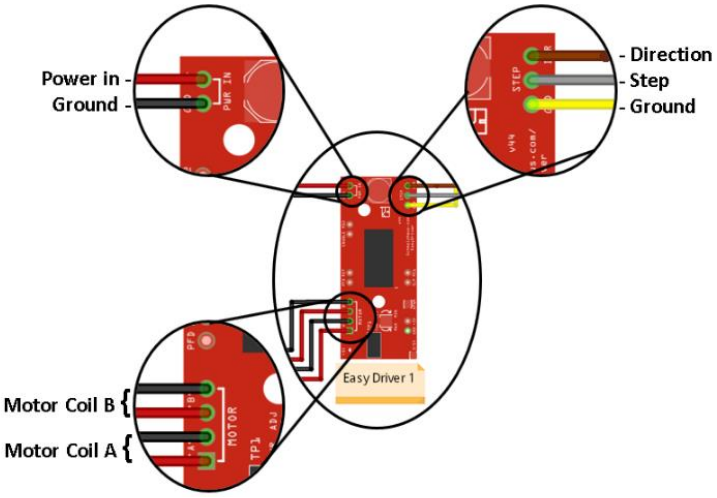

Souce: Author.

Figure 28 shows a picture taken from the lab, where it is shown the real electronic setup. It illustrates some features not showed in the schematic representation, such as the grey aluminum block coupled with the Easy Drivers. Here, for short, we explain that this was necessary to help to control the temperature of the Easy Drivers. As with any other electronic equipment, it heats up when working for a long time. As a result, we have coupled this aluminum block filled with a thermal paste, similar to those used in laptop’s processors. The paste works diffusing the heat over the aluminum, so it does not heat up that much, which could damage the component and compromise the experiment. Further, the shutter circuit is composed of a relay, a power supply, and the shutter. Here, the power supply provides an input voltage of 12V to the system, whereas the relay works as switching on/off, which corresponds to the opening and closing motion, respectively, of the shutter. In this context, when the features of the micromachining experiment are set in the program, the relay reads this information and turns the shutter on or off. In addition, there was a need to insert a diode linked on the relay and shutter connections due to a residual electric current that was being received by the stepper-motors as feedback from the relay.

Figure 28 - Shows the real electronic circuit in a photo taken in the lab

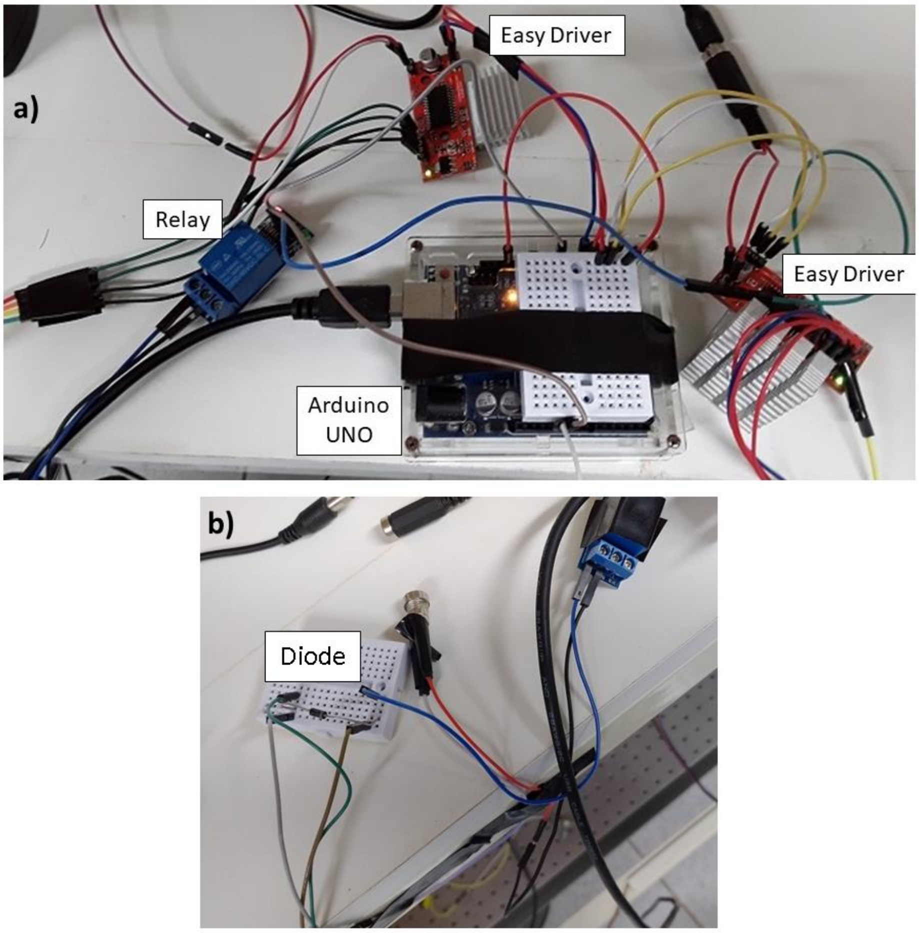

Souce: Author.

It is important to say that the drive control of the engine was also designed within Arduino programming. As a result, we have made the circuit as simple as possible, with no need for additional components like a general controller containing all the logic of Tables and calculations for the motors or other part of the experiment. With no additional components, it leads to a lower price, and it reduces costs.

Overall, this very simple electronic circuit is able to highly enhance the optical micromachining setup in which the use of these tools differs from very complex electronic systems while are still able to provide precise control and performance to the experiment. To put it another way, we have attested and agreed with other authors and researchers, along with the laboratory trials, that it has been proved to be very powerful equipment for physics experiments.

6 RESULTS AND DISCUSSION

In this chapter, we shall discuss and present our results for the micromachining tests that were run in our laboratory.

Firstly, we made tests in gold and chitosan samples to calibrate the optical setup. These were just calibration tests wherein the collected data showed the right path to improve the experiment. Besides, the chitosan and gold samples tests showed two main critical points to be improved in the setup. The first one was the collimation and enlargement of the spot size, while the second one was the alignment of the laser path. These results presented some strange and not expected graph curves, which had indicated some issues in the setup. For further information, see Appendix A and B.

As introduced, the presented data for Gold and Chitosan served well its purpose of giving good directions to improve the optical setup. However, the optical setup, for gold and chitosan tests, was being tested and improved according the outcoming data.

It is important to emphasize that we expected such an increase in the line width is responding to an increase of the pulse energy. On the other hand, as the translation speed increases, the average width shall decrease because of the repetition rate of the laser beam, which remains constant during the process. For that reason, the expected behavior showed in the graphs should point to a saturation region in which the width of the line does not increase anymore.

Further, in this chapter, the first section presents the PMMA/azo-chromophore results, which are considered the first experimental result of our setup. Sequentially, the second section presents the results obtained for the tests in Perovskite quantum dots thin films.

6.1 MICROMACHINING IN PMMA/AZO-CHROMOPHORE

In this section, the data and results from experiments in PMMA+Azo are presented.

6.1.1 Introduction

Polymer-based materials have been widely used in physics experiments due to its variety of possible applications. In recent decades, the interest in developing polymer-based materials and optical technologies has increased because their advantages over glass, such the easiness on processing, low cost of production and fabrication. Moreover, such materials are usually engineered to present specific and important properties such as, for instance, electro-optic coefficient and nonlinear optical response [53].

In particular, the production of optical components has been based on poly (methyl methacrylate)(PMMA) due to its high transmission in the visible and near-infrared, and the similarity of its refractive index to that of standard optical fibers, which favors coupling to existing fiber technologies [54].

Besides PMMA, another interesting material is the azo-aromatic compounds. In short words, these materials present a double bond among two nitrogen atoms, which are bound to aromatic rings. These azo dyes have been largely used by textile, food, and paper industries because of their variety of useful applications and properties for optical purposes [55]–[57]. Also, azo-compounds have been studied in 3D optical storage because of their capability to induce optical birefringence due to the trans-cis-trans photoisomerization process. However, it needs a host matrix to hold the chromophore. In our experiment, PMMA was used as the host matrix for the azo compounds due to its low cost, easy handle, chemically stable, and other important features to be used as thin films for micromachining reasons [58].

In our experiment, we have used the PMMA doped with bi-azocompound to make the thin films used in the micromachining sets.

6.1.2 Materials and Methods

PMMA films doped with azo-aromatic compounds were also produced via the casting technique. These azo films were kindly prepared by the Msc. Lidiana Maranesi Silva – she is also a researcher at LEO&F. The PMMA/azo-chromophores films present an orange color. This Azo compound is named **YB3p91** [58]. Figure 29 shows the molecular structure for the **YB3p91**.

Figure 29 - Azo-compound molecular structure

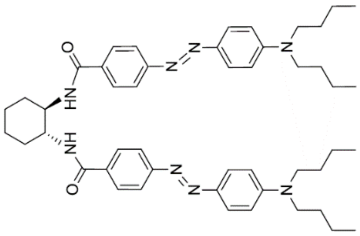

Source: [58].

To micromachine the PMMA sample, we used three different microscope objectives are those microscope objectives of 10x, 20x, and 40x. The features of each objective microscope lens and the screen size are gathered in Table 4. The horizontal and vertical screen sizes were measured by the author using a micrometer as a reference. As we will see further in this section, the average width of the machined lines decreases by half factor from one microscope objective to another. It happens because of the Numerical Aperture of each lens.

Table 4: Characteristics of each objective microscope lens and the screen size.

Objective	**Numerical Aperture (NA)**	**Working Distance (mm)**	**Horizontal Screen Size (µm)**	**Vertical Screen Size (µm)**
10x	0.30	16.00	560	480
20x	0.50	2.10	280	240
40x	0.75	0.72	140	120

Source: Author.

The Numerical Aperture of an objective microscope lens expresses the ability of the lens to gather the light and resolve fine sample details, as explained in chapter 3, section 3.4.1. As a result of increasing the NA, when a laser beam is focused throughout a microscope objective, the focal volume of the spot decreases, producing then, smaller lines. For example, the 20x lens produces lines with half average width in relation to those produced by the 10x. As a consequence, the screen size captured by the CCD camera also decreases, as it is shown in Table 1. To illustrate the screen size difference, it is required to change the distance traveled in each test; otherwise, we would not be able to see the entire machined lines on the screen. For this reason, we decreased the distance traveled by the translation stages. Figure 30 shows the machined area for each microscope objective.

Figure 30 - Picture of the machined area at naked eye photo

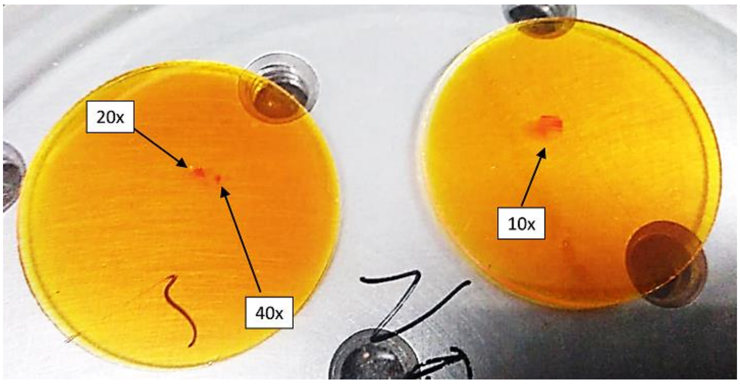

Source: Author.

Therefore, as can be seen from it, the 10x microscope objective produced a larger machined area while the 40x one has a smaller area. The x and y distances traveled by the stages are also shown in Table 5.

Table 5: Distance traveled by the x and y stages.

Microscope objective	**x-distance (µm)**	**y-distance (µm)**
10x	500	100
20x	150	25
40x	80	15

Source: Author

6.1.3 Results and Discussion

The ground-state absorption spectrum for the V-shaped azo-chromophores/PMMA in solution (solid line) and film (dashed line) is shown in Fig. 31 (a). As noted, for both solution and film forms, the azo-chromophore presents a wide absorption band located at 448 nm. If we look carefully at the next graph, it can be seen that there is still an absorbance at 532 nm (laser wavelength). Therefore, here we have a resonating process (one-photon absorption). Details about the electronic and optical features for this molecule can be found in Ref. 27.

Figure 31 - Absorption spectrum for V-shaped azo-chromophores/PMMA in solution (solid line) and guest-host film (dash line)

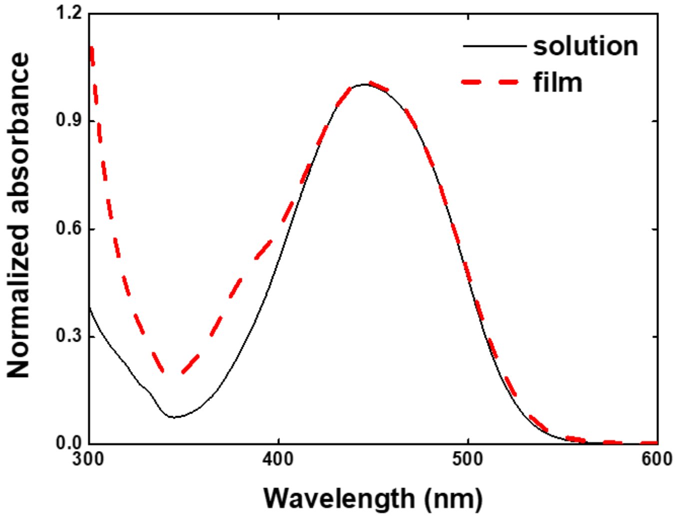

Source: Author.

In solid-state, the V-shaped azo-chromophore exhibits a shoulder at 380 nm as compared to the solution. Such a shoulder indicates that in the solid-state, there are a considerable number of chromophores in the *cis* configuration.

Micromachining in PMMA with aromatic azo compounds presented a clear overview of the experiment, in which it behaved as well as expected in accordance with the theoretical basis. These tests for PMMA/azo-chromophores were taken over different microscope objective lenses, translation speeds, excitation wavelength (532 nm), and pulse energies according to a set of measurements proposed by the author and his advisor.

Before we started micromachining the samples, we had to find the first energy that causes visual modification on the surface. It is called threshold energy, and it has been evaluated by the graph data, further explained in this chapter.

Figure 32 illustrates the micromachining pictures taken for PMMA+azo film over different pulse energies – from 45 nJ to 750 nJ – and translation speeds were set in 10, 25, 50, 75, and 100 µm/s by using a 10x microscope objective and excitation wavelength of 532 nm. The PMMA/azo-chromophores films have absorption at 532 nm and, therefore, the microstructures reported here are an outcome of the linear interaction between the laser beam and the material. Repetition rate was set constant at 2 kHz.

Figure 32 - Ablation area around the burned line in comparison with superficial change

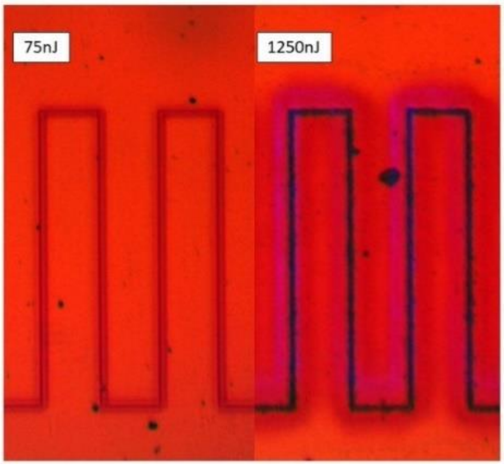

Source: Author.

Besides founding the energy of threshold, we started a structural modification in the sample rather than ablating it. Thus, we used a range of eight different laser power output from 90 μW to 2500 μW, which implies pulse energies from 45 nJ to 1250 nJ. It is essential to mention that in Figure 33, we put only the first five pulse energies to give a better sight over the images.

Figure 33 shows the visual difference on the machined lines for 75 nJ and 1250 nJ, for instance. As can be seen in Figure 33, on the left side of the picture, there is no dark red area around the modified line, which indicates superficial changes because the line is steady and shows only a different color, which indicates changes in the refractive index only. On the other hand, the higher pulse energy, on the right side, with de 1250 nJ energy, produced a large dark red area around the path traveled by the laser spot. All this area means ablation with a burned central line, and it produces a heatwave that propagates and continues the process of heat transmission along the adjacent regions.

To analyze the effect of the pulse energy on the resolution and width of the microstructures, in Graph 1 we show the average width as a function of the pulse energy. As noted, the average width for lower speeds was higher than those for faster speeds, as expected.

Figure 33 - Sequence of micromachining in PMMA/Azo films with a 10x microscope objective

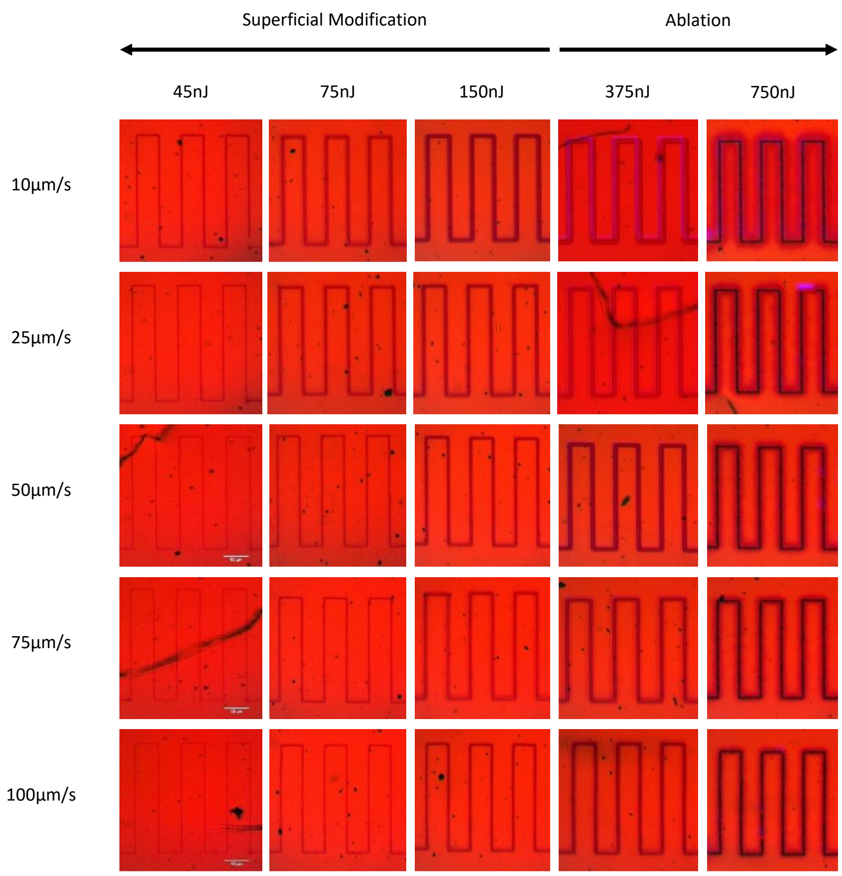

Source: Author.

The black line, for instance, showed wider microstructures as a result of its very slow speed. On the other hand, green and cyan lines, which are the two fastest speeds, showed narrower microstructures due to the less interaction of the laser with the sample. It is important to remember that the repetition rate (2000 Hz) was kept constant during the process.

On the initial energies, for all the colors, there was a significant rise in the width of the line from the first energy until about 400 nJ. After this point at 400 nJ, for the blue, red, and black lines, respectively, there was a steady upward, which tends to a saturation region over the further points.

After 400 nJ of pulse energy, the material suffered complete ablation. As a result, there was a burned central line in which the spot reached the sample with high intensities. At the same time, as shown in Graph 1, the average width tends to be constant after 400 nJ, corroborating the ablation process. It is important to emphasize that this data was constructed considering all the dark red areas.

Graph 1 - Average width as a function of energy per pulse for a 10x microscope objective

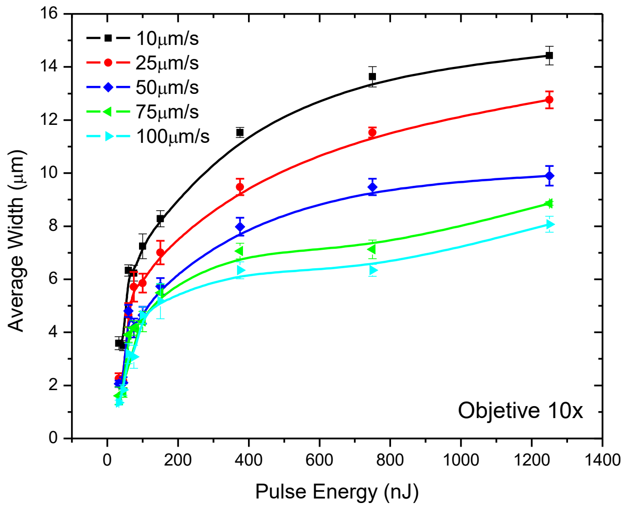

Source: Author.

As the width shall increase by increasing the energy, an opposite situation happens when the energy remains constant, and we increase the speed of translation. To illustrate this situation, Graph 2 presents an overview of changing speeds. As can be seen, each line has the same energy per pulse, and distinct speeds were set for each test. As expected, the average width decreased as a function of the increase in translation speed. For example, lines microstructured with width as small as 1.6 μm were obtained, showing the improvement of resolution of our experimental setup.

Graph 2 - Average width as a function of translation speeds for a 10x microscope objective

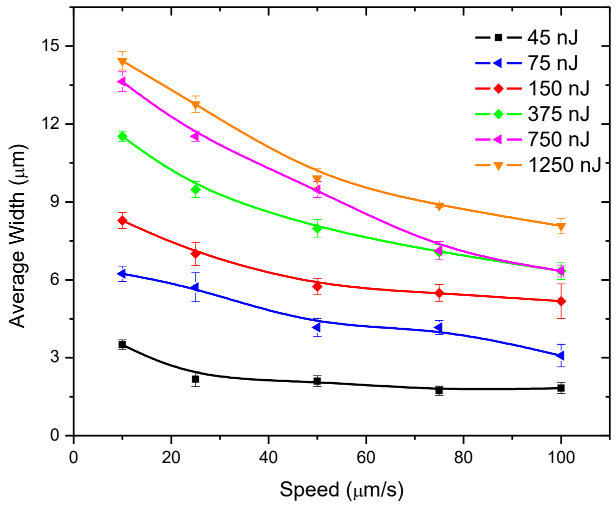

Source: Author.

Further, we changed the microscope objective from 10x to 20x, and, following the same reasoning and patterns of energies and speeds, more tests were run to compare the results of different objectives. Similar results can be observed in Figure 34 as comparing it with the ones reported for the 10x objective in Figure 33.

Figure 34 - Sequence of micromachining in PMMA/azo films with a 20x microscope objective

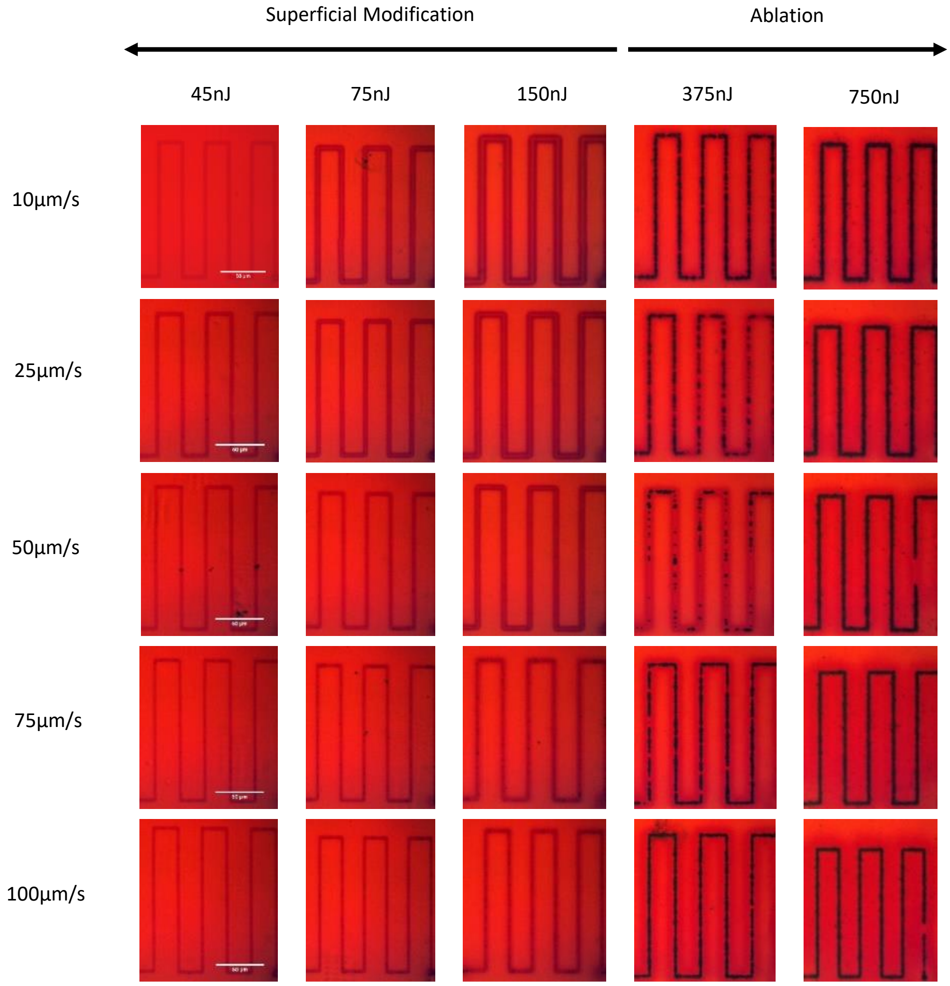

Source: Author.

However, a smaller linewidth and a decrease of the pulse energy to achieve the ablation region was observed. Such outcomes can be explained because the 20x microscope objective has a smaller waist size (w_0) and, therefore, it tends to increase the peak irradiance (I) according to equations 3.31.

Graph 3 presents data comparing the average width as function of pulse energy for a 20x objective lens. As can be seen from the graph, as the speed increased, there was a decrease in the width of the lines. The highest speed (100 μm/s) in the pink line, showed the smallest values of linewidth. Thus, from the initial energies until about the

300 nJ there was a sharp rise in the widths. The black line, for instance, presented the highest slope in the curve, whereas the blue and green lines presented a steadier increase compared to the black one.

Graph 3 - Average width for a 20x microscope objective related to energy

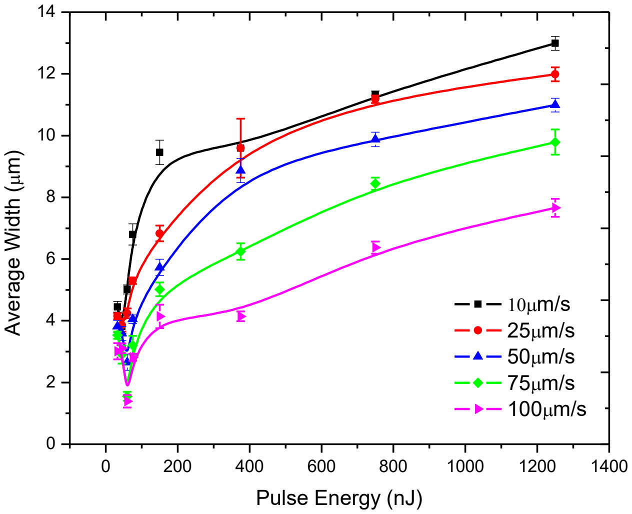

Source: Author.

As can be seen from the graph, there was a dramatic drop from the first to the second point in the curves. Such behaviour was not completely understood.

To illustrate the ablation area compared to surface changes, the pictures below show lines machined in (a) with 60 nJ and (b) 750 nJ. In part (b), as can be seen, there is the dark red area around the burned central line. Both pictures were taken for the same speed (50 µm/s). Here, using the 20x objective allowed the system to achieve widths smaller than 2 µm, which were considered as very good results.

As is shown in Figure 35, on the left side, it is presented a modified line for small pulse energy. In contrast, on the right side, we can see the central burned line caused by the higher energy and peak irradiance surrounded by a tiny dark red area. The a-side shows the structural change in the refractive index while the b-side shows the ablation characteristic.

Figure 35 - Superficial change and ablation area at the same speed

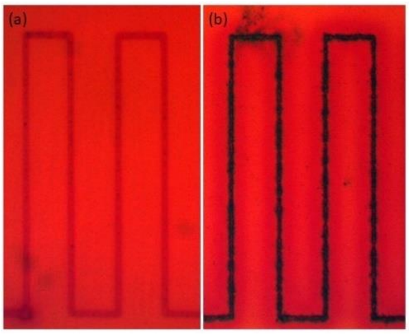

Source: Author.

Following the same reasoning presented before, Graph 4 indicates the average width as a function of translation speed for the 20x microscope objective. As can be noted from the graph, the average width decreases as compared to the increase in translation speed for different pulse energies.

Graph 4 - Average width as a function of translation speeds for a 20x microscope objective

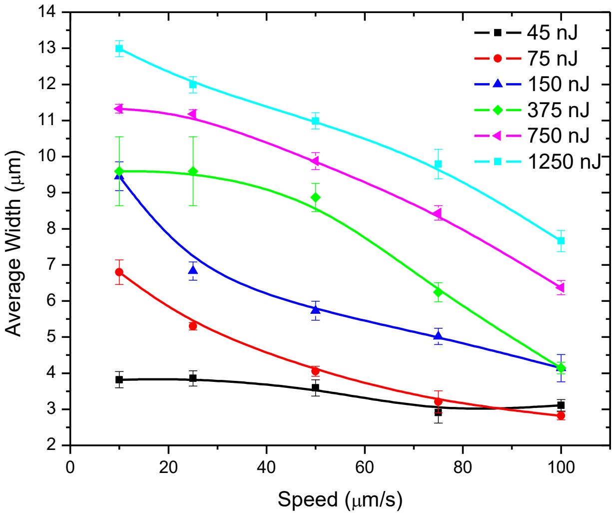

Source: Author.

Therefore, it is clear from the outcomes that the speed has a significant influence on the way the sample responds to energy. As expected, lower speeds tend to wider lines. The smallest energy, represented by the black curve, resulted in the narrowest modified lines. Furthermore, the magenta and the cyan curves, respectively, presented the widest modified lines. Interestingly, the first and the last dot in the blue curve coincides with the same dots in the green curve. It was probably because of some specific features that did not work as expected.

Furthermore, Figure 36 shows a picture comparison in which we can see it as an example of the data described in Graph 3 and 4. Here, the pictures were taken for a speed of 25 μm/s. In this situation, for the speed of 25 μm/s, Figure 36 shows the increase in the width for five different energies, which are 45 nJ, 75 nJ, 150 nJ, 375 nJ, and 750 nJ.

There is a white scale bar on the bottom left side that helps to compare the average width. Still, for 375 nJ, we are able to see that the black line does not represent the full width. The granulated aspect of the lines occurs because of the relation between speed and energy. Looking carefully, we can see that the dark red area around the central line. Thus, the full groove is meant to do be all the dark red areas. Finally, in the last picture, we cannot see a clear separation among the lines. However, we still may infer that it contains the widest lines.

Figure 36 - Increase of width due to the raise of the energy for a 20x objective microscope

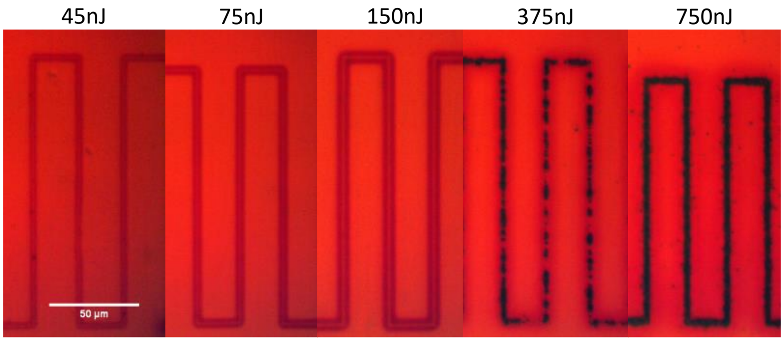

Source: Author.

Further, Figure 37 introduces the results obtained for the 40x microscope objective. As illustrated, those lines machined by the 40x microscope objective are smaller than those machined with the other lenses. As explained before, the 40x microscope objective allows the fabrication of narrower lines because of its smaller numerical aperture.

Figure 37 - Sequence of micromachining in PMMA/Azo films with a 40x microscope objective

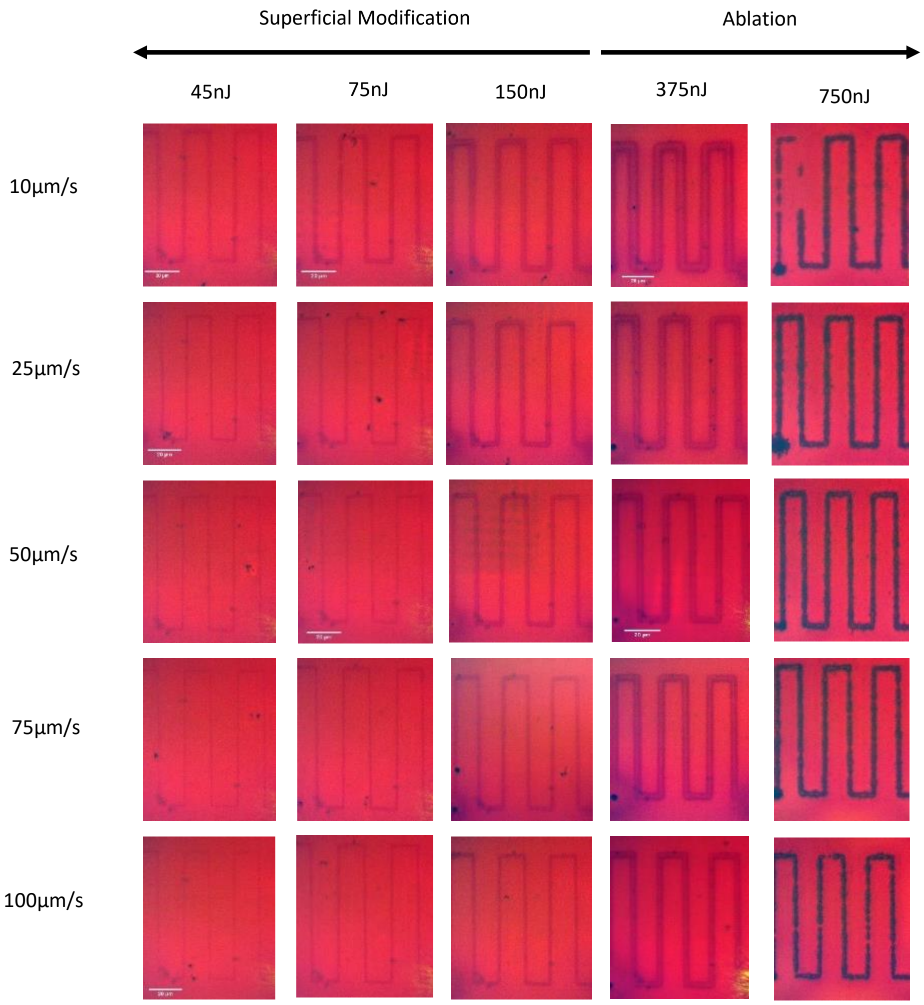

Source: Author.

Graph 5 shows the average width for those structures machined with the 40x microscope objective. At the speed of 10 µm/s, the average linewidth is much wider than lines machined under higher speeds, which is consistent with all the previous results obtained so far. We shall point out that for speeds of 50µm/s and 75µm/s, the lines presented a very significant similarity in its width.

Here, we have achieved a minimum width as small as 1 µm, which is small enough to be further studied for many possible industrial applications. Thus, we see that this trial has behaved as expected. Further, let us check the comparison between the average linewidth in which the pulse energy was kept constant, and the speeds were being changed. Graph 6 illustrates some interesting outcomes. The first one, it is clear from the graph that lines machined with the same speed of 10µm/s for energies of 45 nJ, 60 nJ and 75 nJ, black, blue, and red lines, respectively, did not show much difference in its measurement.

Graph 5 - Average width from the microscope objective of 40x

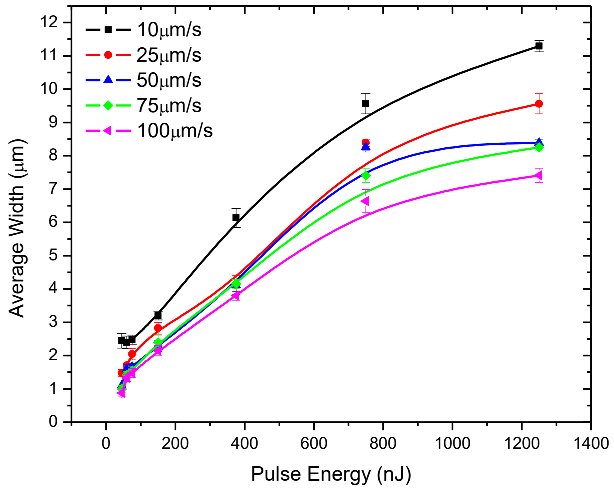

Source: Author.

However, even presenting the same width at the first point, the curves are still as it was expected. The wider lines were obtained for 750 nJ and 1250 nJ energy per pulse, respectively. Finally, all curves presented a similar aspect, in which the curves reduce in values as well as the speed of translation increases.

Graph 6 - Average width related to the speed. From the microscope objective of 40x

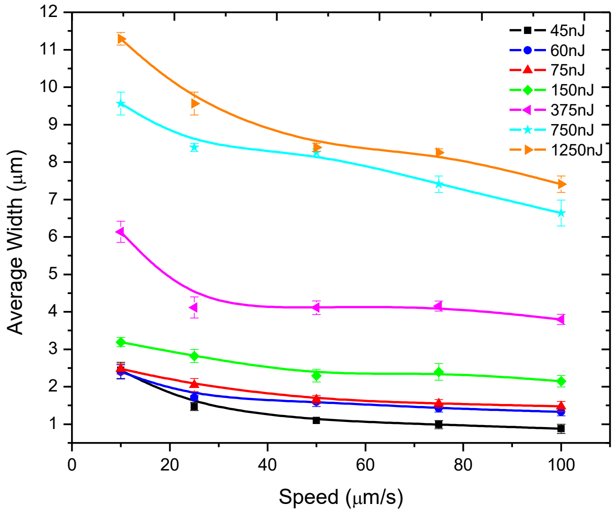

Source: Author.

To simplify the comparison between those databases, Graph 7 presents only the results for the speed of 10 µm/s and 50 µm/s.

Graph 7 - Comparison between the average width data from 10x, 20x, and 40x microscope objectives over the speeds of 10 µm/s and 50 µm/s, respectively.

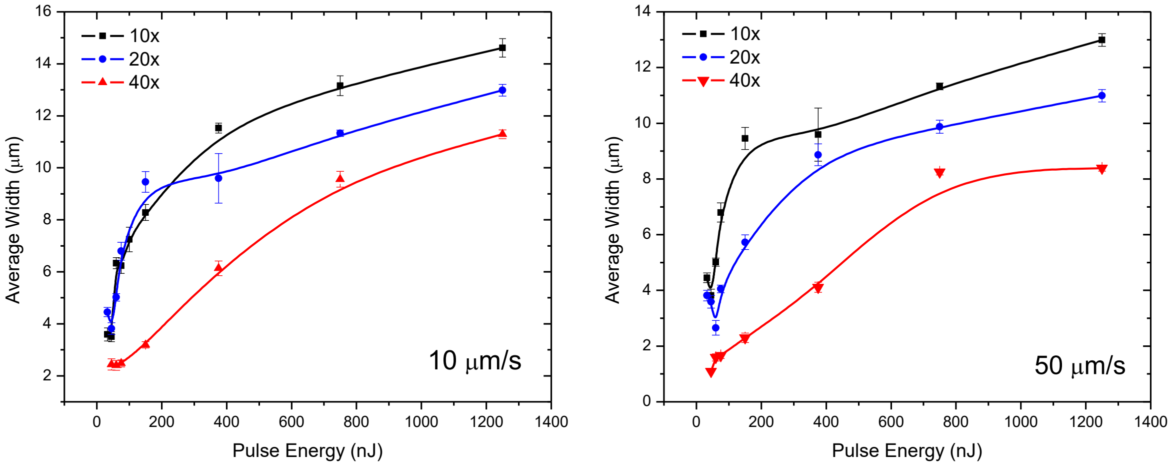

Source: Author.

Two aspects can be clearly observed in Graph 7. The first one, microstructures with linewidth as smaller as 0.9 µm, was obtained. The second one, an increase in spatial resolution as we used the 40x microscope objective even in a resonant process (linear absorption).

6.2 MICROMACHINING IN $CsPbBr_3$ QUANTUM DOTS THIN FILMS

In this section, the data and results from experiments in Perovskite Quantum Dots are presented.

6.2.1 Introduction

Perovskite Quantum Dots (QDs) are colloidal photoluminescent semiconductor nanocrystals, and it has been widely used and researched in the field of fundamentals materials research to supply the interests in industrial needs and also in photonics applications [51][52]. In particular, perovskite QDs are interesting materials to produce useful electrical energy from solar energy. QDs present unique optical properties such as narrow emission, bright photoluminescence, size-dependent absorption and emission from UV-visible to near-infrared, and high photo-stability if compared to corresponding bulk materials [61]. Specifically, the QDs like the metal halides perovskites such as $CsPbBr_3$ are considered newcomer optoelectronic materials with such rising attention in many research fields. For that, this material are used in several kind of applications spanning from the biology to physics [62]. These nanocrystals are usually sized from 2-20 nm, and they feature a very favorable combination of quantum effects related to the size of crystals presenting a wide advantage against the same material in a bulk format [62].

In our experiment, we have run trials using perovskite $CsPbBr_3$ QDs thin films produced by the Group of Research in Chemistry of Materials (at the Federal University of São João del-Rei). Here, we present the results obtained from a 10x and a 40x microscope objective micromachining optical setup. This work, besides being the first attempt produced in our lab, shows the design and parameters used to modify such thin films. Herein, the main idea is to aid a deeper understanding of the relation between threshold fluence and the number of incident pulses. This relation is named incubation effect and it characterizes the ablation process leading to the reduction of the threshold fluence as a function of the number of overlapped pulses.

6.2.2 Materials and Methods

Here the materials and methods for Perovskite samples are presented.

6.2.2.1 Perovskite

The perovskite films employed in our experiments were fully prepared and kindly provided by the Group of Research in Chemical of Materials of the Federal University of São João del-Rei. The researcher involved in this work were Caroline de Mayrinck, André Felipe Vale da Fonseca, Marco Antônio Schiavon. Thus, the preparation processes follow, as described by the authors below.

6.2.2.2 Materials and Methods

All the reagents were used without further purification. Octadecene (ODE) 90%, Oleic Acid (OA) 90%, Oleylamine (OLEA) ≥ 98%, Cesium carbonate (Cs_2CO_3) 99.9%, Hexane for HPLC ≥ 97.0% and Lead Bromide ($PbBr_2$) as perovskite precursors. All obtained from Sigma-Aldrich. The cesium-oleate solution was prepared according to the approach reported by Kovalenko and co-workers.[62] 0.0813 g of Cs_2CO_3, 0.250 mL of OA, and 4 mL of ODE were loaded in a three-neck flask and degassed under a vacuum at 120 °C for 1 h, followed by heating at 150 °C under a N_2 atmosphere until all Cs_2CO_3 reacted with OA.

Initially, 0.069 g of $PbBr_2$ and 0.5 mL of ODE were loaded in a three-neck flask and dried under a vacuum for 1 h at 120 °C. Then 0.5 mL of OLEA and 0.5 mL of OA were injected at 120 °C under N_2. After the complete dissolution of $PbBr_2$, the temperature was increased to 150 °C. Finally, 1 mL of hot (150 °C) Cs-oleate solution was quickly injected, and the reaction mixture was cooled by ice-bath after 5 s.

FTO glass (Aldrich) was ultrasonically cleaned in ultra-pure water, ethanol, isopropanol, and acetone, respectively, for 10 min each. After drying at room temperature, the NPs suspension was spin-coated onto the substrate at 800 rpm for 10 seconds, and then 2000 rpm for 5 seconds. All the thin films were kept in a glovebox at an inert atmosphere before the experiments.

The crystalline structure for the $CsPbBr_3$ QDs thin film was obtained by X-ray diffraction (XRD). The diffraction patterns were obtained on a Shimadzu XRD-6000 diffractometer, with Kα do Cu radiation, $\lambda = 1.5418\,\text{Å}$, graphite monochromator, scanning at 0.02 degrees, in the range of $2\theta = 10° - 70$ °.

6.2.3 Results and Discussion

The ground-state absorption (black lines) spectrum for the $CsPbBr_3$ QDs thin films are illustrated in Figure 38. As can be observed, the absorption spectrum presents a transition band located at 510 nm, which is related to the first exciton transition. Also, the small absorption (absorbance of 0.015) suggest the thin thickness of the QDs films, characteristic of the spin-coated technique. The photoluminescence spectrum (blue lines) presents a peak at 517 nm with a narrow linewidth. Such an outcome, along with the very small Stokes-Shift (33 meV on the order of thermal energy at room temperature), indicates the high optical quality of the sample.

Figure 38 - Absorption and emission spectra of the film of CsPbBr3

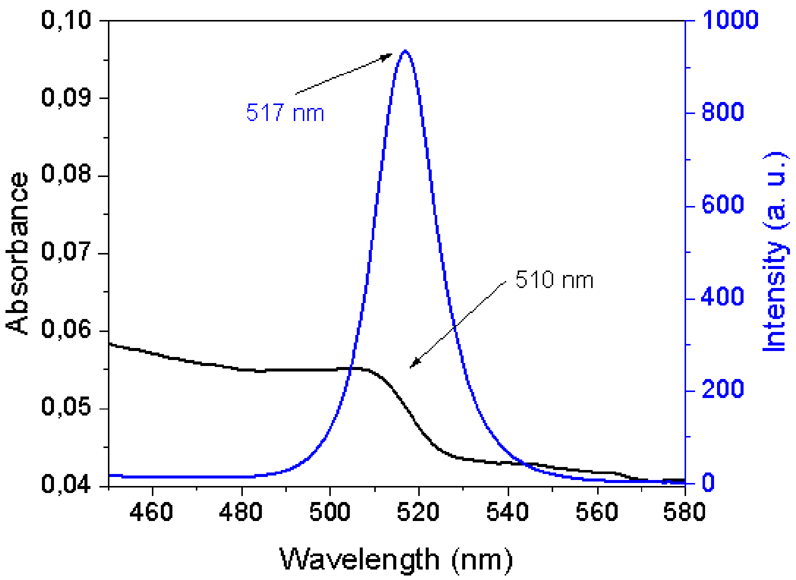

Source: Author.

Figure 39 shows the x-ray diffractogram for the $CsPbBr_3$ QDs thin films. As noted, XRD indicates the formation of a crystalline system referring to the thin film of perovskites. The XRD has a cubic phase crystalline system, belonging to the Pm-3m group in accordance with JCPDS card No. 00-054-0752. It is also observed the presence of reflections not belonging to the CsPbBr3 cubic phase. According to JCPDS card No. 01-054-0750, such reflections are attributed to the composition Cs_4PbBr_6, which commonly presents an orthorhombic phase in its structure, showing the presence of polymorphs in the perovskite lattice.

Figure 39 - XRD patterns of the CsPbBr3 films and suspension of perovskite nanocrystals

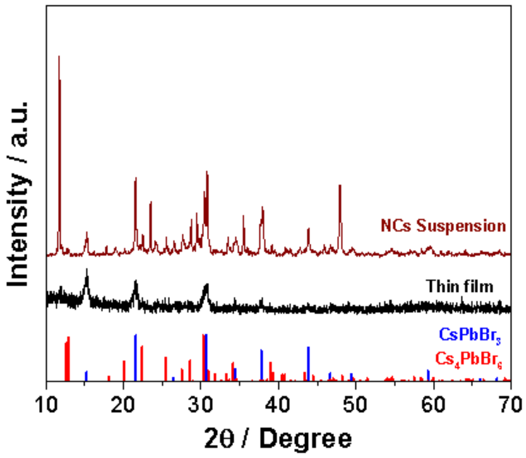

Source: Author.

Here, the setup was set to run at different speeds to determine the relationship between the average width and fluence. Both 10x and 40x microscope objectives were used, and their results will be presented separately. At next, some comments comparing both data are written to evaluate some important points achieved in this work.

For both 10x and 40x objective lenses, we have set different speeds and energies to obtain different grooves machined. Table 6 shows the speeds and the energies employed in the trials. It is important to say that all the speeds and energies were set for each trial. For instance, we set the first energy and change the speeds. Next, we set the second energy and vary the speeds again and so on. Graph 8 shows the average width of the grooves as a function of energy. In the graph, the black line represents the trial with speed set in 25 um/s whereas the magenta line shows the values for the fastest speed set in 200 um/s and varying the energies according to Table 6.

Figure 40 shows the trials obtained as a function of the pulse energy for the 10x microscope objective and translation speed of 25 um/s.

Graph 8 - Average width as a function of energy resulted from a 10x objective lens experiment

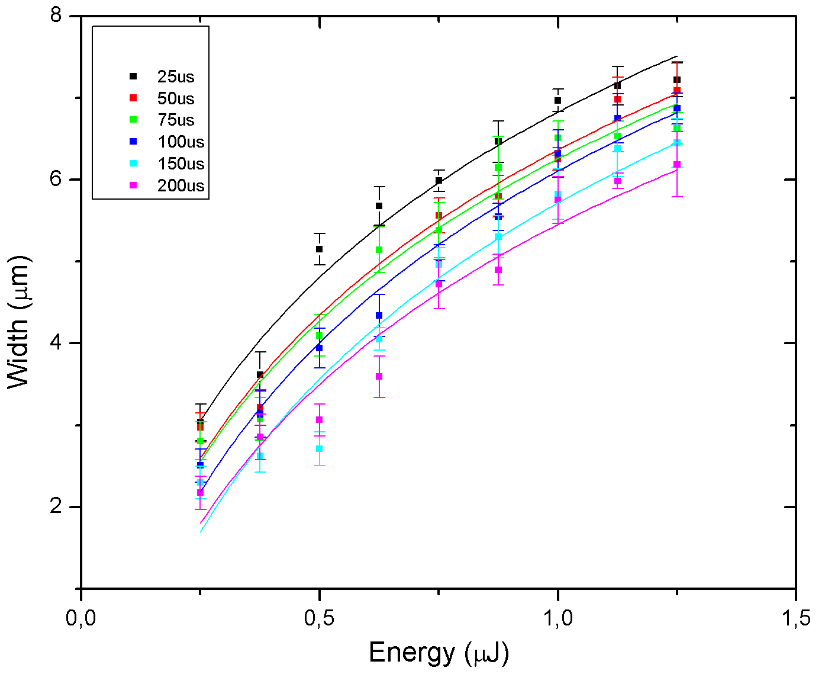

Source: Author.

As can be seen in Graph 8, for faster speeds such as 100 µm/s we have obtained grooves with average width varying from 1.8 µm to 2 µm. On the other hand, the slower speeds set in 25 µm/s and 50 µm/s have produced wider grooves with about 3 µm width. Besides, all the curves tend to saturable for pulse energy higher than 1 µJ. It happens because higher energies do not increase the spot size anymore, only providing more energy to the sample. As we are working with a nanosecond pulsed laser – long pulse duration – the high energy will aggressively damage the groove by spreading more shock waves and cracking the surface around the modified path.

Figure 40 - Grooves machined in each power set by the laser with a bar scale of 50 µm

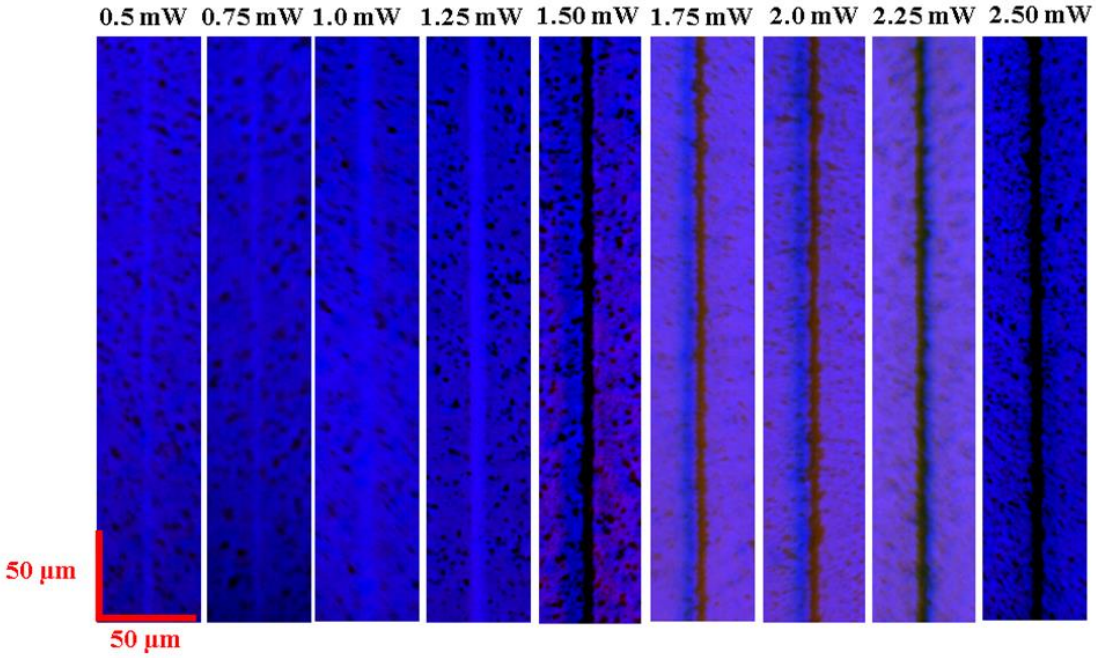

Source: Author.

Also, from the graph 8, we can see the behavior of the speed in relation to the energies. As explained before, at faster speeds, the laser spot interacts for shorter times rather than at slower speeds. Here, the fastest speeds have produced narrower lines rather than those slower. The cyan curve, for 150 um/s, produced narrower lines and those presented by the blue curve, representing the speed of 100 um/s, for instance.

In possession of these data, we aimed to calculate the threshold fluence provided by the laser and how it is related to the average width of the lines. Thus, we have obtained a new graph showing this information. As shown in section 3.4 – Micromachining Theory – the fluence F can is used to be expressed in J/cm^2 or mJ/cm^2. Therefore, graph 9 shows the square average width (r^2) in terms of fluence (F) (linear-log scale). As can be observed, a linear relationship is obtained, corroborating the theoretical model described by equation 3.35. Therefore, through this equation, we can found the threshold fluence, F_{th}, for each translation speed, through the slope coefficient of the straight line depicts in Graph 9.

Going forward, the last still important data obtained from the 10x trial is the relation between F_{th} and the number of pulses incidents over the sample, as shown next in graph 10. It can be seen that for small numbers of incident pulses, the threshold fluence has its highest values. It happens because if the specimen is reached by few laser pulses, so the energy has to be high enough to start modifying the surface with just a few interactions between laser and material. The contrary is also true.

Graph 9 - Square average width (r^2) in terms of Fluence from a 10x objective lens

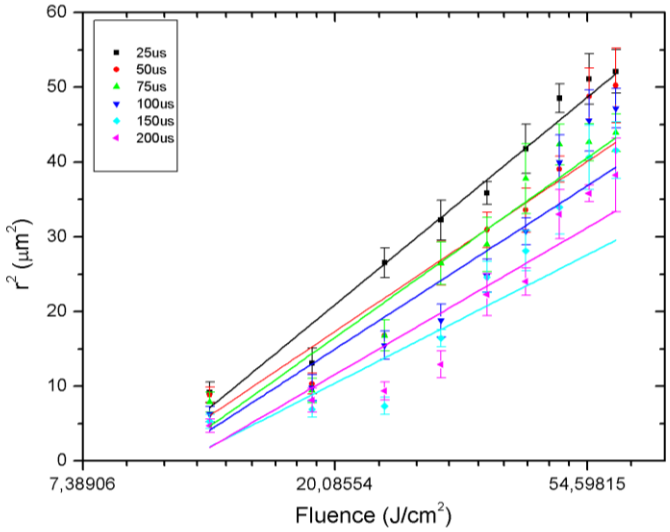

Source: Author.

For a higher number of incident pulses, the threshold fluence presents its smallest values, which in turn, implies in more interactions between laser pulses and material in which the surface is hit by more pulses. As a result, we have this declining aspect in the graph. However, from 65 pulses ahead, the curve seems to keep a steady evolution even by increasing the number of pulses.

Further, the 40x objective lens produced such similar curves besides its smaller values in a general overview. As explained before, the objectives differ from the NA number, which gathers the light narrower or wider. Thus, the 40x lens has a different NA number from the 10x one, which consequently has produced similar results with other values – for similar results reads curves with an analogous aspect in the next graphs.

Following the same reasoning from the previous paragraphs, we firstly exhibit the relation between the average width of the grooves with the pulse energy.

Graph 10 - Relation between the threshold fluence and the number of incident pulses for the 10x objective lens

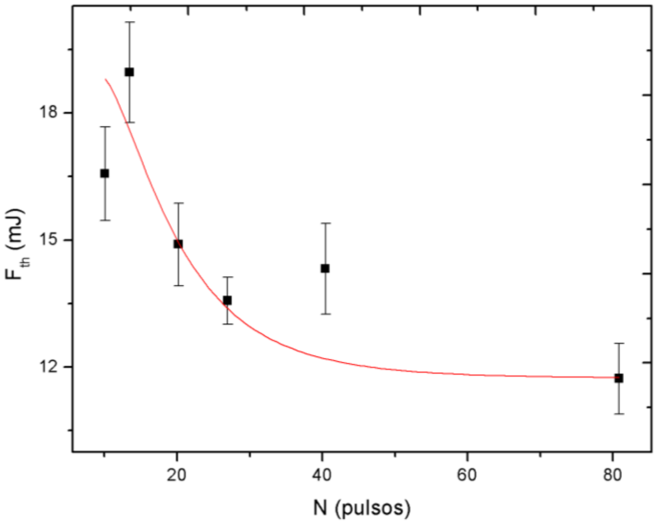

Source: Author.

Graph 11 illustrates such dependence and relation among those features wherein each curved line was set by keeping a constant speed. From the graph, we can infer that for energies higher than 1.25 μJ, the curves present a saturation trend, where again, there are no longer changes in the laser spot size, but there are still secondary damages caused by the heatwave that propagates along the lattice.

Further, as can be seen from the graph, the black line shows the results for the lowest speed, which is 25 μm/s. The trial images obtained for this translation speed as a function of the pulse energy are shown in Fig. 41. There is also a scale bar of 50 μm to help to compare the lines in which can be seen differences in them.

This translation speed has produced the widest grooves rather than those grooves machined under higher speeds, such as 100 µm/s or 200 µm/s. For the 25 µm/s trial, the black curve shows its initial value at about 2 µm, which is the narrowest line produced under such conditions. However, by increasing the energy per pulse, the width rises rapidly for the next three values until the energy of 0.75 µJ per pulse. After that point, the values rise until it starts tending the saturation region.

Graph 11 - Average width as a function of the energy per pulse for a 40x microscope objective lens

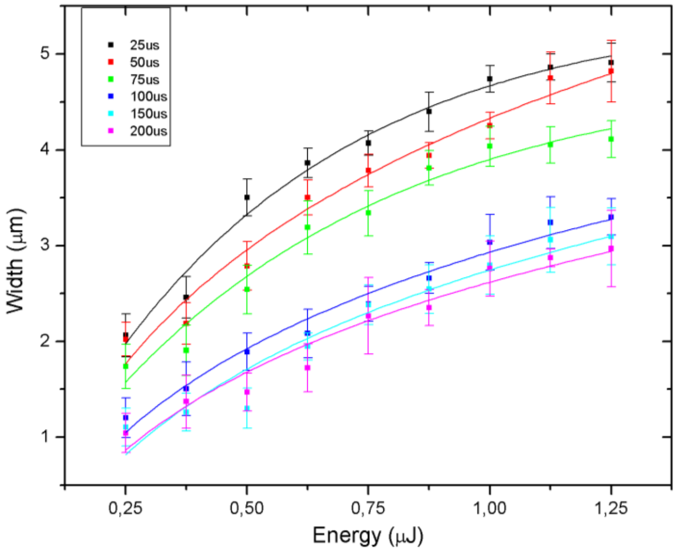

Source: Author.

Figure 41 - Picture showing the grooves machined under different laser powers using a 40x objective

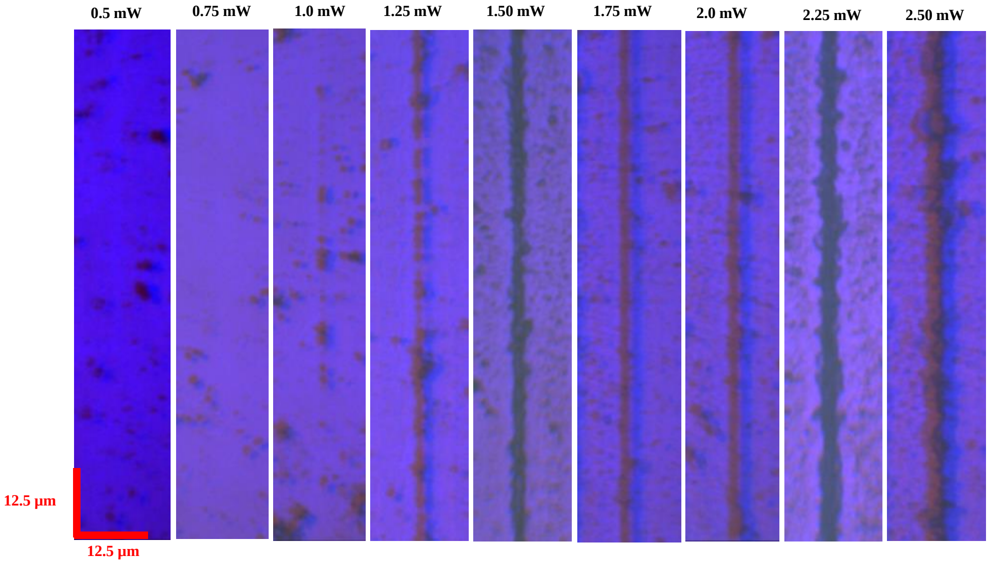

Source: Author.

In the aftermath, the data described in graph 11 allows us to plot a new graph, graph 12, similar to the one presented earlier where we set the average square width as a function of the Fluence. Here, the Fluence-axis has been set as ln scale, which eases the calculation of the threshold fluence following the same reasoning adopted in the results for the 10x objective lens. Thus, in spite of different absolute values compared to the previous results, these data have produced straight lines as expected. From the graph, it also can be observed that the straight lines have different slopes. The slope returned by the graph was used to evaluate the threshold fluence according to equation 3.34 and 3.35.

Graph 12 - Average square width as a function of Fluence for grooves machined by a 40x objective lens

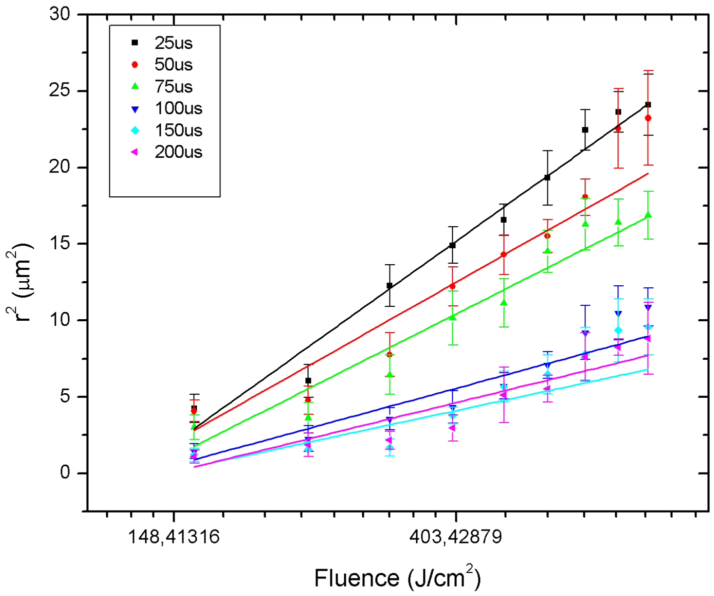

Source: Author.

Then, the threshold fluence evaluated from the data in graph 12 is presented as a function of the number of incident pulses in Graph 13. The threshold fluence is higher for a few pulses and has its slowest value at about 22 pulses targeting the sample. This difference occurs because of the energy required to start ablating the surface of the sample. It is also important to compare both graphs 10 – relative to the 10x objective data – and graph 13 relative to the 40x objective data. To illustrate so, minimum threshold fluence for the 10x objective is a bit smaller than 12 mJ/cm^2 while for 40x objective, the equivalent value point stands at about 2 mJ/cm^2. The number of pulses has its maximum value at 80 pulses (10x data) in which, for the 40x data, it stands at about only 22 pulses.

This difference, therefore, occurs because of the different NA from the objectives. As explained before, higher NA values are able to focus light more efficiently (smaller w_0). Thus, the peak intensity is much higher for the 40x objective as compared to the 10x objective. Therefore, the threshold energy required tends to be smaller as the contrary is also true, and it can be inferred from both graphs – higher NA value requires less energy and fewer pulses to start modifying the sample.

Graph 13 - Threshold fluence as a function of the number of pulses for grooves machined by a 40x objective lens

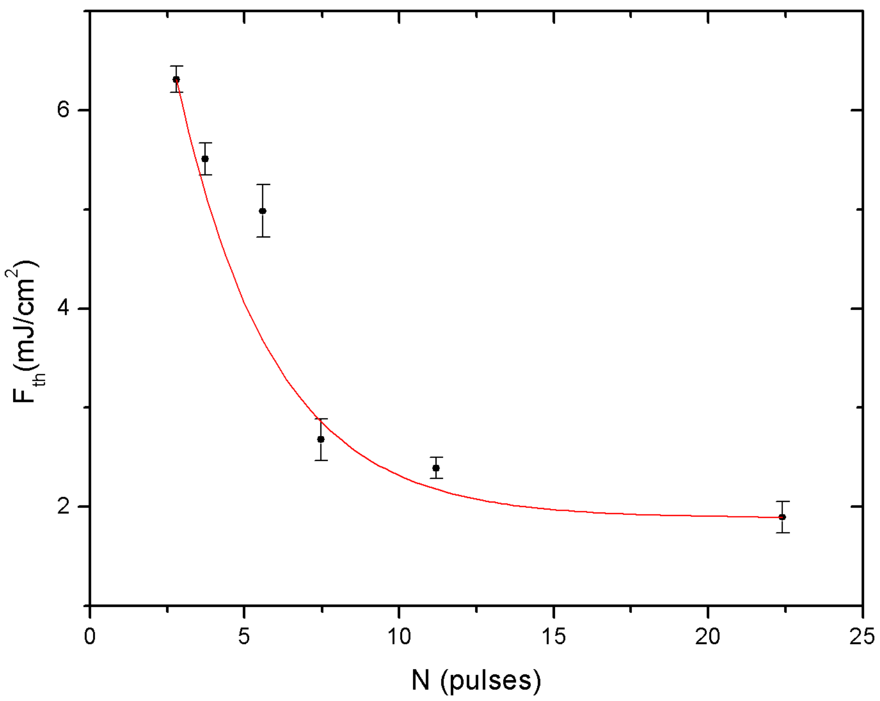

Source: Author

6.2.4 Remarkable Outcomes

As presented, faster speeds have produced narrower lines rather than slower speeds. In this work, therefore, we have obtained lines as small as 2 μm for the 10x lens and small as 0.8 μm for the 40x one. Also, the threshold fluence was determined as a function of the number of pulses, which indicates that the number of pulses interacting with the sample depends directly on the translation speed and w_0. From the experiments, we have obtained threshold fluences from 12 to 20 mJ/cm^2 for the 10x objective lens and from about 2 to 6 mJ/cm^2 for the 40x objective lens. Our results pointed out that the incubation effect for the $CsPbBr_3$ QDs thin films follow a similar tendency to the gallium nitride thin films [40], which F_{th} change significantly for the number of pulses between 1 and 50 (for 40x objective). On the other hand, the F_{th} value found here for $CsPbBr_3$ QDs thin films are much distinct. Thus outcome can be explained because we have used the pulse duration of 1 ns while the results reported in reference [40] making use of 160 fs pulse duration.

7 FINAL REMARKS

This work shows that the micromachining optical setup was well built, tested, and improved according to the needs evaluated by the trials and experiments, which in turn allowed the achievement of microstructured lines with an average width as small as about 1 µm. Such improvements were possible after analyzing data from gold and chitosan films initially and then, by the data from PMMA/azochromophores films and finally by the $CsPbBr_3$ QDs thin films.

For the PMMA/azochromophores films, we found two regimes of micromachining (ablation and superficial modification), and it points to new outcomes by using a nanosecond pulsed laser. Also, the general behavior of the samples in relation to the microscope objectives were as expected. At this point, the expected behavior of PMMA/azochromophores to the optical system was considered to be satisfactory in terms of increasing and decreasing the groove widths as the speed of translation, objective's NA, and laser energy was being changed over the process.

Regarding the $CsPbBr_3$ QDs thin films, we have obtained the incubation curves in two intensities regimes, i. e., by employing the 10x (low intensity) and 40x (low intensity) objectives. Our results show steady-state threshold fluences from 12 mJ/cm^2 and 2 mJ/cm^2 for the 10x and 40x objective lens, respectively. To best of our knowledge, it is the first time that incubation curves are obtained from the nanosecond laser micromachining. In the last decade, perovskite thin films are currently being widely studied due to its properties and a vast range of possible applications, in particular, ones related to the optoelectronic devices in reduced-scale. Therefore, such results to open the possibility to apply the laser micromachining to develop new or even to improve photonics devices based on the nanomaterials.

Finally, to show the capability of our laser micromachining system, in Figure 42 we illustrate a microstructure with the acronym of our Laboratory (LEOF: Laboratório de Espectroscopia Óptica e Fotônica) micromachined in a gold thin film (50 nm). This micromachining acronym was controlled by the home-made software using LabView language. It allowed to set up vectors commands that, in turn, controlled the stepper motors to produce such image. Overall, we still have to work to improve such circular letters as the "O" in the acronym.

Figure 42 - LEOF Acronym produced by our micromachining setup in a gold thin film

Source: Author.

REFERENCES

[1] GATTASS, R. R.; MAZUR, E. Femtosecond laser micromachining in transparent materials. **Nat. Photonics**, London, v. 2, n. 4, p. 219–225, 2008, doi: 10.1038/nphoton.2008.47. Available from https://www.nature.com/articles/nphoton.2008.47. Accessed in 9 Oct. 2019.

[2] GARMIRE, E. Nonlinear optics in daily life. **Opt. Express**, v. 21, n. 25, p. 30532–30544, 2013, doi: 10.1364/OE.21.030532. Available from: https://www.osapublishing.org/oe/fulltext.cfm?uri=oe-21-25-30532&id=275155. Accessed in: 11 Oct. 2019.

[3] HEIDARI, F. Micromachining: A new trend in manufacturing. **ASEE Annu. Conf. Expo. Conf. Proc.**, Atlanta. 2013. Available from: https://peer.asee.org/22292. Accessed in: 31 July 2020.

[4] MEIJER, J. *et al.* Laser Machining by short and ultrashort pulses, state of the art and new opportunities in the age of the photons. **CIRP Annals.** United States of America, v. 51, n. 2, p. 531–550, 2002, doi: https://doi.org/10.1016/S0007-8506(07)61699-0. Accessed in: 31 July 2020.

[5] SUN, X.; MASUZAWA, T. and FUJINO, M. Micro ultrasonic machining and its applications in MEMS. **Sensors Actuators A-physical - Sens. ACTUATOR A-PHYS.** Netherlands, v. 57, p. 159–164, Nov. 1996, doi: 10.1016/S0924-4247(97)80107-0. Available from: https://www.sciencedirect.com/science/article/abs/pii/S0924424797801070?via%3Dihub. Accessed in: 30 July 2019.

[6] REYNAERTS, D.; HEEREN, P-H.; BRUSSEL, H. Microstructuring of silicon by electro-discharge machining (EDM) - part I: Theory. **Sensors Actuators A-physical - Sens. ACTUATOR A-PHYS.** Netherlands, v. 60, p. 212–218, May 1997, doi: 10.1016/S0924-4247(97)01359-9. Available from: https://linkinghub.elsevier.com/retrieve/pii/S0924424797013599. Accessed in: 31 July 2020.

[7] GIETZELT, T. Mechanical Micromachining by Drilling, Milling and Slotting. *In*: GIETZELT, T. **Micromachining Techniques for Fabrication of Micro and Nano Structures**. Shanghai: Ed. Rijeka, IntechOpen, 2012, ch. 8, p. 159-182. Available from: https://www.intechopen.com/books/micromachining-techniques-

for-fabrication-of-micro-and-nano-structures/mechanical-micromachining-by-drilling-milling-and-slotting. Accessed in: 31 July 2020

[8] HAMAD, A. H. Effects of Different Laser Pulse Regimes (Nanosecond, Picosecond and Femtosecond) on the Ablation of Materials for Production of Nanoparticles in Liquid Solution. 1st ed. **InTechOpen**, DOI: 10.5772/63892. 2016, p. 305-327. Available from: https://www.intechopen.com/books/high-energy-and-short-pulse-lasers/effects-of-different-laser-pulse-regimes-nanosecond-picosecond-and-femtosecond-on-the-ablation-of-ma. Accessed in: 29 Feb 2020.

[9] HECHT, J. Short history of Laser development. **Applied Optics**. Florida, v. 49, p. 99-122, Sept. 2010, doi: 10.1117/1.3483597. Available from: https://www.osapublishing.org/ao/abstract.cfm?uri=ao-49-25-F99. Accessed in: 30 July 2019.

[10] SHANK, C. V.; BJORKHOLM, J. E.; KOGELNIK, H. Hybrid scattering in periodic waveguides. **Applied Physics Letters.** v. 22 n. 4(1973) p. 135-137. DOI:10.1063/1.1654585. Available from: https://aip.scitation.org/doi/10.1063/1.1654585. Accessed in: 30 July 2019.

[11] GARMIRE, E. M.; YARIV, A. Laser mode-locking with saturable absorbers. **IEEE Journal of Quantum Electronics**. London, v. 3, n. 6, p. 222-226, 1967. DOI: 10.1109/JQE.1967.1074489. Available from: https://ieeexplore.ieee.org/document/1074489. Accessed in: 20 Apr. 2020.

[12] IPPEN, E. P.; SHANK, C. V. Dynamic spectroscopy and subpicosecond pulse compression. **Applied Physics Letters.** v. 27, n. 9(1975) p. 488-490. DOI:10.1063/1.88544. Available from: https://aip.scitation.org/doi/abs/10.1063/1.88544. Accessed in: 30 July 2019.

[13] NEW, G. H. C. Nonlinear optics: the first 50 years. **IEEE Quantum Electron.** Michigan, v. 52, n. 4, p. 281-292, 2011. DOI: 10.1080/00107514.2011.588485. Available from: https://www-tandfonline.ez37.periodicos.capes.gov.br/doi/full/10.1080/00107514.2011.588485. Accessed in: 04 Sept 2020.

[14] IPPEN, E. P.; SHANK, C. V.; DIENES A. Passive mode locking of the cw dye laser. **Applied Physics Letters.** United States of America, v. 21, p. 348, 1972. DOI: 10.1063/1.1654406. Available from:

https://aip.scitation.org/doi/10.1063/1.1654406. Accessed in 04 Sept 2020.

[15] FORK, R. L.; GREENE, B. I.; SHANK, C. V. Generation of optical pulses shorter than 0.1 psec by colliding pulse mode locking. **Applied Physics Letters.** United States of America, v. 38, n. 9, p. 671–672, May 1981, doi: 10.1063/1.92500. Available from: https://aip-scitation-org.ez37.periodicos.capes.gov.br/doi/10.1063/1.92500. Accesed in 04 Sept 2020.

[16] NISOLI, M. *et al.*, Compression of high-energy laser pulses below 5 fs. **Optics Letters.** Massachusetts, v. 22, p. 522–524, 1997, doi: 10.1364/OL.22.000522. Available from: https://osapublishing.ez37.periodicos.capes.gov.br/ol/abstract.cfm?uri=ol-22-8-522. Accessed in: 04 Sept. 2020.

[17] ZHAO, K.; ZHANG, Q.; CHINI, M.; *et al.* Tailoring a 67 attosecond pulse through advantageous phase-mismatch. **Optics Letters.** Massachusetts, v. 37, n. 18, p. 3891–3893, 2012, DOI: 10.1364/OL.37.003891. Available from: https://osapublishing.ez37.periodicos.capes.gov.br/ol/fulltext.cfm?uri=ol-37-18-3891&id=241459. Accessed in. 30 July 2020.

[18] DAVIS, K. M.; MIURA, SUGIMOTO, K. N.; *et al.* Writing waveguides in glass with a femtosecond laser. **Optics Letters.** v. 21, n. 21, p. 1729-1731, 1996, doi: 10.1364/OL.21.001729. Available from: https://osapublishing.ez37.periodicos.capes.gov.br/ol/abstract.cfm?uri=ol-21-21-1729. Accessed in: 30 July 2020.

[19] JIA, Y.; CHEN, F.; VÁZQUEZ DE ALDANA J. Efficient continuous-wave laser operation at 1064 nm in Nd:YVO4 cladding waveguides produced by femtosecond laser inscription. **Optics Express.** v. 20, p. 16801–16806, Jul. 2012, doi: 10.1364/OE.20.016801. Available from: https://osapublishing.ez37.periodicos.capes.gov.br/oe/fulltext.cfm?uri=oe-20-15-16801&id=239717. Accessed in: 30 july 2020.

[20] ALMEIDA, G. F. B. **Femtosecond laser writing of nonlinear waveguides in Gorilla® Glass and L-threonine organic crystals**. 2018. 100 p. Thesis (PhD in Physics) - University of São Paulo, São Carlos, SP, 2018.

[21] KRCHNAVEK, R. R.; LALK, G. R.; HARTMAN, D. H. Laser direct writing of channel waveguides using spin-on polymers. **Jornal of Applied. Physics**.

Middletown, v. 66, n. 11, p. 5156–5160, Dec. 1989, doi: 10.1063/1.343750. Available from: https://aip-scitation-org.ez37.periodicos.capes.gov.br/doi/10.1063/1.343750. Accessed in: 30 July 2020.

[22] MEADOWS, M. D. NMR, 3D Analysis, Photopolymerization. Advances in Polymer Science. **Journal of American Chemical Society.** Washington D.C, v. 127, n. 32, p. 11530, Aug. 2005, doi: 10.1021/ja041007+. Available from: https://pubs.acs.org/doi/10.1021/ja041007%2B. Accessed in 04 Nov. 2020.

[23] LAFRATTA, C. N.; FOURKAS, J. T.; BALDACCHINI, T. Multiphoton Fabrication. **Angewandte Chemie International Edition**. Weinheim, v. 46, n. 33, p. 6238–6258, 2007, doi: 10.1002/anie.200603995. Available from: https://onlinelibrary.wiley.comdoi/abs/10.1002/anie.200603995. Accessed in 30 july 2020.

[24] CHEN, F. *et al.* Maskless fabrication of concave microlens arrays on silica glasses by a femtosecond-laser-enhanced local wet etching method. **Optics Express.** Massachusetts, v. 18, p. 20334–20343, Sept. 2010, doi: 10.1364/OE.18.020334. Available from: https://www.osapublishing.org/oe/abstract.cfm?uri=oe-18-19-20334. Accessed in 11 Sept. 2019.

[25] LI, C. Importance of Nonlinear Optics. in: **Nonlinear Optics: Principles and Applications**, 1st edition, Singapore, Shangai: Springer Singapore, 2017, p. 1–5. DOI: 10.1007/978-981-10-1488-8. Available from: https://www.springer.com/gp/book/9789811014871. Accessed in 9 Aug. 2019.

[26] JACKSON, J. D. **Classical electrodynamics**. Third edition. New York : Wiley, 1999. 808p.

[27] BOYD, R. W. “Chapter 2 - Wave-Equation Description of Nonlinear Optical Interactions,” in **Nonlinear Optics (Third Edition),** R. W. Boyd, Ed. Burlington: Academic Press, 2008, p. 69–133.

[28] Verbiest, T., Clays, K., & Rodriguez, V. Second-order Nonlinear Optical Characterization Techniques. CRC Press. 2009. DOI: https://doi.org/10.1201/9781420070736. 192 p.

[29] BOYD, R. W. “Chapter 1 - The Nonlinear Optical Susceptibility,” in **Nonlinear Optics (Third Edition)**, R. W. Boyd, Ed. Burlington: Academic Press, 2008, p. 1–67.

[30] GAUSSIAN BEAMS. Available from: https://en.wikipedia.org/wiki/Gaussian_ beam. Accessed in: 28 Sept. 2020.

[31] PASCHOTTA, R. **Beam Waist**. 2008. Available from: https://www.rp-photonics.com/ beam_waist.html. Accessed in: 19 June 2020.

[32] PASCHOTTA, R. **Gaussian Beams**. 2017. Available from: https://www.rp-photonics.com/gaussian_beams.html. Accessed in: 3 Aug. 2020.

[33] MACHADO, L. M.; SAMAD, R. E.; ROSSI, W. DE *et al*. D-Scan measurement of ablation threshold incubation effects for ultrashort laser pulses. **Optics Express.** Massachusetts, v. 20, n. 4, p. 4114–4123, 2012, doi: 10.1364/OE.20.004114. Available from: http://www.opticsexpress.org/abstract.cfm?URI=oe-20-4-4114. Accessed in: 28 Sept. 2020.

[34] PASCHOTTA, R. **Objectives**. 2008. Available from: https://www.rp-photonics.com/objectives.html. Accessed in: 19 June 2020.

[35] PASCHOTTA, R. **Focal Distance**. 2008. Available from: https://www.rp-photonics.com/focal_distance.html. Accessed in: 19 June 2020.

[36] DAVIDSON, M. W. **Numerical Aperture and Resolution**. 2018. Available from: https://micro.magnet.fsu.edu/primer/anatomy/numaperture.html. Accessed in: 19 June 2020.

[37] PASCHOTTA, R. **Spherical Aberrations**. 2019. Available from: https://www.rp-photonics.com/spherical_aberrations.html. Accessed in 10 Aug. 2020.

[38] K. R. H. E. K. M. W. D. SPRING;, “Microscope Objectives Introduction,” 2018. https://www.olympus-lifescience.com/en/microscope-resource/primer/anatomy/objectives/. Accessed in 10 Aug. 2020.

[39] PASCHOTTA, R. **Fluence**. 2008. Available from: https://www.rp-photonics.com/fluence.html. Accessed in: 19 June 2020.

[40] DE ALMEIDA, G. F. B. *et al.*, Incubation effect during laser micromachining of GaN films with femtosecond pulses. **Journal of Materials Science: materials in electronics.** New York, v. 30, n. 18, p. 16821–16826, 2019, doi: 10.1007/s10854-019-01373-2. Available from: http://dx.doi.org/10.1007/s10854-019-01373-2 PP. Accessed in: 31 July 2020.

[41] CHICHKOV, B.; MOMMA, C.; NOLTE, S.; *et al*. Femtosecond, picosecond and nanosecond laser ablation of solids. **Applied Physics A.** New York, v. 63, n. 2, p. 109–115, 1996, doi: 10.1007/BF01567637. Available from:

http://link.springer.com/10.1007/BF01567637. Accessed in: 21 July 2020.

[42] MOMMA, C.; *et al.*, Short-pulse laser ablation of solid targets. **Optics Communications.** Netherlands, v. 129, n. 1–2, p. 134–142, 1996, doi: 10.1016/0030-4018(96)00250-7. Available from: https://linkinghub.elsevier.com/retrieve/pii/0030401896002507. Accessed in: 21 July 2020.

[43] BROWN, M.; ARNOLD, C., Fundamentals of Laser-Material Interaction and Application to Multiscale Surface Modification. In: Sugioka K., Meunier M., Piqué A. **Laser Precision Microfabrication.** Berlin, v. 135, 2010, p. 91–120. DOI: https://doi.org/10.1007/978-3-642-10523-4_4 Available from: http://link.springer.com/10.1007/978-3-642-10523-4_4. Accessed in: 21 July 2020.

[44] HAN, J.; LI, Y. Interaction Between Pulsed Laser and Materials. In: Jakubczak, K. **Lasers - Application in Science and industry.** Shanghai, InTech, v. 1, p. 109-130, 2011.

[45] VISKUP, A.; RICHARD, E. Effects of Different Laser Pulse Regimes (Nanosecond, Picosecond and Femtosecond) on the Ablation of Materials for Production of Nanoparticles in Liquid Solution. In **High Energy and Short Pulse Lasers**, Rijeka: IntechOpen, 2016, ch. 12. Available from: https://doi.org/10.5772/63892. Accessed in: 29 Feb. 2020.

[46] WANG, X. Y., RIFFE, D.; LEE, Y.-S.; DOWNER, M. C. Time-resolved electron-temperature measurement in a highly excited gold target using femtosecond thermionic emission. **Phys. Rev. B. Condens. Matter**, v. 50, p. 8016–8019, Oct. 1994, doi: 10.1103/PhysRevB.50.8016. Available from: https://link.aps.org/doi/10.1103/PhysRevB.50.8016. Accessed in: 29 Feb. 2020.

[47] R. W. SCHOENLEIN, W. Z. LIN, J. G. FUJIMOTO, and G. L. EESLEY, “Femtosecond studies of nonequilibrium electronic processes in metals,” **Physics Review Letters.** v. 58, n. 16, p. 1680–1683, 1987. DOI: 10.1103/PhysRevLett.58.1680. Available from: https://link.aps.org/doi/10.1103/PhysRevLett.58.1680. Accessed in: 31 July 2020.

[48] KNOWLES, M.; RUTTERFORD, G.; KARNAKIS, D.; FERGUSON, A. Micro-machining of metals, ceramics and polymers using nanosecond lasers. **International Journal of Advanced Manufacturing Technology.** United Kingdom, v. 33, n. 1–2, p. 95–102, 2007, doi: 10.1007/s00170-007-0967-2.

Available from: http://link.springer.com/10.1007/s00170-007-0967-2. Accessed in: 29 Feb. 2020.

[49] ROMERO, A. L. S.; BARBANO, E. C.; MISOGUTI, L. Sistema computadorizado para deslocamento de amostra com motor de passo utilizando o L298: aplicação na técnica de varredura-Z. **Revista Brasileira de Ensino Física**. São Paulo, v. 41, n. 4, 2019. Available from: https://www.scielo.br/scielo.php?script=sci_arttext&pid=S1806-11172019000400403&tlng=pt. Accessed in: 1 June 2020.

[50] N. B. TOMAZIO, A. L. S. ROMERO, and C. R. MENDONCA, “Desenvolvimento de um obturador de feixe óptico utilizando um disco rígido de computador,” **Revista Brasileira de Ensino de Física**. São Paulo, v. 40, n. 1, 2018. Available from: https://www.scielo.br/scielo.php?script=sci_arttext&pid=S1806-11172018000100407&lng=pt&tlng=pt. Accessed in: 1 June 2020.

[51] ARDUINO. 2020. Available from: www.arduino.cc. Accessed in 15 Mar. 2019.

[52] STEPPER MOTOR. 2020. Available from: en.wikipedia.org/wiki/Stepper_motor. Accessed in 19 June 2020.

[53] SI, J.; QIU, J.; ZHAI, J.; *et al.* Photoinduced permanent gratings inside bulk azodye-doped polymers by the coherent field of a femtosecond laser. **Applied Physics Letters.** United States of America, v. 80, n. 3, p. 359–361, Jan. 2002, doi: 10.1063/1.1435808. Available from: http://aip.scitation.org/doi/10.1063/1.1435808. Accessed in: 11 June 2019.

[54] FERREIRA, P. H. D.; STEFANUTTI, R.; PAVINATTO, F. J.; *et al.* Femtosecond laser fabrication of waveguides in DR13-doped PMMA. **Optics Communications.** Netherlands, v. 318, p. 53–56, 2014, doi: https://doi.org/10.1016/j.optcom.2013.12.066. Available from: http://www.sciencedirect.com/science/article/pii/S0030401813012145. Accessed in: 8 June 2019.

[55] REIFLER, F. A.; HUFENUS, R.; KREHEL, M.; *et al.* Polymer optical fibers for textile applications – Bicomponent melt spinning from cyclic olefin polymer and structural characteristics revealed by wide angle X-ray diffraction. **Polymer.** Austin, v. 55, n. 22, p. 5695–5707, 2014, DOI: 10.1016/j.polymer.2014.08.071. Available from: https://www.sciencedirect.com/science/article/abs/pii/S0032386114007769?via%3Dihub. Accessed in 8 June 2019.

[56] DERKOWSKA-ZIELINSKA, B.; *et al.* Optical characterization of heterocyclic azo

dyes containing polymers thin films. **Applied Surface Science.** Netherlands, v. 421, p. 361-366. Dec. 2016, doi: 10.1016/j.apsusc.2016.12.080. Available from: https://linkinghub.elsevier.com/retrieve/pii/S0169433216327970. Accessed in: 31 July 2020.

[57] NATANSOHN,A.; ROCHON, P.; GOSSELIN, J.; *et al.* Azo polymers for reversible optical storage. 1. Poly[4'-[[2-(acryloyloxy)ethyl]ethylamino]-4-nitroazobenzene]. **Macromolecules**. Washington D.C., v. 25, n. 8, p. 2268–2273, Apr. 1992, doi: 10.1021/ma00034a031. Available from: https://doi.org/10.1021/ma00034a031. Accessed in: 31 july 2020.

[58] MARANESI, L. **Armazenamento Óptico Reversível em Filmes Guest-host contendo Compostos Azoaromáticos em Forma de V dispersos em uma matriz de Polimetilmetacrilato.** 2019. 73 p. Dissertação (Mestrado em Engenharia e Ciência dos Materiais) - Universidade Federal de Alfenas, Poços de Caldas, MG, 2019.

[59] GRIM, J.; MANNA, Q. L.; MOREELS, I. A sustainable future for photonic colloidal nanocrystals. **Chemical Society Reviews.** London, v. 44, n. 16, p. 5897–5914, 2015, doi: 10.1039/C5CS00285K. Available from: http://dx.doi.org/10.1039/C5CS00285K. Accessed in: 23 June 2020.

[60] PANFIL, Y. E.; ODED, M.; BANIN, U. Colloidal Quantum Nanostructures: Emerging Materials for Display Applications. **Angewandte Chemie International Edition.** Darmstadt,, v. 57, n. 16, p. 4274–4295, Apr. 2018, doi: 10.1002/anie.201708510. Available from: https://onlinelibrary.wiley.com/doi/full/10.1002/anie.201708510. Accessed in: 23 June 2020.

[61] ANTOLINI, F.; ORAZI, L. Quantum Dots Synthesis Through Direct Laser Patterning: A Review. **Frontiers in Chemistry.** Vancouver, v. 7, p. 252, 2019. DOI: 10.3389/fchem.2019.00252 Available from: https://www.frontiersin.org/article/10.3389/fchem.2019.00252. Accessed in 23 Sept. 2019.

[62] PROTESESCU, L.; *et al.* Nanocrystals of Cesium Lead Halide Perovskites ($CsPbX_3$, X = Cl, Br, and I): Novel Optoelectronic Materials Showing Bright Emission with Wide Color Gamut," **Nano Letters.** Evanston, v. 15, n. 6, p. 3692, 2015, doi: 10.1021/nl5048779. Available from: https://pubs.acs.org/doi/10.1021/nl5048779. Accessed in: 22 June 2020.

APPENDIXES

APPENDIX A – CHITOSAN AND GOLD FILMS

1 CHITOSAN FILMS

Chitosan films were composed, as a receipt, of 10 mg of chitosan for 1 ml of a 1% Hydrochloric Acid (HCl) solution. However, in a way to have more solutions for tests, we usually made 100 mg of Chitosan for 10 ml of HCl.

Chitosan is a bio-substrate that needs to be solubilized in an ultrasound machine the helps the solution become more homogeneous. From our experience, the best time for solubilizing the Chitosan in HCl is about 48 min with a pipe filled in the ultrasound. After that, it was necessary to filter the insolubilized particles using a 14 µm scale filter. The average time to filtrate the solution lasts about 48 hours to be all filtered.

In sequence, this homogenous solution was taken using a 200µL pipette in which the material was deposed over a transparent circular glass to dry. For each test, two glasses were filled with 500 µL and other two glasses filled with 600 µL. This difference was to make sure which concentration would be flatter after drying. The drying process takes over 24 h, and a specific atmosphere has to be created. Finally, it is necessary to mention that for all film produced the level of the basis was checked in many directions to prevent making unlevelled samples.

Figure 43 - Chitosan film produced at LEO&F

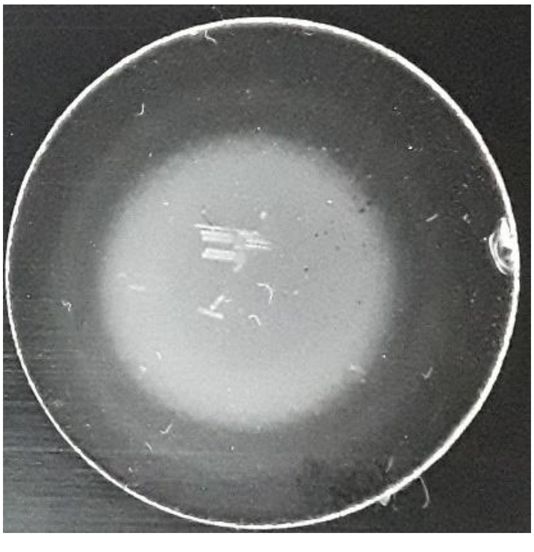

Source: Author.

2 GOLD FILMS

The gold films are produced at the LNNANO laboratory (National Laboratory of Nanotechnology) located in Campinas/SP. Gold substrate does not present a very good grip or adherence in the glass. An intermediate layer is put between the glass and the gold. This intermediate layer consists of a 2 nm Chromo – the metal Chromo – that works as a grip for gold and glass. The gold layer, however, is a 50nm thickness film that is placed over the Chromo layer. The technique employed to make such a film is named “sputtering”.

APPENDIX B - MICROMACHINING IN GOLD AND CHITOSAN

As introduced, the presented data for Gold and Chitosan served well its purpose of giving good directions to improve the optical setup. However, the optical setup, for these tests, was not ready. To say so, as explained before, the setup for these two different tests had only one telescope to enlarge the spot size, for instance.

It is important to emphasize that we expected that the increase of the pulse energy causes an increase in the linewidth. On the other hand, as the translation speed increases, the average width shall decrease because of the repetition rate of the laser beam, which remains constant during the process. For that reason, the expected behavior showed in the Graphs may appoint such a saturation region in which the width of the line does not increase anymore.

The repetition rate is an essential feature of micromachining. In our experiment, such a parameter was maintained constant at 2000 Hz. As a result, translating the sample at lower speeds, such as 50μm/s, more pulses reach the sample causing a more extended interaction for each second. However, at higher translation speeds, 300 μm/s, for instance, the sample moves faster, which leads to a shorter interaction between laser and substrate. Thus, this quicker interaction shall cause fewer modifications to the surface of the sample that, in turn, may represent more steady lines after the process. We analyzed all the pictures by using open-source software called ImageJ version 1.52a leased by the National Institutes of Health from USA.

1 MICROMACHINING IN GOLD

The tests in gold were measured by different translation speeds and energy per pulse. Figure 44 shows the effect of the pulse energy on the linewidth of the microstructure. The lines were made under the following conditions: translation speed: 50μm/s; repetition rate: 2000 Hz; excitation wavelength: 532 nm. Here, we used pulse energy of (a) 10nJ; (b) 20nJ and (c) 30 nJ. Thus, from (a) to (b) it is observed the increase in the width while from (b) to (c) there is a smaller difference. It is essential to point out that any defects over the surface may interfere in the process.

Figure 44 - Micromachining in Gold film at speed of 50μm/s with the energies per pulse of 10nJ, 20nJ and 30nJ, respectively

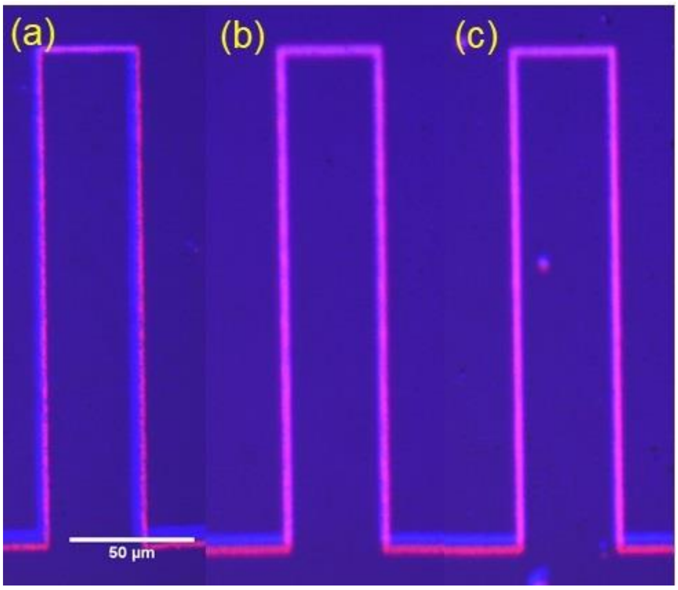

Source: Author.

It is seen from the pictures in different colors. The dark blue is the surface of the film, while the pink color is the micromachined lines. From (a) we can see very tiny lines, in which the microstructure was not steady constant all over the sample. We may see some gaps that we interpret that 10 nJ was not enough energy to make it steady. In comparison, looking at part (c) in which the sample was modified with 30nJ, we got very stable lines keeping constant the same factors like speed and repetition rate like said before.

Besides these three pictures, the tries for gold were run in seven different speeds – 50 µm/s; 100 µm/s; 150 µm/s; 200 µm/s; 250 µm/s; 300 µm/s; 400 µm/s, respectively – using a microscope microscope objective lens of 20x, NA (number of aperture of 0,50). As a result, we analyzed the lines comparing the average width with the energy per pulse and next, with the speed of translation. These data were converted into Graphs for a better understanding. Next, the Graphs and a short description and comparison are presented.

Firstly, let us take for analysis the Graphs 14, 15 and 16 of Average Width *versus* Pulse Energy. Here, for 50um/s, we obtained a similar increase for each energy displayed. Also, the most variable data was related to the energy of 30 nJ – there is a more significant error bar for this point. On the other hand, for the first two sets of values, the error bar is tiny, which indicates more constant values from one line to another.

Graph 14 - Average width related to the pulse energy at the speed of 50 µm/s for a gold film

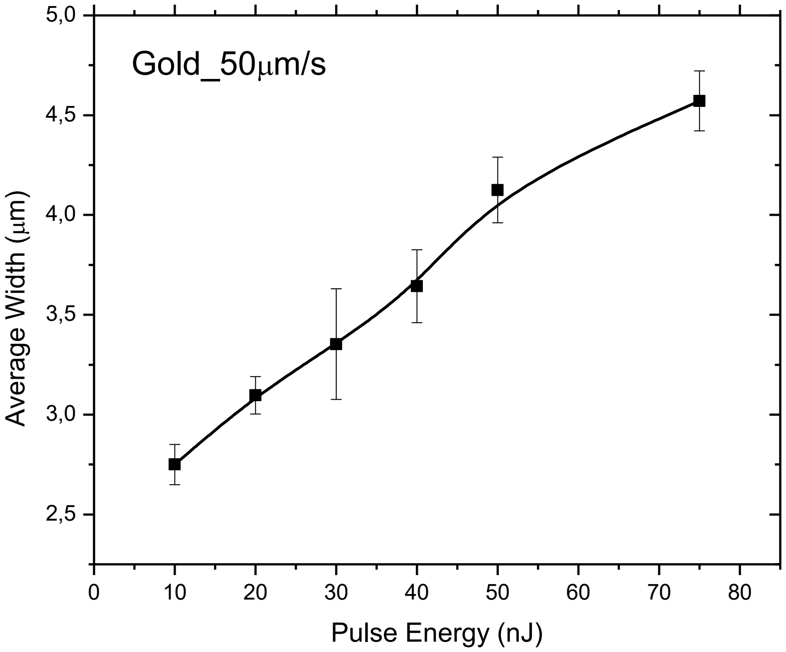

Source: Author.

Secondly, it is presented the 250 μm/s and 400 μm/s data side by side. As discussed before, a saturation region was expected with the increase of energy. As a result, for these two speeds, this behavior occurred, especially between 30 and 60 nJ, for instance. In both situations, the most irregular lines are related to 40 nJ per pulse. Meanwhile, we can infer that a smaller error bar like those for 50 nJ indicates more steady machined lines.

Finally, an example of a Graph of Width *versus* Speed is shown. As expected, when the energy is kept constant, lower speeds should make larger lines; likewise, the higher speeds should make more narrow lines.

Graph 15 - Average width for two different speeds in relation to the pulse energy for gold film

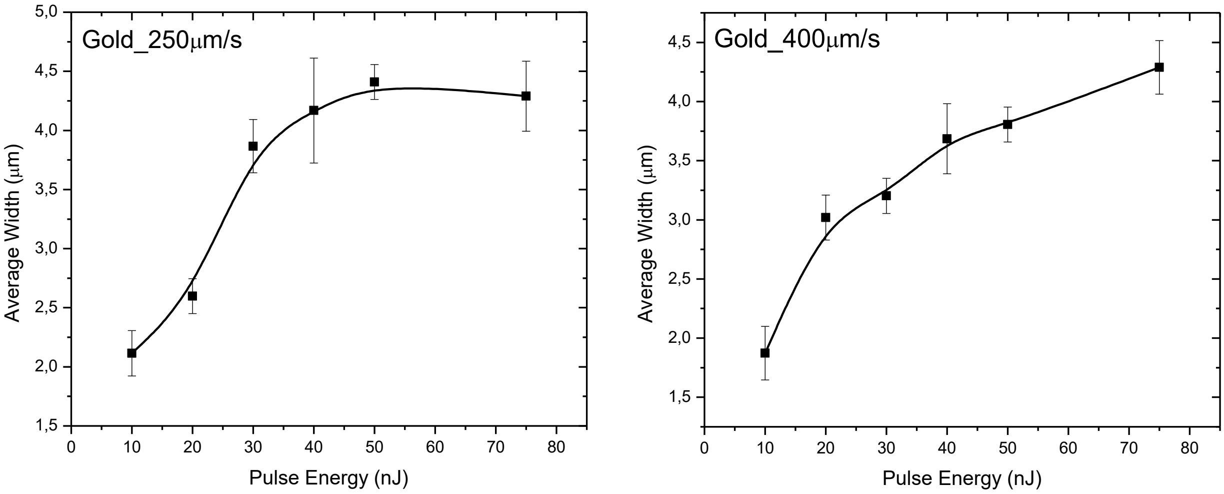

Source: Author.

Graph 16 - Average width for different speeds at constant energy of 10 nJ for the gold film

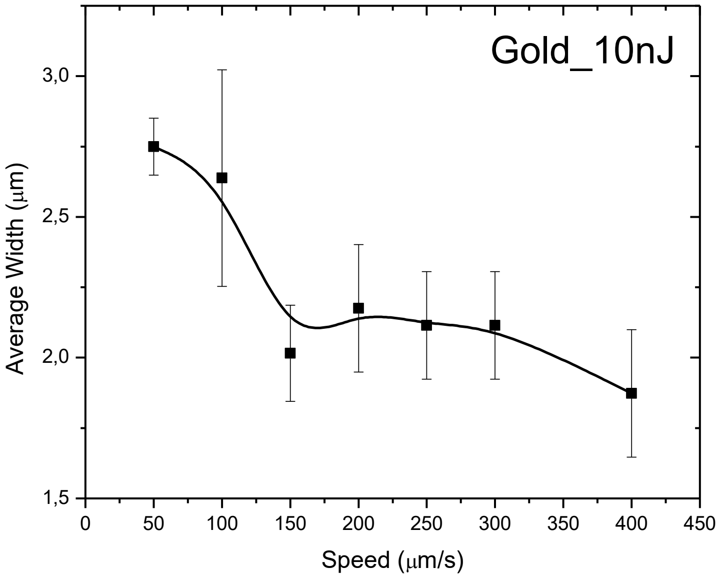

Source: Author.

The best results, although it was just initial tries, was the lower speed of 50 µm/s that reported the smaller error bar. Somehow, for this case, the setup promoted such steady moves on the sample with fewer issues.

2 MICROMACHINING IN CHITOSAN

Similarly, to gold films, the chitosan films were submitted by the same tests, which includes the same range of speeds, repetition rate, and excitation wavelength. Therefore, as the chitosan is completely transparent at 532 nm (excitation wavelength), the microstructures reported here are associated with the nonlinear optical effect (two-photon absorption). However, unlike the gold films which absorb energy at 532 nm (resonant process, absorption coefficient 5.27 x 10^5 cm^{-1}), the energies for chitosan were a bit higher due to the fact it is another type of material, and the process is nonlinear. This difference in the range of powers happens because another kind of material presents new characteristics such as mechanical and thermal resistance. In this way, it is needed to find another threshold energy that means the first energy able to start modifying the material, indeed.

Also, chitosan films have visible porosity that can be observed when they put on the microscope. These tests we also made with a microscope objective of 20x. Speeds from 50 μm/s to 200 μm/s were used at the same intervals from one to another. Next, follow the data analysis for chitosan films. First, I present a picture of the micromachining lines at the naked eye. The picture was taken by a popular smartphone with no zoom. It can be seen in Fig. 30, at least nine separated blocks. Each of these blocks represents an amount of 240 lines of the same rectangular pattern, as shown for gold. Also, you may see some blocks narrower than others, which indicates that these are blocks made with smaller values of energy. Therefore, it produces narrow lines. Figure 45 shows a comparison between machined lines with the same energy.

Figure 45 - Chitosan film micromachining by LEO&F at the naked eye picture

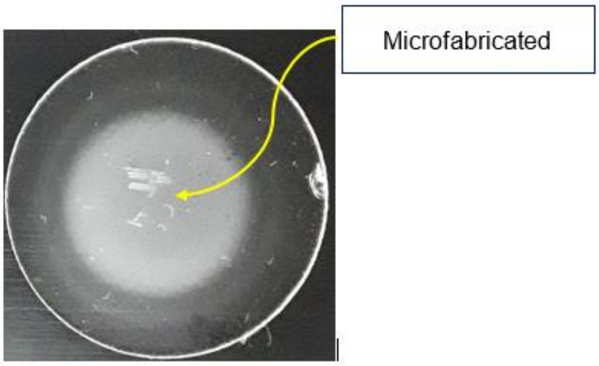

Source: Author.

Figure 46 shows a comparison between machined lines with the same energy (0,425 μJ) by changing the translation speed (from 50 μm/s to 200 μm/s with an increment of 50 μm/s). We may see that pictures (c) and (d) are narrower than parts (a) and (b). Now, let us observe the results for the speed of 150 μm/s for five different energies (from (a) to (e) we used 0,425 μJ; 0,75 μJ; 1,25 μJ; 1,75 μJ; 2,75 μJ), as shown in Figure 46. As can be noted, there is an increase in the width of the microstructure as a function of the pulse energy. Pointing out part (e) in Figure 47, we observed that for higher energies, there is the occurrence of a tiny groove in the middle of the line. Thus, it indicates that chitosan was being ablated, and the glass started to come up. The chitosan is transparent.

Figure 46 - Pictures of machined chitosan from a 20x microscope objective

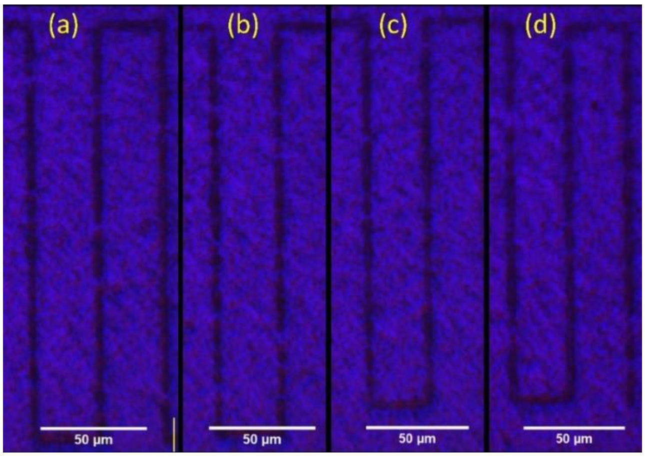

Source: Author.

Figure 47 - Chitosan machined at a constant speed by increasing the energy

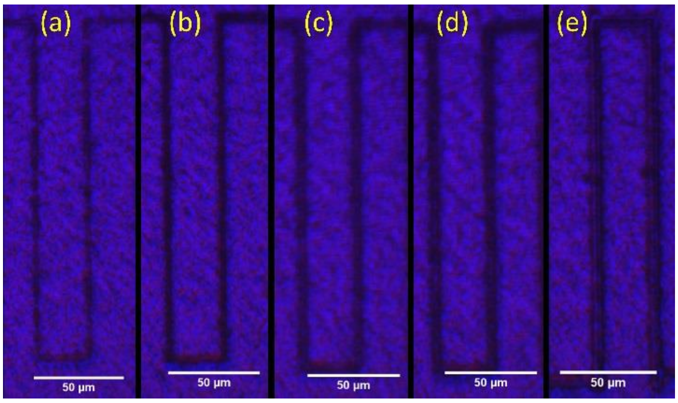

Source: Author.

Following the same reasoning from the gold section, a brighter comprehension of the data could be analysed with Graphs. First, a comparison between the average widths *versus* the pulse energies. Further, the average width *versus* the translation speeds follows with a short discussion about it.

The graphs show, therefore, the results obtained for chitosan at the speeds of 50 μm/s and 150 μm/s, for instance. To say so, the speed of each situation was kept constant while changing the pulse energy. Considering at first the 50 μm/s machined lines, we may infer that in the lower energies, more steady lines were produced as pointed out by the smaller standard deviation. At the same time, the curve represents, overall, an increase of the width as a function of the rise of the energy, as expected.

Graph 17 - Comparison of average width for two different speeds in Chitosan

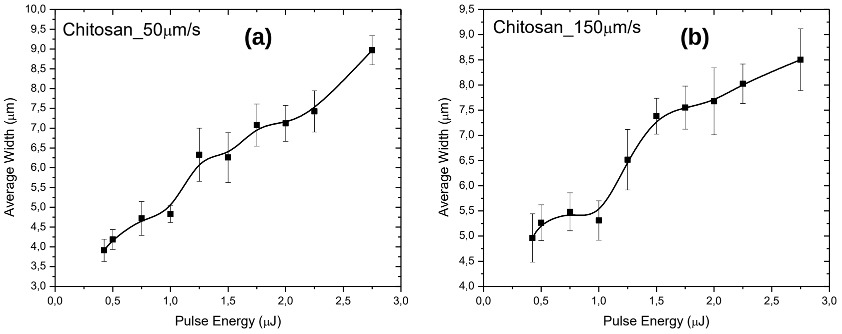

Source: Author.

For 150 μm/s (Graph 17 (b)) shows a slow increase in the average width – at low energies between 0.425 μJ to 1 μJ. However, from 1.25μJ to the last value, there is a significant growth in the width of the lines. From the Graph 17, it is clear that the lines, although machined in different translation speeds, did not show any significant change in the values of the average width.

Considering the average widths *versus* the translation speed, as represented above, when the energy per pulse of 0.425 μJ remained constant, at the high speeds, the width of the lines was still increasing considerably, which was not expected. On the other hand, for much higher energy of 2.75 μJ, also constant, the machined lines presented an expected behavior in which it suffers a decrease for higher speeds. To remember so, at high speeds, the laser beam interacts for a shorter period in which it should cause less modification for the same amount of energy.

Graph 18 - Average width for Chitosan at constant energies in relation to the speed

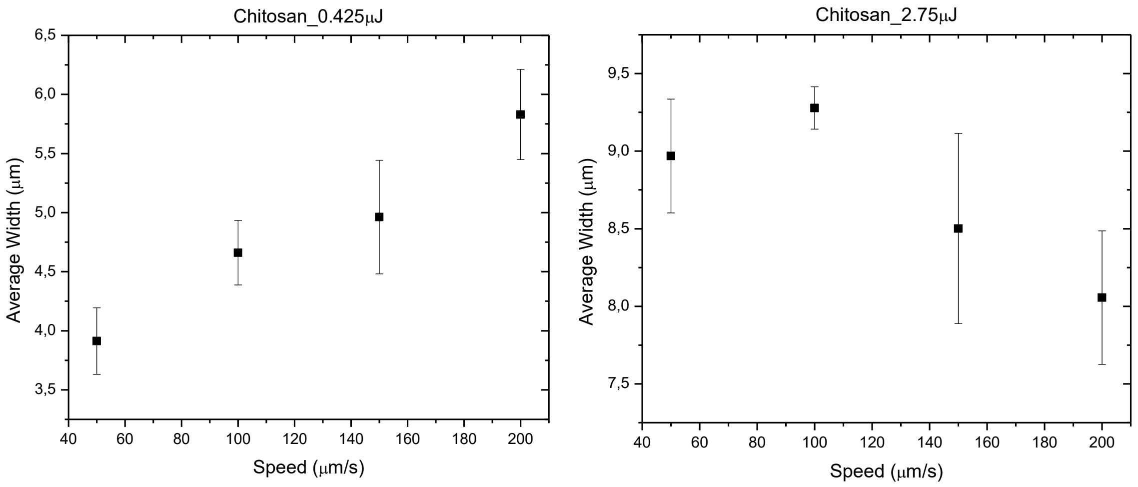

Source: Author.

Overall, micromachining for gold and chitosan showed itself very helpful to calibrate the optical setup to obtain more steady lines and, consequently, better results. One enhanced feature for the next section is that before ablating the material, it is interesting if the optical system can cause just structural changes on the surface. In this case, there are no black lines as those in chitosan pictures.

Thus, ending this section, I shall point out that, for initial results, that Chitosan and Gold films offered a great chance to map some mistakes and dismisses along with the optical setup. These graphs provided evidence about which points should care about the issues of the system. Then, we could put efforts in the right place and improve specific features, which, in turn, led to the good results presented in this work.